The third Sandia fracture challenge: predictions of ductile fracture in additively manufactured metal

As Published: https://doi.org/10.1007/s10704-019-00361-1

Publisher: Springer Netherlands

Persistent URL: https://hdl.handle.net/1721.1/131747

Version: Author's final manuscript: final author's manuscript post peer review, without publisher's formatting or copy editing

The third Sandia fracture challenge: predictions of ductile fracture in additively manufactured metal

Cite this article as: Sharlotte L. B. Kramer, Brad L. Boyce, Amanda Jones, Ahmed Mostafa, Babak Ravaji, Thomas Tancogne-Dejean, Christian C. Roth, Maysam Gorji Bandpay, Keunhwan Pack, John T. Foster, Masoud Behzadinasab, James C. Sobotka, John M. McFarland, Jeremy Stein, Ashley D. Spear, Pania Newell, Michael W. Czabaj, Bruce Williams, Hari Simha, Mark Gesing, Lindsay N. Gilkey, Christopher A. Jones, Remi Dingreville, Scott E. Sanborn, John L. Bignell, Albert Cerrone, Vincent Keim, Aida Nonn, Steven Cooreman, Philippe Thibaux, Nicoli Ames, Devin O'Connor, Matthew Parno, Brett Davis, Joseph Tucker, Baptiste Coudrillier, Kyle N. Karlson, Jakob T. Ostien, James W. Foulk III, Christopher I. Hammetter, Spencer Grange, John M. Emery, Judith A. Brown, Joseph E. Bishop, Kyle L. Johnson, Kurtis R. Ford, Steffen Brinckmann, Michael K. Neilsen, Jacek Jackiewicz, K. Ravi-Chandar, Thomas Ivanoff and Bradley C. Salzbrenner, The third Sandia fracture challenge: predictions of ductile fracture in additively manufactured metal, International Journal of Fracture https://doi.org/10.1007/s10704-019-00361-1

The third Sandia Fracture Challenge: predictions of ductile fracture in additively manufactured metal

Author List

Sharlotte L.B. Kramer, Sandia National Laboratories, slkrame@sandia.gov

Brad L. Boyce, Sandia National Laboratories, blboyce@sandia.gov

Amanda Jones, Sandia National Laboratories, ajones1@sandia.gov

Ahmed Mostafa, University of Texas at San Antonio, jenan.055@gmail.com

Babak Ravaji, University of Texas at San Antonio, ravaji@gmail.com

Thomas Tancogne-Dejean, Massachusetts Institute of Technology, tancogne@mit.edu

Christian C. Roth, ETH Zürich, ccroth@ethz.ch

Maysam Gorji Bandpay, Massachusetts Institute of Technology, gorji@mit.edu

Keunhwan Pack, Massachusetts Institute of Technology, kpack@mit.edu

John T. Foster, University of Texas at Austin, john.foster@utexas.edu

Masoud Behzadinasab, University of Texas at Austin, behzadi@utexas.edu

James C. Sobotka, Southwest Research Institute, james.sobotka@swri.org

John M. McFarland, Southwest Research Institute, john.mcfarland@swri.org

Jeremy Stein, Southwest Research Institute, jeremy.stein@swri.org

Ashley D. Spear, University of Utah, ashley.spear@utah.edu

Pania Newell, University of Utah, Pania.Newell@utah.edu

Michael W. Czabaj, University of Utah, m.czabaj@utah.edu

Bruce Williams, CanmetMATERIALS Natural Resources Canada, bruce.williams@canada.ca

Hari Simha, University of Guelph, csimha@uoguelph.ca

Mark Gesing, CanmetMATERIALS Natural Resources Canada, mark.gesing@canada.ca

Lindsay N. Gilkey, Sandia National Laboratories, lngilke@sandia.gov

Christopher A. Jones, Sandia National Laboratories, jonesca@ksu.edu

Remi Dingreville, Sandia National Laboratories, rdingre@sandia.gov

Scott E. Sanborn, Sandia National Laboratories, sesanbo@sandia.gov

John L. Bignell, Sandia National Laboratories, jbignel@sandia.gov

Albert Cerrone, GE Global Research Center, arc247@cornell.edu

Vincent Keim, Ostbayerische Technische Hochschule (OTH), Resensburg, vincent1.keim@oth-regensburg.de

Aida Nonn, Ostbayerische Technische Hochschule (OTH), Resensburg, aida.nonn@oth-regensburg.de

Steven Cooreman, OnderzoeksCentrum voor de Aanwending van Staal (OCAS), steven.cooreman@ocas.be
Philippe Thibaux, OnderzoeksCentrum voor de Aanwending van Staal (OCAS), philippe.thibaux@ocas.be
Nicoli Ames, Exponent, names@exponent.com
Devin O'Connor, Cold Regions Research and Engineering Laboratory, devin.t.oconnor@gmail.com
Matthew Parno, Cold Regions Research and Engineering Laboratory, parnomd@gmail.com
Brett Davis, Exponent, bdavis@exponent.com
Joseph Tucker, Exponent, jtucker@exponent.com
Baptiste Coudrillier, Exponent, bcoudrillier@exponent.com
Kyle N. Karlson, Sandia National Laboratories, knkarls@sandia.gov
Jakob T. Ostien, Sandia National Laboratories jtostie@sandia.gov
James W. Foulk III, Sandia National Laboratories, jwfoulk@sandia.gov
Christopher I. Hammetter, Sandia National Laboratories, cihamme@sandia.gov
Spencer Grange, Sandia National Laboratories, sgrange@sandia.gov
John M. Emery, Sandia National Laboratories, jmemery@sandia.gov
Judith A. Brown, Sandia National Laboratories, judbrow@sandia.gov
Joseph E. Bishop, Sandia National Laboratories, jebisho@sandia.gov
Kyle L. Johnson, Sandia National Laboratories, kyljohn@sandia.gov
Kurtis R. Ford, Sandia National Laboratories, krford@sandia.gov
Steffen Brinckmann, Max-Planck Institute, brinckmann@mpie.de
Michael K. Neilsen, Sandia National Laboratories, mkneils@sandia.gov
Jacek Jackiewicz, Kazimierz Wielki University Jacek.Jackiewicz@ukw.edu.pl
K. Ravi-Chandar, University of Texas at Austin, ravi@utexas.edu
Thomas Ivanoff, Sandia National Laboratories, tivanoff@sandia.gov
Bradley C. Salzbrenner, Sandia National Laboratories, bsalzbr@sandia.gov

Abstract

The Sandia Fracture Challenges provide the mechanics community a forum for assessing its ability to predict ductile fracture through a blind, round-robin format where mechanicians are challenged to predict the deformation and failure of an arbitrary geometry given experimental calibration data. The Third Challenge, issued in 2017, required participants to predict fracture in an additively manufactured 316L stainless steel tensile-bar configuration containing through holes and internal cavities that could not have been conventionally machined. The volunteer participants were provided extensive materials data, from tensile tests of specimens printed on the same build tray to electron backscatter diffraction maps of the microstructure and micro-computed tomography scans of the Challenge geometry. The teams were asked to predict a number of quantities of interest in the response, including predictions of variability in the resulting fracture response, as the basis for assessment of the predictive capabilities of the modeling and simulation strategies. This paper describes the Third Challenge, compares the experimental results to the predictions, and identifies successes and gaps in capabilities in both the experimental procedures and the computational analyses to inform future investigations.

Keywords: Fracture, Rupture, Tearing, Deformation, Plasticity, Metal, Alloy, Additive Manufacturing, Simulation, Prediction, Modeling

1 Introduction

Over the past several years, there has been a proliferation of interest, investments, and research in metal additive manufacturing (AM) technologies. While metal “3D printers” were initially developed more than two decades ago (Frazier 2014), the recent renaissance can be attributed to a number of converging factors, primarily: a) expiration of initial patents (e.g. (Deckard, et. al. 1992, Hull 1986, Meiners et. al. 1998)); b) national and international efforts, such as the America Makes program (Frazier 2014), which spawned from the US Advanced Manufacture Initiative (Hemphill 2014); c) emerging success stories from early adopters, such as the GE LEAP fuel nozzle (Foust et. al. 2012, Herderick 2017); and d) a maturing and expanding base of commercially available metal printers. AM offers many advantages over conventional manufacturing. Components, including tooling fixtures, prototypes, and production units, can be rapidly manufactured in an agile workflow. In addition, the AM process can accelerate the transition from concept through design to fabrication. Moreover, the AM process can produce complex geometric shapes that are difficult and expensive to produce by traditional manufacturing routes. This geometric flexibility is amenable to topology optimization algorithms that maximize part performance for a given set of boundary conditions (Zegard and Paulino 2016, Brackett et. al. 2011). By enabling topology optimization, the design sequence itself transitions from intuition-based object-oriented design and manual iteration to requirements-based design with automated *in silico* iteration (Kharmanda et. al. 2004). The entire concept-to-production workflow can now be performed in a more seamless computational framework (Jared et. al. 2017). Finally, the parts can be individually tailored for custom-fit applications with little or no extra manufacturing cost (Huang et. al. 2013). Despite these advantages, adoption of AM for structural applications faces potential challenges in certification for use (Seifi et. al. 2016).

The qualification of AM parts can benefit substantially from simulation-based strategies that minimize dependence on experimental testing, which is typically slow and costly compared to the agile, flexible nature of AM. Moreover, destructive testing of a subpopulation of components or test specimens relies on the assumption that the tested specimens/parts are representative of the fielded components. However, in the AM process, the microstructure, defects, and performance can vary locally throughout the 3D part volume due to inhomogeneous thermal history. Therefore, it is necessary to assess the capability of simulation strategies for effective evaluation of AM performance. Structural reliability considerations can span the gamut from elastic performance to fatigue lifetime estimation to ductile rupture. In all cases, the effects of microstructural features (e.g. porosity, crystallographic texture) can be introduced through simulation to increase fidelity. Yet it is unclear if such additional fine-scale analysis is necessary to achieve adequate predictions. In the case of fatigue-crack initiation and growth, there have been several developments in computational approaches to account for microstructural-scale heterogeneities (e.g. McDowell and Dunne 2010). In both fatigue and monotonic loading cases, industrial practice typically employs homogenized continuum-scale simulations for reliability assessment, utilizing safety factors to mitigate the effects of microstructural variability. However, homogenized continuum solutions to ductile rupture may be insufficient in heterogeneous, defect-dominated materials produced by AM.

Ductile tearing can be difficult to predict, even in the case of conventionally manufactured wrought alloys with negligible internal defects and homogeneous, isotropic microstructure (Boyce et. al. 2014, 2016). Linear elastic fracture mechanics does not apply in cases where the plastic process zone dominates the fracture process (McClintock and Irwin 1965). Even elastoplastic fracture mechanics is challenged when the material lacks sharp cracks and undergoes gross plastic collapse rather than well-defined crack propagation (Broek 2012). These issues have been the subject of an ongoing assessment activity known as the Sandia Fracture Challenges (Boyce et. al. 2014, Boyce et. al. 2016). These Sandia Fracture Challenges have illustrated several deficiencies and lack of consistency in solving engineering problems associated with ductile rupture. Aside from comparing different mechanistic models for damage progression, the Challenges have shown the difficulties in calibrating material models based on limited experimental data, ascribing appropriate boundary conditions, and capturing salient physical realism such as anisotropic plasticity or heat generation by plastic work. The current study sets out to assess if the lessons learned in the prior Challenges can be applied to components produced by AM.

The unique benefits and deficiencies of AM differentiate the present challenge from the two previous challenges, which utilized commercially available wrought alloys: 15-5PH stainless steel and Ti-6Al-4V. The ensemble of defects in the first two challenges were machined in the plate, and intrinsic material defects were ignored. In the present case, the geometry included through-thickness channels and an internal cavity that would be difficult or impossible to manufacture without AM processes. Moreover, the AM process induced variations in the dimensions of the internal (and external) features as well as spatial variations in the material properties and numerous surface defects. Finally, the AM process typically induces substantial residual stresses (Wu et. al. 2014), which was anticipated during the planning stages to influence fracture predictions.

There are numerous processes for manufacturing metal structures using AM, including laser powder bed fusion (LPBF) (King et.al. 2015), electron beam melting (EBM) (Murr et. al. 2012), and Laser Metal Deposition (LMD), also known as Laser Engineered Net Shaping (LENS) (Hofmeister and Griffith 2001). The focus of the current study is on metal manufactured by the LPBF process, a process that parallels Selective Laser Sintering (SLS) (Agarwala et. al. 1995), Selective Laser Melting (SLM) (Bremen et. al. 2012) or Direct Metal Laser Sintering (DMLS) (Khaing et. al. 2001), along with proprietary names like Direct Metal Printing or LaserCUSING® (Bechmann 2014). The LPBF process is distinguished by using a packed layer of metal powder that is fused by local laser heating. The part is built up one layer at a time by alternating between packing a layer of fresh powder and selectively fusing the powder with the laser. While the process cannot be applied to any arbitrary alloy powder with success, several alloys can be manufactured by this method including both austenitic and precipitation hardened stainless steels, Ni-based superalloys, Ti-6Al-4V, and lightweight Al-Si-Mg. The type of microstructure and defect content produced depends in part on the specific conditions of the LPBF process coupled to the type and quality of the powder feedstock (Gong et. al. 2014, Rafi et. al. 2013, Gu et. al. 2012, Beese and Carroll 2016). In general, common defects include contaminants/impurities (Bhavar et. al. 2014), gas porosity (Sun et. al. 2016), lack of fusion porosity (Tang et. al. 2017), and partially melted and sintered particles (Gong et. al. 2014). The grain morphologies, crystallographic texture, and residual stress profile can vary as a function of the local cooling rate and multi-pass thermal history as well as any post-process thermal treatments (Rafi et. al. 2013). Finally, the surfaces of LPBF parts exhibit a roughness induced by partially melted particles and solid particles trapped at the molten interface (Matthews et. al. 2016). The local microstructure and defects are heterogeneous due to subtle fluctuations in processing conditions and powder state, resulting in stochastic mechanical performance distributions that lack the consistency of comparable wrought alloys (Salzbrenner et. al. 2017). These process-dependent considerations set the backdrop for estimating the reliability of AM components in ductile rupture scenarios.

The current study, known as the Third Sandia Fracture Challenge, or SFC3, exploits the complexity of AM materials to assess the potential capabilities and deficiencies of various computational mechanics approaches. The Challenges all benefit from evaluating *blind* predictions that are performed in isolation without any knowledge of the experimental outcome or other teams' predictions, providing a realism that parallels actual engineering scenarios. To ensure unfamiliarity, each challenge employs a novel geometry that is designed with sufficient complexity to prevent back-of-the-envelope solutions. The challenge relies on volunteer participants to faithfully attempt to solve the posed problem and make quantitative predictions regarding the failure process. SFC3 emphasizes the importance of predicting not just average behavior but estimating the range of performance associated with intrinsic material variability and extrinsic factors like dimensional variations. As part of the challenge, traditional far-field measures are employed to compare and assess computational approaches. In addition, SFC3 goes beyond the prior challenges by investigating local measures of deformation. Specifically, local surface strains measured by digital image correlation (DIC) (Chu et. al. 1985) are used as a metric for evaluating the accuracy of various modeling approaches. These local measures can provide additional insight into the role of mesoscale heterogeneities (e.g. defects, residual stress), sources of model-experiment discrepancy, and delineation among different computational methodologies at a finer length scale than can be obtained by only macroscopic observables.

The Sandia Fracture Challenges rely on predictions from volunteer experts in the field of computational mechanics to assess the state-of-the-art and compare modeling approaches. All teams who participated in the SFC3 were free to choose whatever method they felt would achieve the requested predictions. In total, 21 teams from 14 institutions provided blind predictions of the current challenge problem. The teams represented a cross-section of government labs, industry, and academic institutions from Europe and North America. Notably, Sandia National Laboratories provided four separate predictions from independent teams who used different approaches and did not share information. Also, for the first time, a team of three professors at the University of Utah, led by Dr. Ashley Spear, used the Challenge in a classroom setting to compare various approaches. Their contribution resulted in seven separate team predictions using three intentionally disparate modeling approaches. However, their predictions are not considered to be entirely independent as there was some information sharing across teams.

Finally, it is important to note that the Challenges are unlike systematic or parametric studies that vary one or more elements of the prediction stream to study its effects on the result. Because each team can make many unique decisions in their approach, discrepancies can be seen in choices made along the entire prediction stream including the plasticity model, fracture criteria, damage evolution approach, model calibration methodology, uncertainty methods, the numerical implementation strategy, and computational tools. Assessments of efficacy are made, and where possible, the sources of discrepancy between experiment and model are traced to their origins.

The remainder of the manuscript is delineated into six additional sections and three appendices. Section 2 describes the Challenge as it was conveyed to the participants. Section 3 describes the experiments used for both the calibration data and the challenge experiments. Section 4 provides a brief synopsis of the various modeling methods that were employed by each team. Section 5 compares the blind predictions to experimental outcomes for a number of different macroscopic and mesoscale quantities of interest. Section 6 provides a discussion of the assessment of the effective and ineffective methods, highlighting common gaps and opportunities for future development. Section 7 provides a summary of the findings and main conclusions. The Appendices provide additional details on experimental results, modeling methods, and team-by-team assessments.

2 The Challenge

The challenge specimen for the SFC3 was designed to meet several objectives. First and foremost, the challenge geometry was developed to introduce sufficient complexity and distinction from standard geometries such that no obvious closed-form solution exists for the prediction of failure. Simultaneously, the challenge geometry was designed to contain features that could not be fabricated by conventional subtractive processes. Another design objective, as with previous challenges, was that the numerical predictions had to be readily confirmed through experiments. In fact, SFC3 was issued after experiments had already been conducted on the challenge specimens, but prior to reduction of that experimental data. Details regarding the challenge specimens, as well as the calibration specimens that were tested to provide data, are provided in the following subsections. The data is available through the Materials Data Facility (Blaiszik, et. al. 2016) via http://dx.doi.org/10.18126/M26D20 (Kramer et. al. 2018).

Teams had the option to submit 80th percentile, nominal, and 20th percentile global and local predictions to enable comparison among the population of all experimental observations. In addition, teams were required to report local strain information on the surface of the challenge geometry. The push to account for variability and honor global and local measurements is requisite to compare, contrast, and validate computational approaches to predict failure.

2.1 Overview of Material and Build Geometries

All specimens fabricated for the SFC3 were additively manufactured by a commercial vendor using LPBF with 316L stainless steel powder and a nominal layer spacing of 20 µm. The specimens included the challenge-geometry specimens, which were used for the blind predictions, and two different types of calibration specimens that were used to provide data for model definition. For the latter, un-notched and notched tensile specimens were built and tested to provide data for material-model and fracture/damage-model calibration, respectively. All of the specimens for the SFC3, including the challenge-geometry and calibration specimens, were fabricated in a single build, as shown in Figure 1. The un-notched tensile specimens were fabricated in both the build (longitudinal) and transverse directions. The notched and challenge-geometry specimens were built in the longitudinal direction only. The nominal material properties reported by the commercial vendor are listed in Table 1, and these properties were provided to all participants. Note that the un-notched tensile tests performed for the SFC3 resulted in slightly different material properties than those reported by the vendor (see Section 2.2).

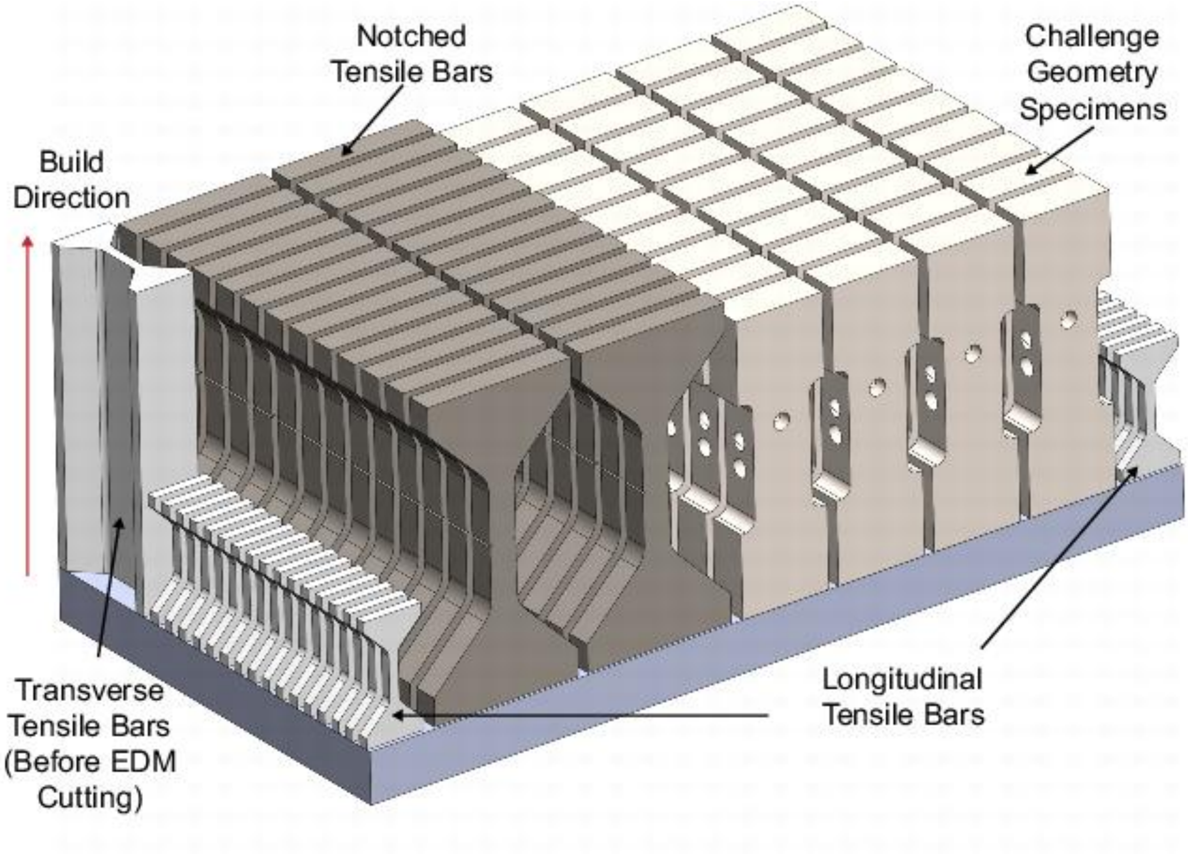

Figure 1: Layout of challenge specimens as well as tensile coupons and notched tensile bars

Table 1: AM 316L material properties as reported by the commercial vendor.

Standard	Ultimate Tensile Strength (MPa)	0.2% Offset Yield (MPa)	Elongation (%)	Hardness
AMS5653H	483	172	30	76.5 HRB to 25.5 HRC

2.2 Tensile Calibration Tests

Tensile specimens were fabricated and mechanically tested to provide the participants with data to facilitate calibration of their material models. Figure 2 shows the technical drawing of the nominal geometry of the tensile specimens, which was provided to the participants. The tensile specimens were fabricated in two different orientations, such that the loading axis was either in the build plane (transverse) or aligned with the build direction (longitudinal), see Figure 1. For identification purposes, the longitudinal and transverse tensile samples were given the pre-fix designation “LTA” and “TTA”, respectively. The transverse tensile samples were machined after

AM by electrical discharge machining (EDM). All transverse tensile samples (17 in total) were mechanically loaded to failure at a rate of 0.05 mm/s. A total of 39 longitudinal tensile specimens were tested, of which, 19 had an EDM surface finish post-build, while the remaining 20 specimens retained the native surface from the AM process. The longitudinal tensile specimens were tested to failure at a rate of 0.05 mm/s, with the exception of four EDM-surface finished specimens, which were tested at a rate of 0.0005 mm/s. A fully automated testing setup described by Salzbrenner et. al. (2017) was used to streamline the tensile testing and reduce uncertainty caused by the experimental setup. Digital Image Correlation (DIC) data were collected and analyzed using a Correlated Solutions system (VicGauge) to measure the gauge displacement of the tensile specimens. Figure 3 shows the resulting engineering stress-strain curves obtained from the tests for all tensile specimens.

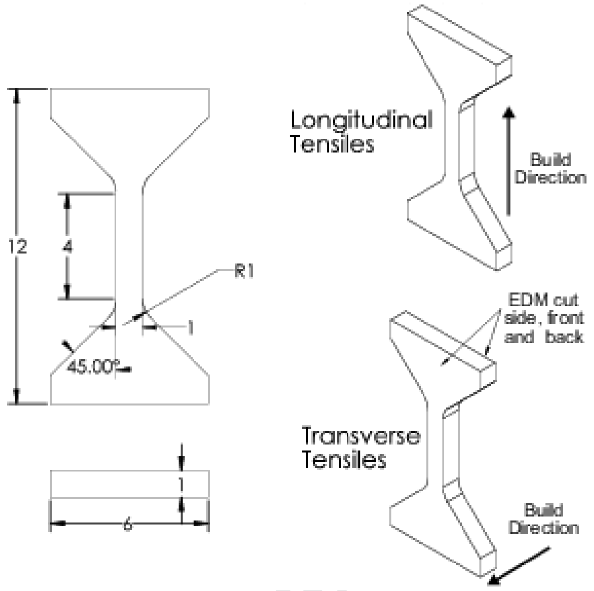

Figure 2: Tensile specimen geometry used to provide load-displacement data for model calibration. Dimensions are in millimeters.

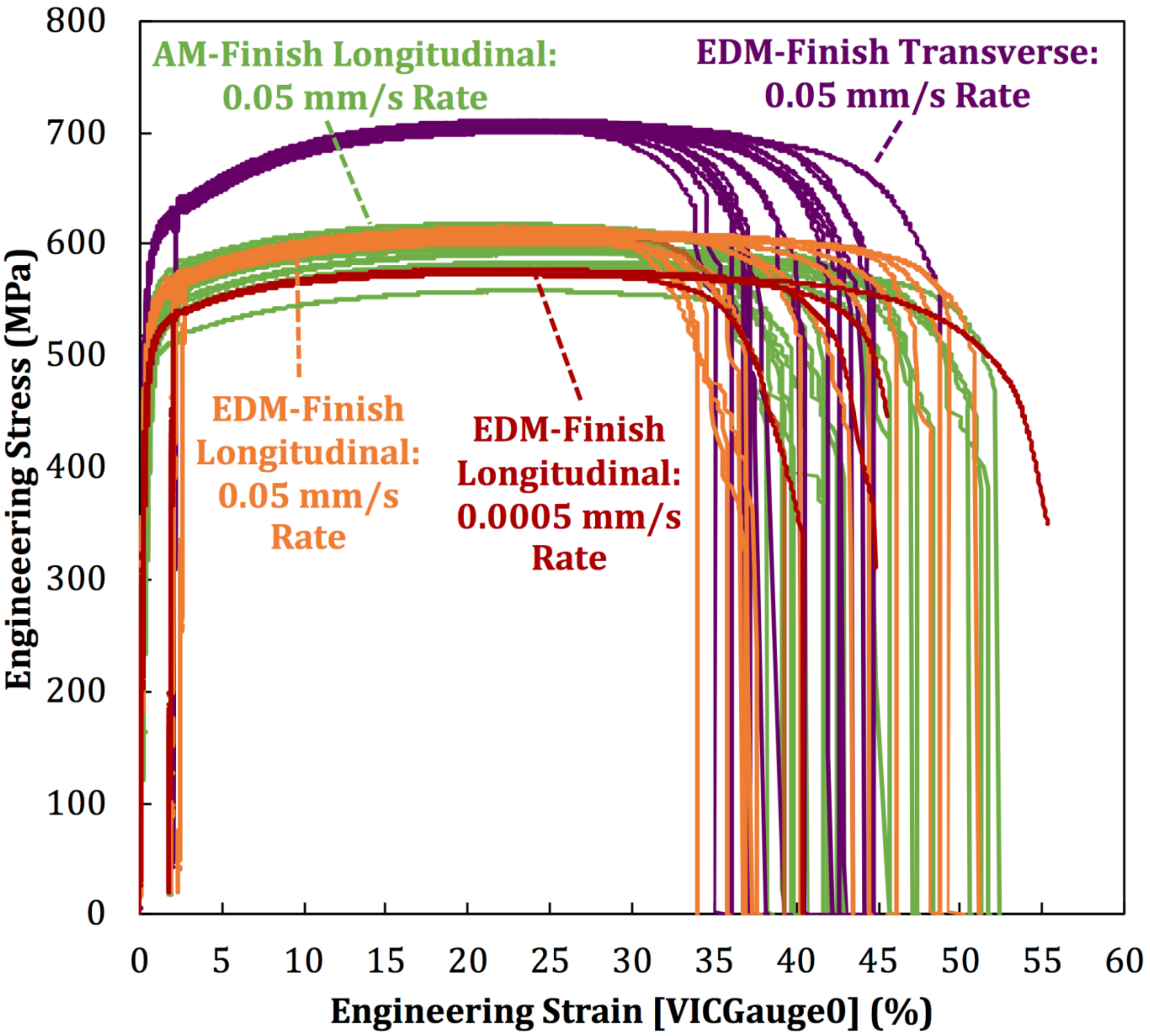

Figure 3: Summary of 4 different sets of tension calibration data: (1) AM-finish longitudinal specimens pulled in tension at a rate of 0.05 mm/s (n=20; green lines); (2) EDM-finish longitudinal specimens pulled in tension at a rate of 0.05 mm/s (n=15; orange); (3) EDM-finish longitudinal specimens pulled in tension at a rate of 0.0005 mm/s (n=4; red lines); and (4) EDM-finish transverse specimens pulled in tension at a rate of 0.05 mm/s (n=17; magenta). Note: the unloading near the initial slope was intentional in order to measure the unloading elastic modulus.

In addition to the mechanical-test data, participants were provided with data or figures from specimens characterized prior to and post failure. Specifically, the width and thickness of the gauge sections (which were measured using either a digital micrometer or optical microscope) were provided for all tensile specimens. The initial void distribution was characterized for one representative sample by cross-sectioning the sample along its length to mid-thickness and using image analysis of the sample mid-thickness plane (see Figure 4). The information from the image analysis was provided to the participants. The relative porosity in the cross section of the gauge section was reported to be 0.11%. Images of the fracture surfaces were also collected postmortem for a sample subset (see Figure 5). These images were made available to the participants at the outset of the challenge.

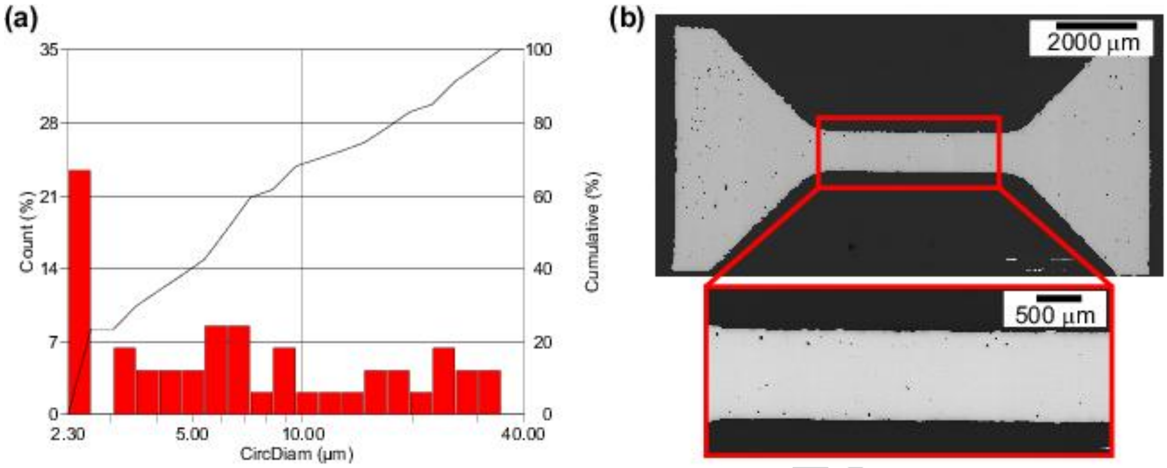

Figure 4: Void characterization of a mid-plane thickness slice of longitudinal tensile specimen LTA21. (a) Characterization of voids by size in the gauge section and (b) optical microscope image of full specimen mid-plane slice with a zoomed in image of the gauge section.

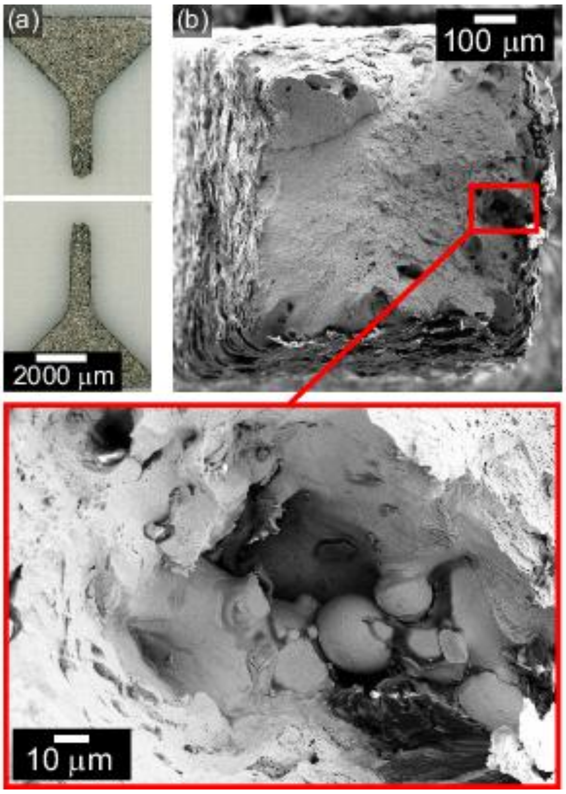

Figure 5: Representative post-test tensile specimen fracture shape and fracture surface characterization. (a) Image of the fracture shape of tensile specimen LTA04 and (b) corresponding SEM micrograph of fracture surface with call-out showing a close-up image of the fracture surface morphology. Poorly sintered areas are visible in this region.

2.3 Notched Tensile Tests

Notched tensile tests were conducted on 23 specimens to provide the participants with data for damage- or fracture-model calibration. For identification purposes, the notched tensile samples were given the pre-fix designation “NA”. The nominal geometry of the notched specimens is shown in the technical drawing of Figure 6. The notched tensile specimens were manufactured such that the loading axis would be aligned with the build direction, similar to the challenge specimens. The specimen notches were designed to have ratios of notch length to the specimen width, *a/W*, of 0.129. The actual notches were produced via the AM process. Consequently, the as-built notches did not conform precisely to this specification. Participants were provided with images of the actual as-built notches for reference, as illustrated in the example shown in Figure 7.

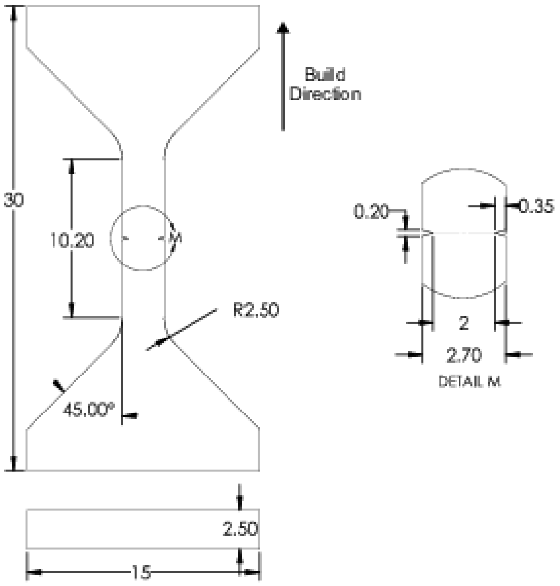

Figure 6: Notched tensile specimen geometry used to provide load-displacement data for fracture or damage model calibration. Dimensions are in millimeters.

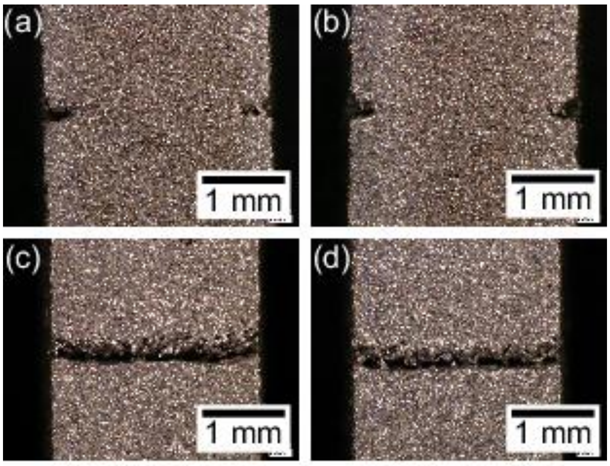

Figure 7: Pre-test images of the (a) front, (b) back, (c) left and (d) right sides of a notched tension specimen NA05 showing the variability in the cross-section and notch size.

The notched specimens were pulled in tension at 0.015 mm/sec using a uniaxial MTS load frame with custom wedge grips. Correlated Solutions VicGauge extensometer measurements were made on the front surface of the specimen, and the corresponding images were provided to the participants. The custom wedge grips were designed to properly constrain each specimen by allowing displacement only in the loading direction. Figure 8 shows a summary of the load-versus-extensometer-displacement data provided to participants.

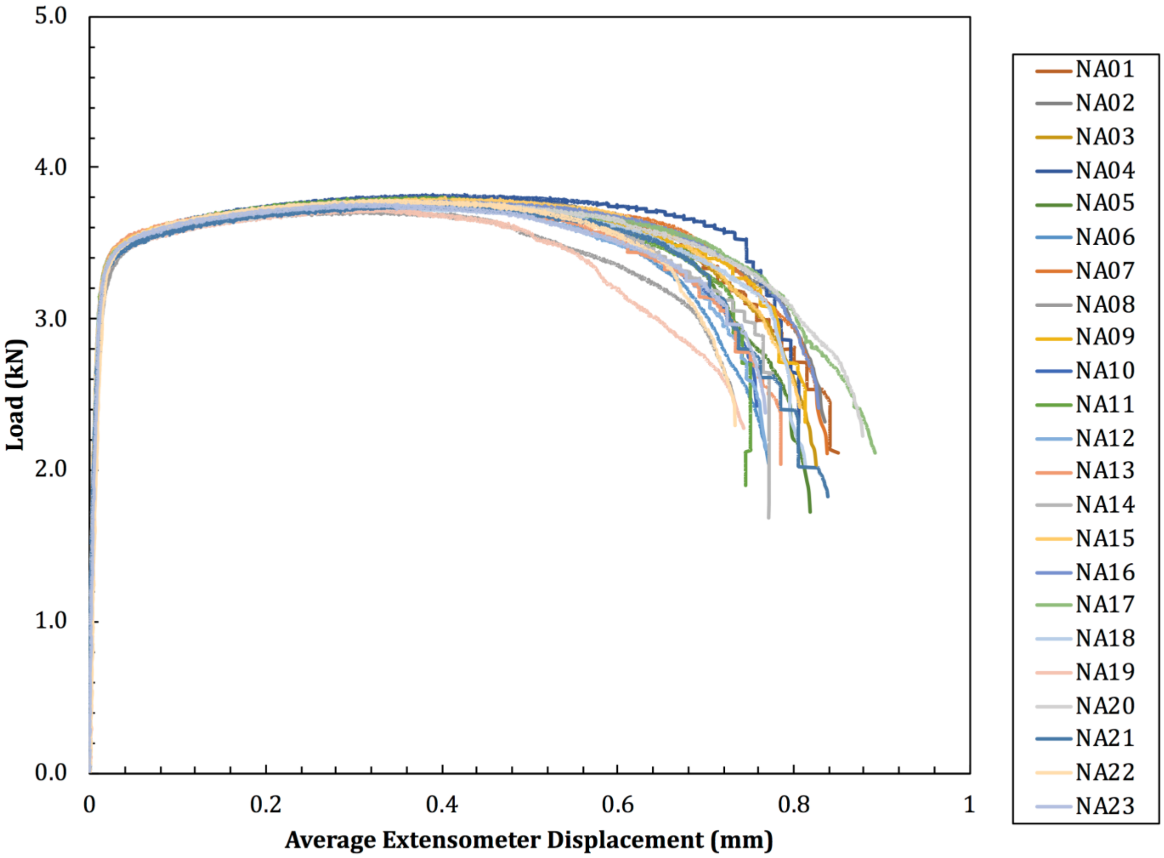

Figure 8: Notched tension test results provided to all participants.

In addition to mechanical-test data, information pertaining to void distribution was provided for an undeformed, representative notched sample by cross-sectioning the sample along its length to mid-thickness and using image analysis of the sample mid-thickness plane (see Figure 9). The relative porosity in the cross section of the gauge section was reported to be 0.09%.

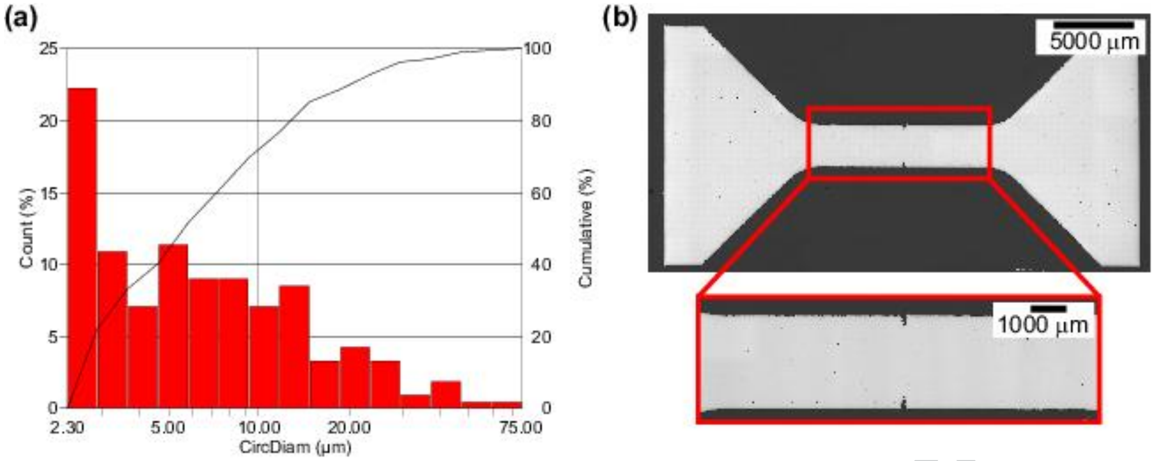

Figure 9: Void characterization of a mid-plane thickness slice of a notched tensile specimen NA24. (a) Characterization of voids by size in the gauge section and (b) optical microscope image of full specimen mid-plane slice with a zoomed in image of the gauge section.

After notched tensile testing, a subset of specimens was selected to investigate the approximate failure location in the gauge region as well as the fracture-surface morphology. An example of one of the notched specimens after testing is shown in Figure 10. The images were intended to provide teams with information to support calibration and/or validation of the simulation results.

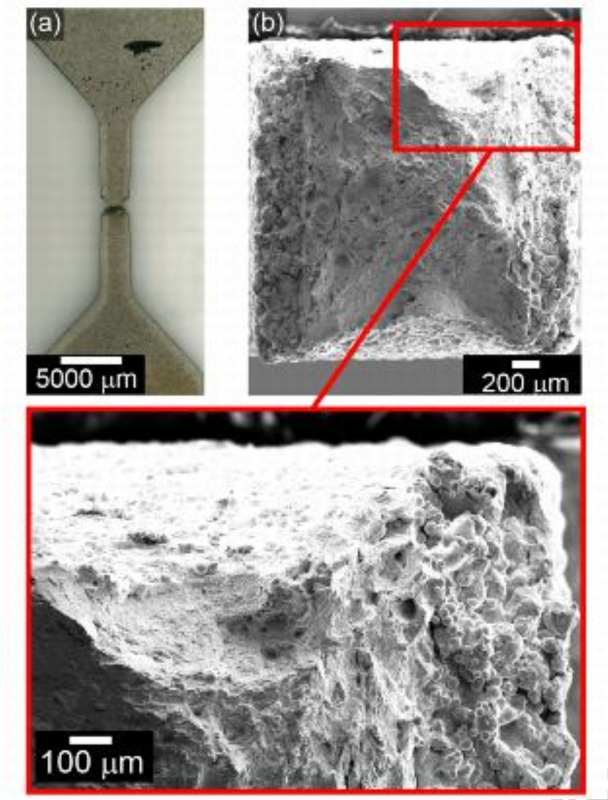

Figure 10: Post-test notch tensile specimen fracture shape and fracture surface characterization. (a) Fracture shape of specimen NA05 and (b) fracture surface morphology with zoom in on the notch region.

2.4 Challenge Specimens: Geometry and Characterization

The challenge geometry was a modified dog-bone sample with nominal gauge dimensions of 10 mm (length), 6 mm (width), and 4 mm (thickness). The geometry included several holes and cavities, including a through-thickness hole intersecting two angled channels as well as two elliptically revolved channels intersecting a spherical cavity. The nominal dimensions are shown in Figure 11. As for a representative tensile and notched tensile specimen, one undeformed challenge-geometry specimen, A06, was cross-sectioned along its length to its mid-thickness, and then this mid-thickness plane was imaged and analyzed for the void distribution (). The relative porosity in the cross section of the gauge section was reported to be 0.15%.

In total, 36 challenge specimens were manufactured and characterized. For identification purposes, the challenge specimens were given the pre-fix designation “A”. All 36 specimens were scanned using an X-Ray Worx 225kV Tubehead with a Varian Cesium Iodide 2520DX detector. The X-ray computed tomography data were acquired with North Star Imaging software and reconstructed with Volume Graphics 2.2 Max software, adopting an effective voxel size of 16.08 micron (an example of the micro-CT image is shown in Figure 13). These data were then used to determine the position and dimensions of the holes and cavities and to derive information on the statistical distribution of the porosity. For one of the specimens, EBSD (electron backscatter diffraction) measurements were performed at mid-thickness to characterize the grain structure and crystallographic texture, which is shown in Figure 14.

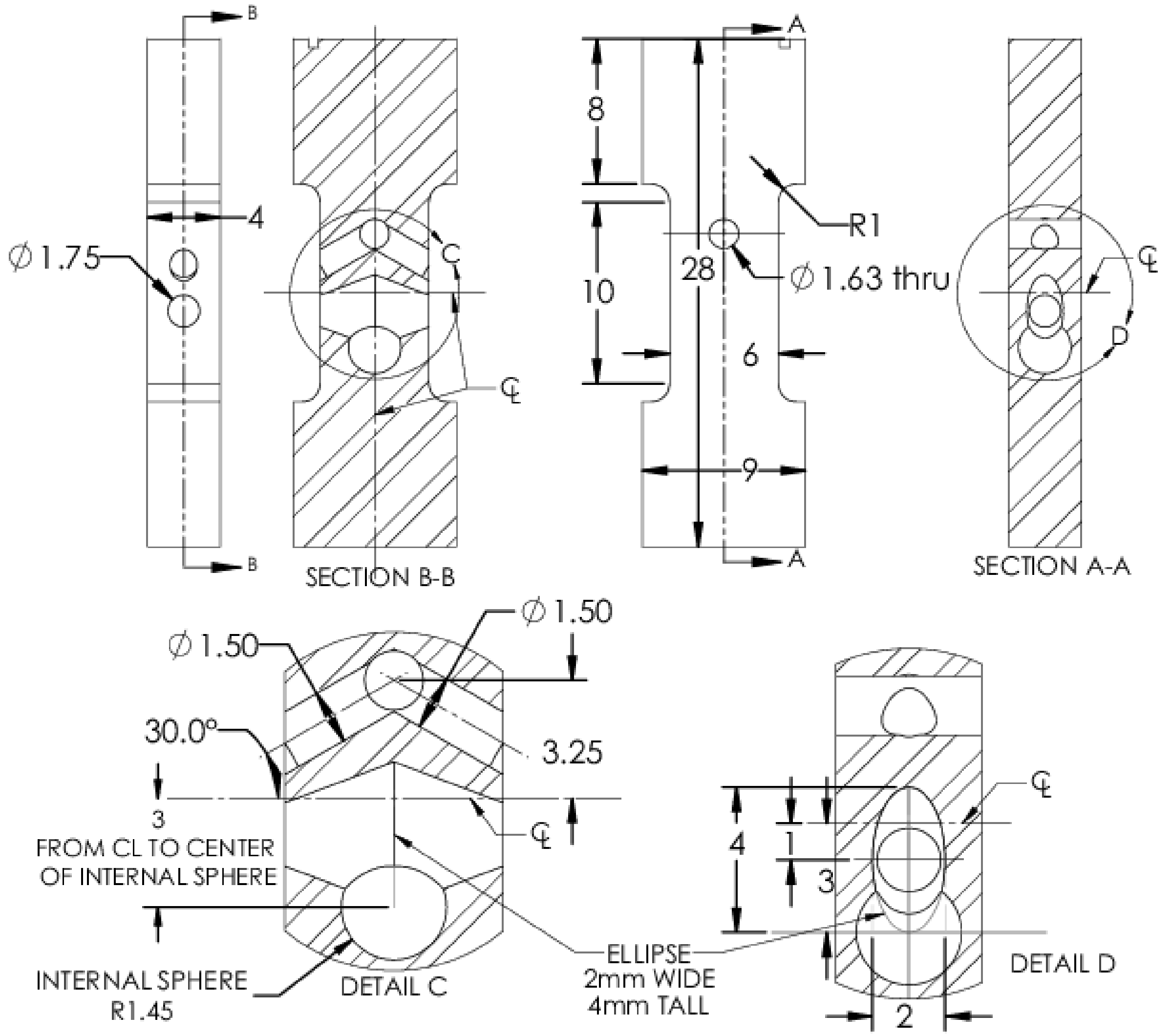

Figure 11: Dimensions of the third Sandia Fracture Challenge additively manufactured specimen geometry in millimeters.

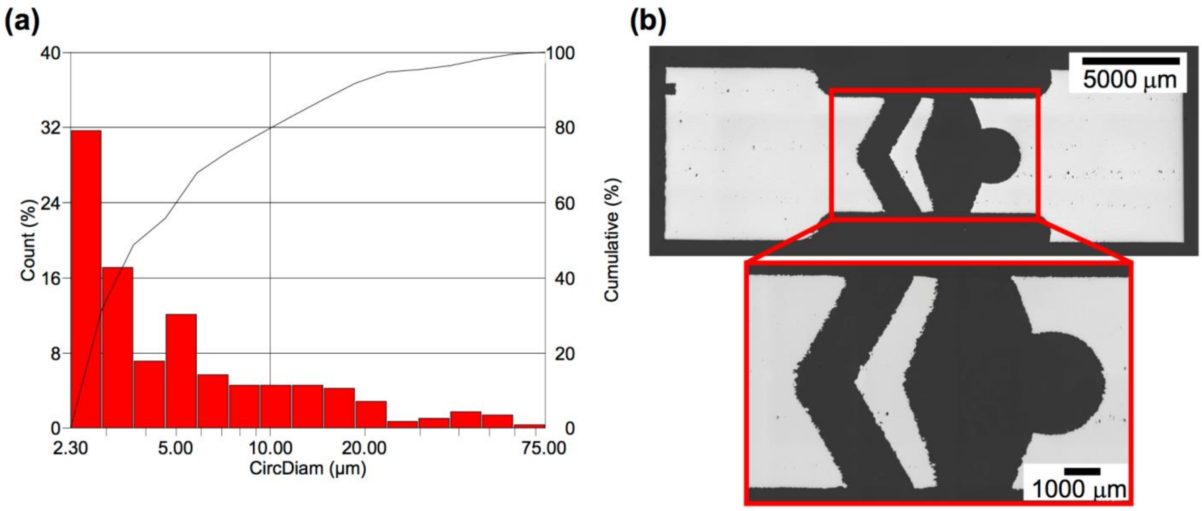

Figure 12: Void characterization of a mid-plane thickness slice of a challenge-geometry specimen A06. (a) Characterization of voids by size in the gauge section and (b) optical microscope image of full specimen mid-plane slice with a zoomed in image of the gauge section.

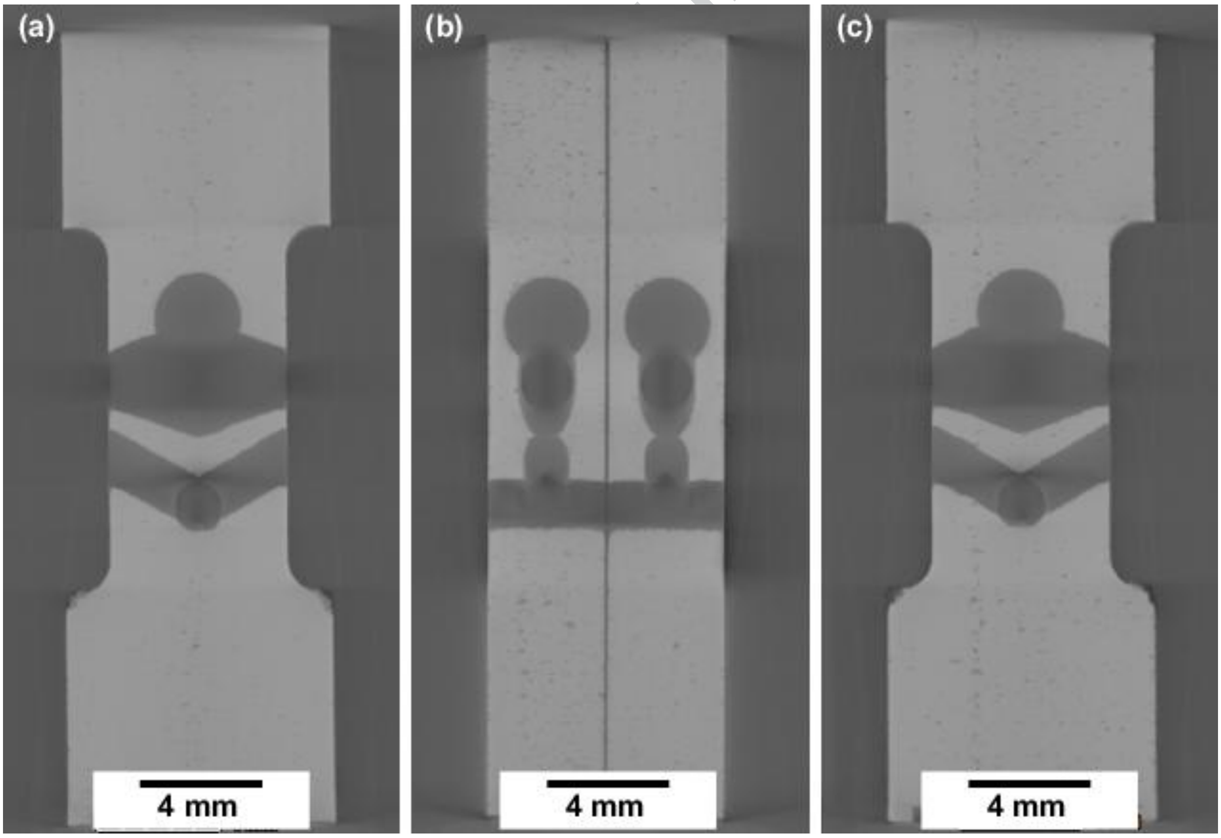

Figure 13: Example of micro-CT data of two challenge geometry specimens, A32 (left) and A15 (right). (a) A32 front view “thick slab” image, which sums the data to show all the void and internal feature content (high contrast)

through the central section of the specimens, (b) side view “thick slab” image of A32 (left) and A15 (Right), and (c) A15 front view “thick slab” image. (Note: The specimens were scanned with the build direction down.)

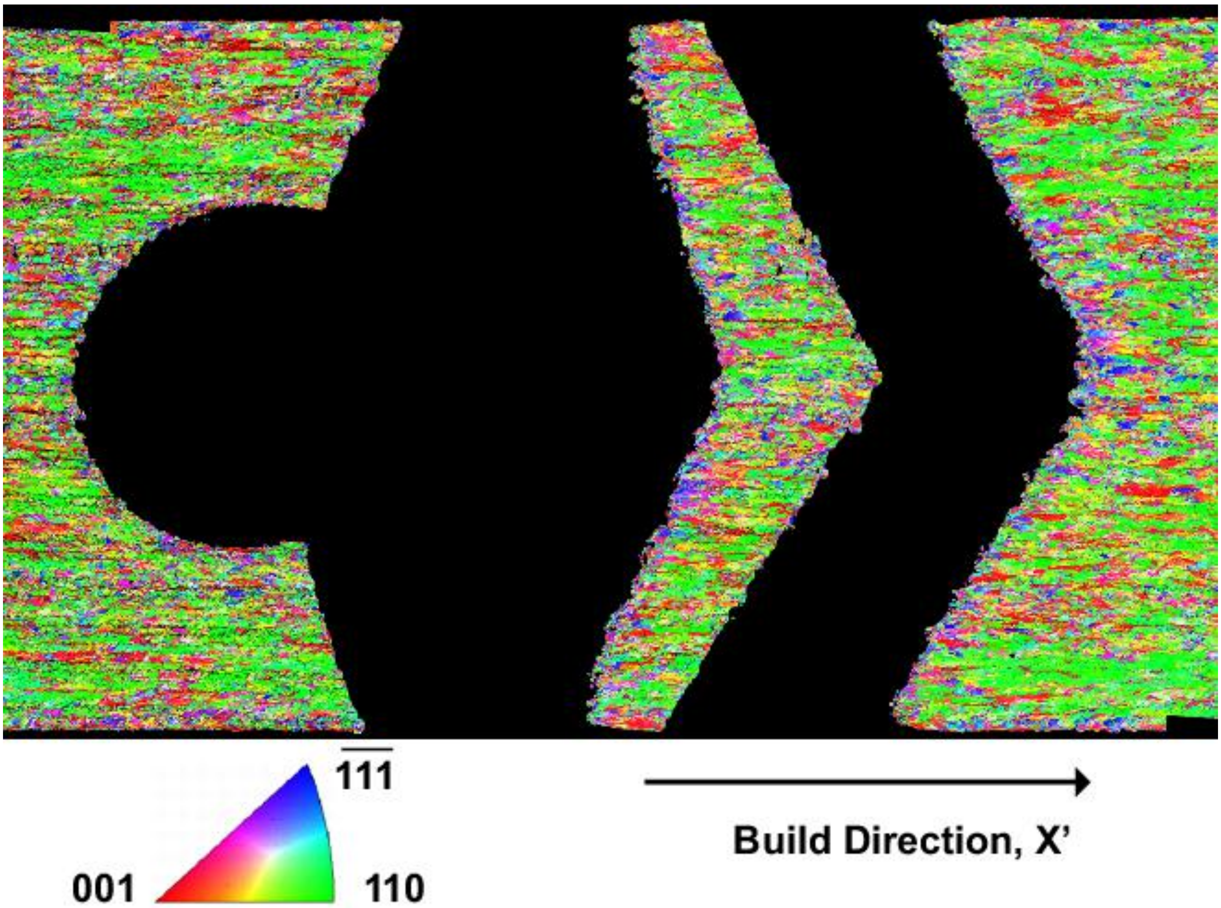

Figure 14: Inverse pole figure map from EBSD measurements on challenge geometry: large area mapping of mid-plane of challenge geometry specimen A06 along build direction (here denoted X’, equivalent to the geometry Y direction).

Void distributions in seven challenge samples were studied using three-dimensional (3D) characterizations. These 3D characterizations were digitally reconstructed from a series of two-dimensional (2D) planar projections acquired via X-ray computed tomography. Image processing was performed on each 2D projection in preparation for 3D reconstruction. Projections were first converted to 8-bit grayscale TIF (tagged image file format) images and squared within the image frame, as needed, using a bilinear rotation algorithm. Then pixel values in each image were stretched to utilize the full 8-bit pixel intensity range (0 to 255), which improves image contrast. This was accomplished by saturating the top and bottom 1% of pixel values in each image to 255 and 0, respectively. Segmentation was then used to separate material from non-material, i.e. voids. A single threshold value was manually chosen for each image stack to process material into white (pixel value of 255) and voids into black (pixel value of 0). Image artifacts produced during image processing were manually corrected.

Voids were identified by locating continuous regions of non-material surrounded by material. A minimum volume of 8 voxels, 3.3×10^{-5} mm^3 using an effective voxel size of 16.08 µm, was stipulated for void identification. Surface roughness was not characterized. The centroid location, volume, and shape of each void was determined from the 3D reconstructions. Statistical descriptions of these voids and their correlation to mechanical performance are presented in Section 6.4. Figure 15 presents two 3D reconstructions of the gauge region of a representative challenge sample. The solid structure is shown in Figure 15(a), and the voids located within this sample are shown in Figure 15(b). Standard orthographic projections of the void locations are shown in Figure 16; voids are denoted as circles that are colored to represent their volume per the scale shown. A diagonal-hash pattern with a spacing of approximately 1 mm is evident in the xy-projection. This pattern is most likely a result of the AM-build process. No patterns are evident in the remaining two projections. Participants in SFC3 did not receive the 3D void characterizations prior to submitting their predictions.

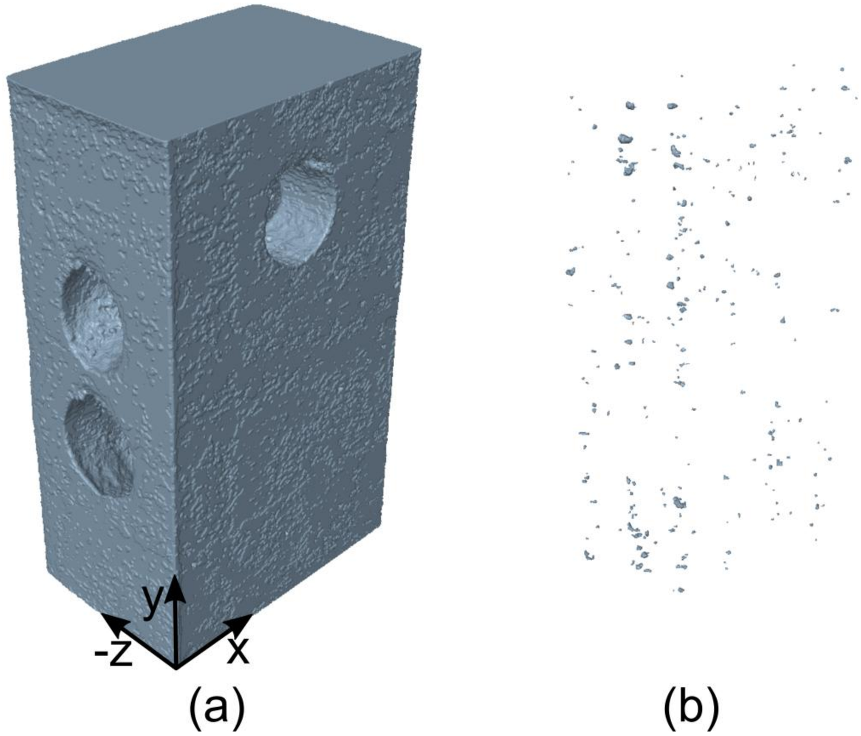

Figure 15: Three-dimensional reconstructions of (a) the solid material and (b) the voids within the gauge region of a representative challenge specimen. Explicit void information was not provided to the participants prior to submitting

predictions. However, raw X-ray CT data, from which the void information was derived, were provided to participants.

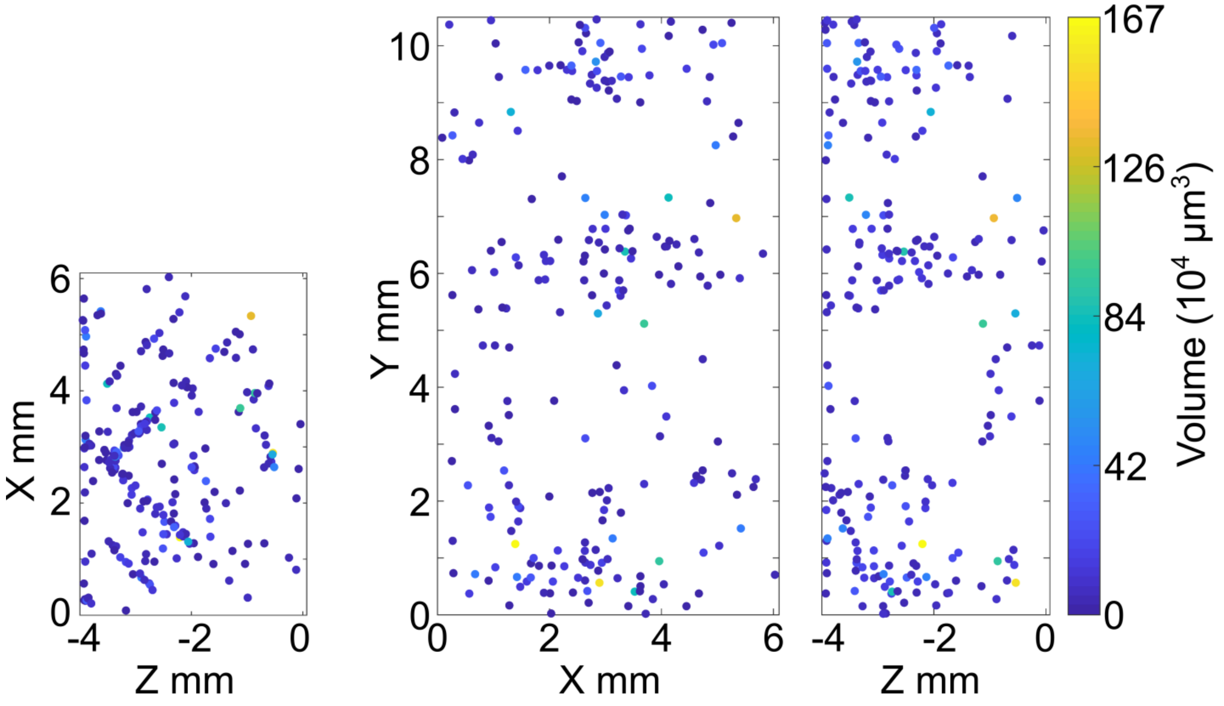

Figure 16: Standard orthographic projections of the void locations from a representative challenge sample. This void information for the challenge specimens was not provided to participants prior to submitting predictions.

2.5 Quantities of Interest

Participants were asked to report multiple quantities of interest for the challenge specimens described above. The quantities of interest included both global (*e.g.*, displacement) and local (*e.g.*, local strain) quantities. All participants were asked to report values for six questions to facilitate a quantitative comparison of the blind predictions with the experimental results. The six questions are as follows:

Question 1: Report the force at displacements (*D*) 0.25, 0.50, 0.75, and 1.0 mm.

Question 2: Report the force and Hencky (logarithmic) strain in the vertical direction (ε_{yy}) at four points, P1, P2, P3, and P4 (Figure 17), on the surface at the following forces:

- F1, 75% of peak load (before peak).
- F2, 90% of peak load (before peak).
- F3, at peak load.
- F4, 90% of peak load (after peak).

Question 3: Report the force versus gauge displacement (*D*) for the test.

Question 4: Report the force versus the Hencky (logarithmic) strain in the vertical direction (ε_{yy}) at four points, P1, P2, P3, and P4, on the surface.

Question 5: Report the force versus the Hencky (logarithmic) strain in the vertical direction (ε_{yy}) along four horizontal lines, H1, H2, H3, and H4 (Figure 17), on the surface at forces F1, F2, F3, and F4. Line scan data should be provided with a data spacing of Δx=0.030 mm.

Question 6: Provide images of the model directly viewing the front surface (same as the side for DIC) at crack initiation and at complete failure showing contours of Hencky (logarithmic) strain.

For questions 1 and 3, displacement, *D*, is defined as the vertical displacement, *v*, of six points according to the following equation:

$$D = \frac{[(v_{P8} - v_{P5}) + (v_{P9} - v_{P6}) + (v_{P10} - v_{P7})]}{3}$$

where the points P5-P10 are referenced in Figure 17.

For questions 1 through 4, participants were asked to report nominal (average) values and were optionally asked to report the 80th percentile and the 20th percentile values. Additionally, participants were asked to provide information about their modeling approach and method for determining model parameters for the blind predictions.

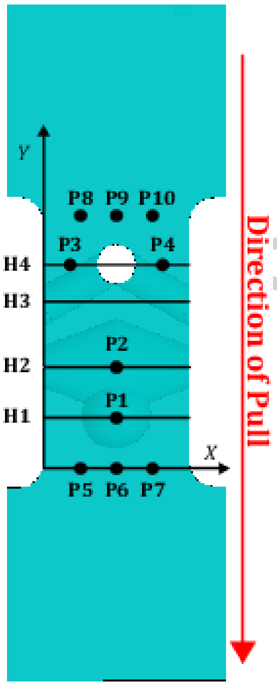

Figure 17: Annotated surface of challenge geometry to describe the points / locations of interest referenced in the challenge questions (H1-H4, P1-P4) and grip displacement measurement locations (P5- P10).

3. Experimental method and results

The mechanical behavior of the additively manufactured challenge geometry was evaluated by two different experimental teams at Sandia National Laboratories. The first set of results (12 of 19 specimens) was acquired in the Structural Mechanics Lab (SML), herein referred to as Lab 1, and supplemented by results from the Material Mechanics Lab (MML), herein referred to as Lab 2. Both teams tested specimens from the same building block by the same machine shop and used the same set of grips. DIC was conducted to capture full-field strains in both labs with independent techniques. The results from both teams were consistent with one another and no major differences were observed in failure path or crack initiation. In addition to the extensive micro-CT data and geometry measurements of internal features, pre-test caliper geometry measurements were collected for all specimens (see Appendix 2) and provided to the participants with the Challenge definition.

3.1 Observations from the Structural Mechanics Laboratory

3.1.1 Test setup and methodology

Twelve specimens were loaded in tension to failure using a 100-kN MTS load frame (Figure 18). The frame was comprised of a 150-mm MTS calibrated actuator and a 100-kN load cell, supplemented by a 22-kN auxiliary load cell. The auxiliary load cell measurements alone are reported due to the increased signal to noise ratio. A stereo-DIC setup was used to capture full-field strains and displacements throughout the test duration. The stereo-DIC system consisted of two 5 MP Point Grey Grasshopper cameras (2048 pix x 2448 pix) with Navitar 6000 zoom lenses, 0.5x Navitar lens adaptors and 1x Navitar lens tubes. The cameras/lenses were arranged at an average stereo angle of 21.25 degrees. The magnification was set to achieve an average field of view of 111.3 pix/mm. The working distance of the lens configuration was nominally 175 mm with the left camera being positioned perpendicular to the sample allowing imaging of the front face directly. The short axis of the camera (2048 pixels) was in alignment (parallel to) with the actuator motion. The exact location in space of the cameras was calibrated using a glass backlit target with 0.89-mm spacing between calibration markings, and the Vic3D 7 calibration routine developed by Correlated Solutions.

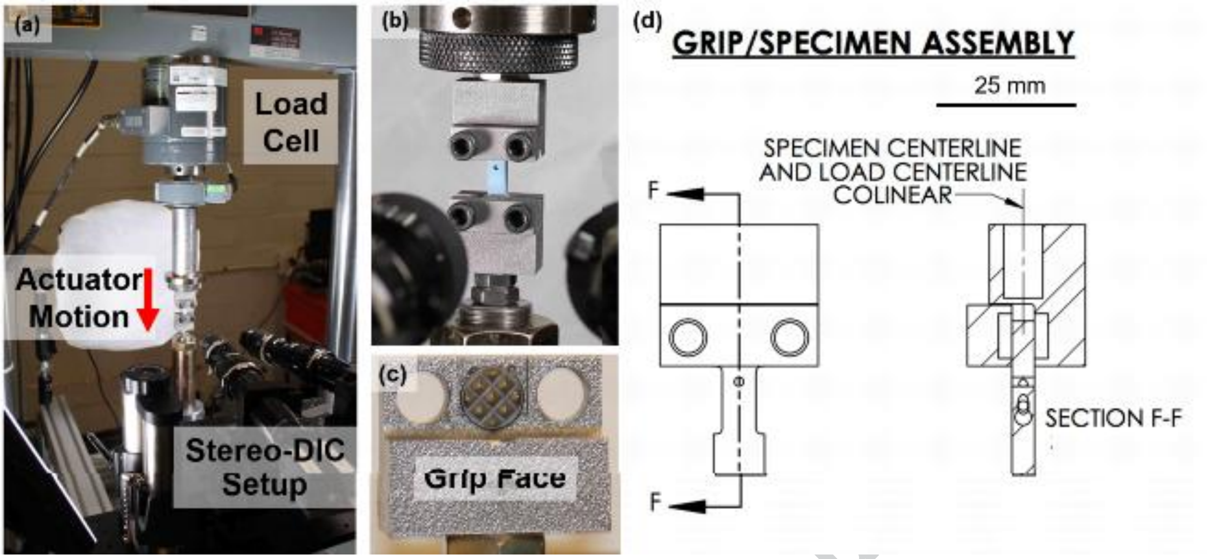

Figure 18: Experimental setup used in the Structural Mechanics Lab at Sandia National Laboratories. (a) Description of load frame and major components. (b) Close-up view of the load train with a challenge geometry specimen loaded in grips and (c) image of the grip face which was in contact with the specimen during testing and (d) engineering drawing of the gripping assembly.

Prior to testing, all specimens were painted with a white base coat of spray-paint (SEM), which was followed by application of a paint-based speckle pattern from an Infinity airbrush (Golden High Flow Acrylics, Phthalo Blue, green shade). Specimens were painted within 3 h of being tested in order to avoid paint cracking/embrittlement. The painted surface was always oriented such that the number “1” in the top grip (Figure 11) was on the “right” side in the image, consistent with the origin of the coordinate system being in the lower left corner of the specimen gauge in the image (Figure 17).

The specimens were gripped using fixed-fixed grips manufactured by a Direct Metal Laser Sintering method (DMLS) with 30-micron layers of 17-4 steel. The specimen itself was in contact with commercially available carbide pads (MSC Part #09715889) affixed to the grip body with epoxy. Specimen alignment with the load train of the load frame was guided by plastic inserts and confirmed with gauge blocks. For all specimens, the 4 bolts (two on either side of the specimen) were lightly tightened in order to engage the carbide pad teeth and then fully tightened once the load frame was in load control with set point at zero load. Once gripped, each specimen was loaded at a nominal displacement rate of 0.0126 mm/sec (displacement control), while the DIC images were acquired at 4 fps using VicSnap software and NI-DAQ synced data from an MTS FlexTest controller. This displacement rate accurately describes the rate near peak load, but due to machine compliance the loading rate was reduced (ca. 0.007 mm/sec) in the earlier portion of the load-displacement curves (<75% peak load).

For all specimens tested in the Lab 1, an identical set of post-processing parameters was used to calculate full-field strains and displacements (Table 2). All post-processing was conducted using a commercial software from Correlated Solutions, Inc. Analysis was completed using an optimized 8-tap interpolant with a zero-normalized squared difference criterion. Strains were calculated over a circular region using a centered decay filter (described in Correlated Solutions strain calculation documentation), which is based off the selection of the strain window determined during a virtual strain gauge study. Virtual strain gauge studies were conducted on several specimens to determine these optimum post-processing parameters (Reu 2012). For these parameters, we observed convergence of the strain values taken from a line scan to the left/right of the hole right before failure (highest strain gradients).

Table 2: DIC Post-processing parameters

DIC Post-Processing Parameter	Dimension	
	pixel	*mm*
Subset	41 x 41	0.368 x 0.368
Step	7	0.063
Strain Window	9 step	N/A
Virtual Strain Gauge	57	0.512

The noise floor was defined as the standard deviation of the given parameter for a set of five static images (zero displacement or strain) and average noise floor values for all specimens tested in Lab 1 are given in Table 3. These values represent the minimum resolvable strain/displacement values for this set of experiments. Strain/displacement values below these levels could be accurate but are below the threshold established by the noise floor.

Table 3: DIC Noise floor parameters

DIC Noise Floor (Lab 1)	
U (mm)	0.000177
V (mm)	0.000138
W (mm)	0.000603
ε_{xx} ($\mu\varepsilon$)	351.2
ε_{yy} ($\mu\varepsilon$)	244.8
ε_{xy} ($\mu\varepsilon$)	211.2

3.1.2 Test observations and results

Load-displacement results are compiled from both testing laboratories (Build A) in Figure 19. A discretized set of the load-displacement data (matching the values requested in the first challenge question) is given in Table 4.

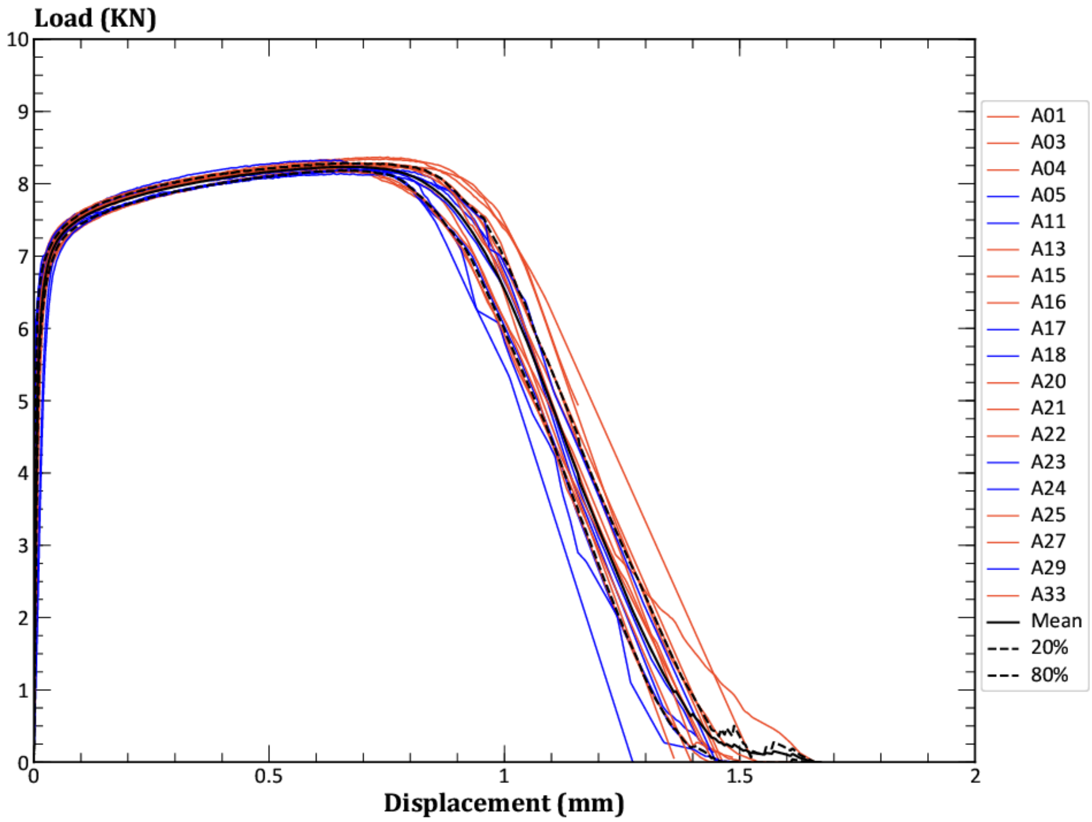

Figure 19: Load-displacement data for all challenge geometry tests from the Lab 1 (orange) and Lab 2 (blue) compiled against the experimental mean (solid black), the 80th %-tile (black, short dash) and the 20th %-tile (black, short dash) results.

Table 4: Summary of forces at prescribed displacements called out in challenge Q1.

Specimen	Testing Lab	Force (N) at D=0.25 mm	Force (N) at D=0.5 mm	Force (N) at D=0.75 mm	Force (N) at D=1.0 mm
A01	1	7936.9	8222.8	8343.0	7371.0
A03	1	7949.5	8248.2	8366.3	7411.3
A04	1	7791.0	8090.6	8233.2	7459.4
A05	2	7825.0	8096.2	8162.4	6793.3
A11	2	7887.8	8147.6	8205.9	6649.4
A13	1	7886.9	8186.3	8250.9	6896.0
A15	1	7800.3	8099.5	8029.3	5846.4
A16	1	7968.3	8222.0	8252.4	6718.9
A17	2	7926.5	8175.1	8151.3	6029.5
A18	2	7994.8	8273.0	8166.4	5469.7
A20	1	7873.9	8169.9	8276.9	7046.0
A21	1	7909.0	8187.2	8220.8	6117.0
A22	1	7806.3	8119.0	8067.6	6119.8
A23	2	7840.1	8080.5	8126.7	5813.5
A24	2	7817.3	8109.0	8169.1	6530.0
A25	1	7958.9	8209.1	8085.5	5917.3
A27	1	7898.0	8181.7	8280.0	6669.7
A29	2	7809.1	8095.4	8189.8	6883.4
A33	1	7916.0	8207.7	8274.5	6483.3
Maximum		**7994.8**	**8273.0**	**8366.3**	**7459.4**
80th %-ile		**7941.9**	**8214.3**	**8275.5**	**6956.0**
Average		**7884.0**	**8164.3**	**8202.7**	**6538.2**
20th %-ile		**7814.0**	**8098.2**	**8141.5**	**5984.6**
Minimum		**7791.0**	**8080.5**	**8029.3**	**5469.7**
Std Dev		**63.7**	**58.9**	**89.4**	**581.3**

Displacement values were obtained from DIC results as the difference between the average of 3 points at the top (P8-P10) and bottom (P5-P7) respectively (Figure 17); i.e. point measurements were taken in 1.5 mm increments at both the top and bottom yielding three measurements on each side (the three measurements were then averaged to give one value for both top and bottom). All specimens gradually increased in load, reaching a peak, which was followed by crack initiation and then failure. Statistics regarding displacements and loads at peak (D_p and F_p), crack initiation (D_c and F_c), and failure (D_f and F_c) are given in Table 5. Note that crack initiation was determined visually by examining the specimen surface. Cracks generally were observed initiating on the left or right side of the through-hole near the top of the specimen (Figure 20). All specimens failed in the same general location (left or right of the through-hole) shortly after crack initiation.

Table 5: Summary of displacements and corresponding forces for all challenge geometry specimens at crack initiation and at failure.

Specimen	Peak Displacement, D_p (mm)	Peak Force, F_p (N)	Crack Initiation Displacement, D_c (mm)	Crack Initiation Force, F_c (N)	D_c- D_p (mm)	F_c- F_p (N)	Side of Crack Initiation	Failure Displacement, D_f (mm)	Failure Force, F_f (N)	D_f- D_p (mm)	F_f-F_p (N)
A01	0.747	8344.6	0.760	8242.8	0.013	-101.8	Right	1.159	4850.4	0.411	-3494.2
A03	0.752	8370.4	0.871	8131.0	0.119	-239.4	Right	1.528	12.5	0.775	-8357.9
A04	0.784	8238.6	0.866	8089.0	0.082	-149.6	Left and Right	1.542	0.3	0.758	-8238.3
A05	0.731	8178.7	0.856	7943.0	0.124	-235.7	Right	1.447	123.1	0.715	-8055.6
A11	0.628	8233.1	0.899	7771.4	0.270	-461.7	Left	1.408	360.7	0.780	-7872.4
A13	0.700	8270.8	0.736	8245.5	0.036	-25.3	Right	1.469	-78.4	0.769	-8349.2
A15	0.647	8170.5	0.659	8069.1	0.012	-101.4	Right	1.443	4.6	0.796	-8165.9
A16	0.643	8287.3	0.743	8234.8	0.100	-52.5	Left and Right	1.456	16.1	0.813	-8271.2
A17	0.591	8226.7	0.633	8187.5	0.042	-39.2	Right	1.399	177.4	0.809	-8049.3
A18	0.639	8331.9	0.648	8308.0	0.009	-23.9	Right	1.274	-17.6	0.635	-8349.5
A20	0.669	8285.9	0.855	8098.1	0.186	-187.8	Right	1.486	65.4	0.816	-8220.5
A21	0.654	8260.1	0.663	8234.8	0.009	-25.3	Left	1.435	6.8	0.781	-8253.3
A22	0.636	8189.8	0.774	7894.7	0.138	-295.1	Right	1.659	3.2	1.023	-8186.6
A23	0.637	8151.5	0.891	7275.9	0.254	-875.6	Right	1.470	9.6	0.834	-8141.9
A24	0.672	8199.5	0.696	8179.0	0.024	-20.5	Left	1.003	6484.2	0.330	-1715.3
A25	0.531	8218.5	0.624	8194.7	0.092	-23.8	Left and Right	1.397	10.4	0.865	-8208.1
A27	0.697	8288.0	0.738	8264.1	0.041	-23.9	Right	1.503	-1.8	0.806	-8289.8
A29	0.757	8204.3	0.836	8092.7	0.079	-111.6	Left and Right	1.449	12.8	0.692	-8191.5
A33	0.657	8293.0	0.669	8190.4	0.012	-102.6	Right	1.363	0.3	0.707	-8292.7
Average	0.672	8249.6	0.759	8086.7	0.087	-163.0	N/A	1.415	633.7	0.743	-7616.0

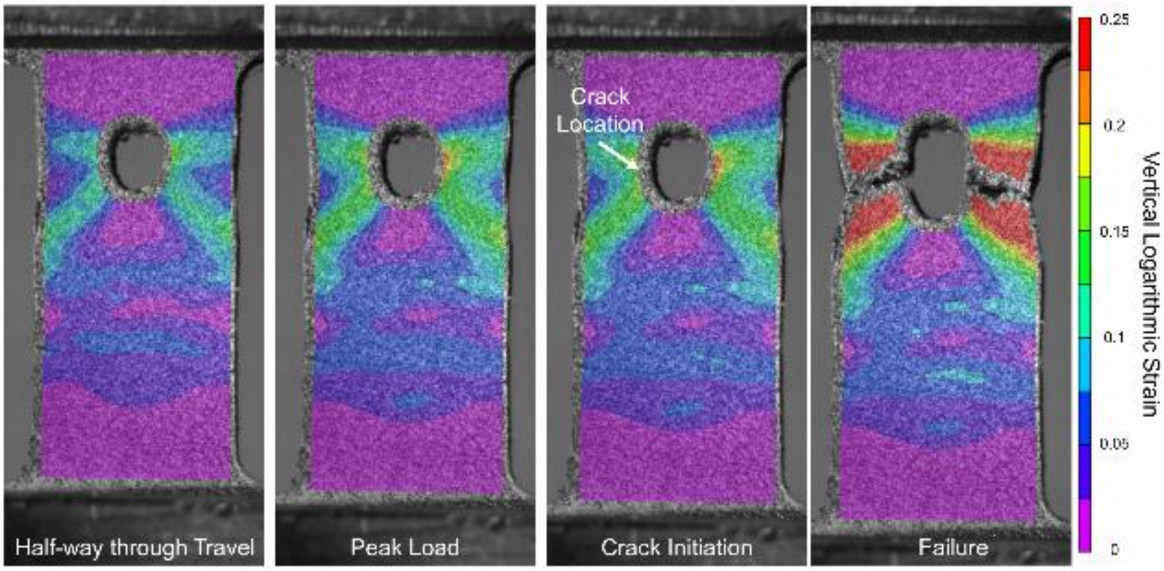

Figure 20: DIC contour strain maps for the challenge geometry specimen A21 ca. half-way through travel (D=0.5 mm, F= 8168 N), peak load (D_p= 0.654, F_p=8260 N), crack initiation (D_c=0.663 mm, F_c=8235 N) and at failure (D_f=1.435 mm, F_f= 3.2 N).

SEM images of the fracture surface are shown in Figure 21. The fracture surfaces mimic the fracture surfaces shown for the tensile and notch specimens. In all specimens, the observed voids ranged from extremely small (less than 1 micron) to quite large (100s of microns).

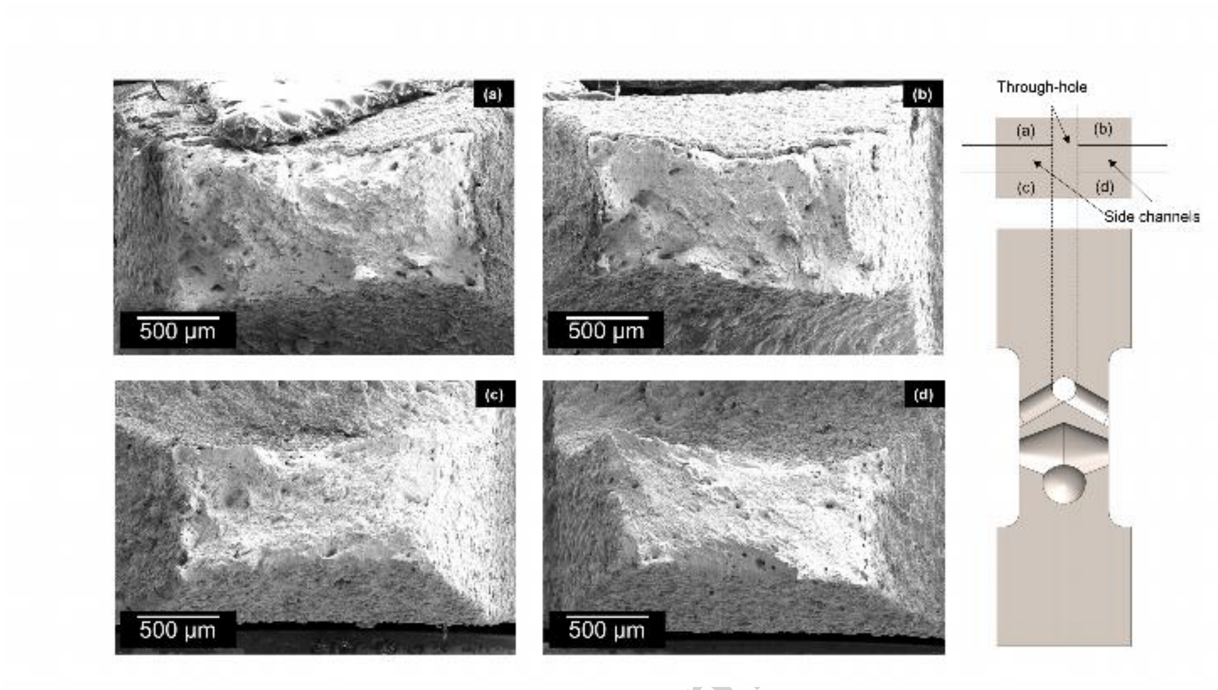

Figure 21: SEM images of the fracture surface for each of the 4 quadrants of specimen A21 after failure.

In this challenge, an emphasis was placed on exploring predictive capabilities for both global and local strain measures. Full-field displacements and strains obtained by DIC were critical towards achieving the second part of this goal. Figure 22 depicts the first example of local strain versus load measurements, while the average results are provided in Table 6. The highest strains occurred on either side of the through hole (P3/P4), which were located in the failure region. By comparison, strains on the surface near the two large internal cavities were significantly lower at failure.

The competition between the strains at each of the points of interest at four loads of interest can be seen in Table 6 and Figure 22. The differences between the strains at the four points of interest, P1-P4 were fairly small at lower forces, (e.g. F1 and F2 at 75% of peak load and 90% of peak load respectively), but as the test continued the strains near the through hole increased more rapidly. This is due to the stress concentration at the through-hole, which dominated over the weakening of the specimen from internal cavities. For all but one point, P2, the strain increased monotonically until failure. In contrast, at P2 the measured strain was slightly compressive. One possible reason for this observation is that as the sample pulled towards failure, the internal cavity caused the surface material to deform inward, resulting in negative bending strains. This hypothesis is corroborated by the measured out of plane displacements from DIC, with the caveat that these strains are very small and near (or below in some cases) the noise floor threshold. Another hypothesis is that this effect is related to residual stresses, the study of which is outside the scope of this work.

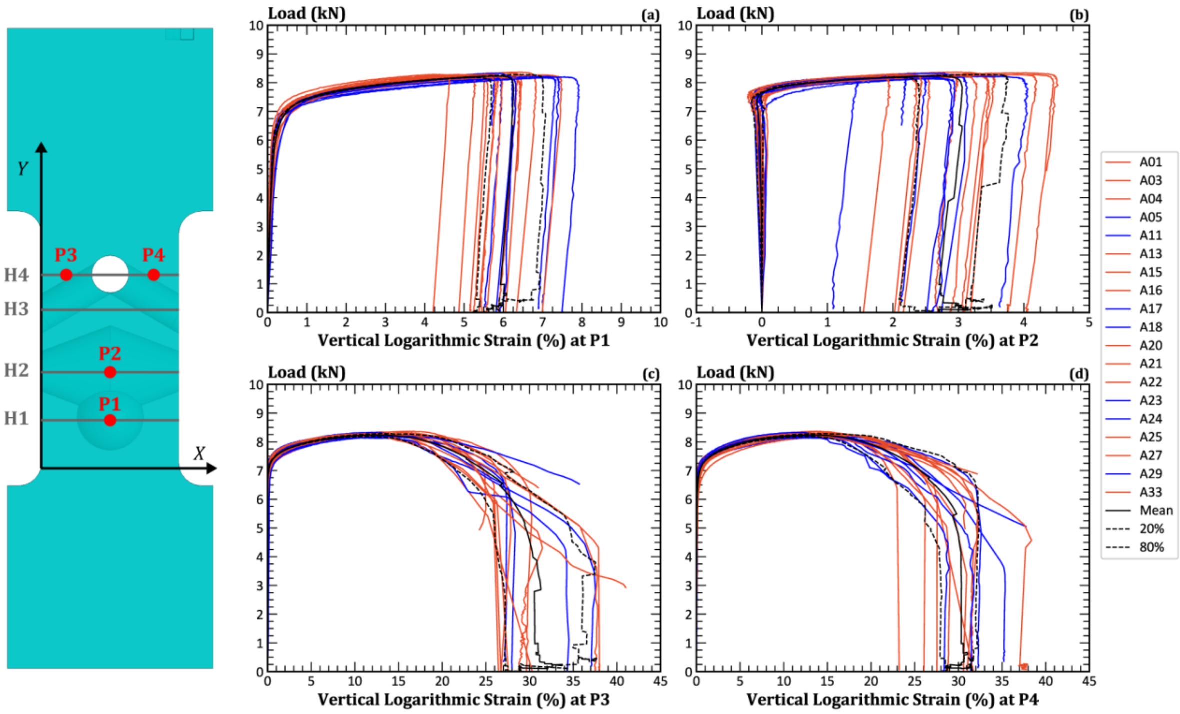

Figure 22: Load and surface strain results at points of interest P1-P4, which are shown in the schematic of internal additively manufactured features. Load vs. vertical logarithmic strain plots for both Lab 1 (orange) and Lab 2 (blue), plotted against the experimental average (solid black), 80th %-tile (black, short dash) and 20th %-tile (black, short dash) results for (a) P1, (b) P2, (c) P3, and (d) P4.

Table 6: Summary of local strains at points P1-P4 at four forces of interest: F1= 75% peak load, F2= 90% peak load, F3= peak load, F4= 90% peak load after peak.

Type	Force Level	Force (N)	Vertical Strain at P1	Vertical Strain at P2	Vertical Strain at P3	Vertical Strain at P4
80th %-ile	F1	6217.5	0.002439	0.000079[a]	0.000401[a]	0.001410
Average		6187.2	0.002020	-0.000276	-0.000348	0.000751
20th %-ile		6146.7	0.001410	-0.000739	-0.001125	-0.000042[a]
80th %-ile	F2	7461.0	0.010721	-0.000176[a]	0.010661	0.016590
Average		7424.7	0.009575	-0.000761	0.007084	0.012887
20th %-ile		7376.0	0.008382	-0.001500	0.003620	0.009688
80th %-ile	F3	8290.0	0.065802	0.032396	0.145217	0.144238
Average		8249.6	0.058266	0.026422	0.126698	0.133132
20th %-ile		8195.6	0.050696	0.020034	0.110758	0.120416
80th %-ile	F4	7461.0	0.069988	0.037234	0.246385	0.261842
Average		7424.7	0.062507	0.030498	0.230000	0.237710
20th %-ile		7376.0	0.056987	0.023896	0.205089	0.218041

[a] These values fall outside the noise floor of the DIC measurements and cannot be reported with certainty. Note: all average values are above the noise floor threshold.

In addition to point measures, line scan strain measurements were taken. Similar to the point measures, little strain accumulated near H1 or H2 (lines that include P1 and P2). One example of strain accumulation along the four lines is given in Figure 23 at the peak load (load F3). It is worth noting that there appears to be a small asymmetry/bias towards higher strains on the right side of the sample. This will be discussed briefly in Section 3.2. Finally, a compilation of the line-scan strains at four different loads (F1: 75% peak load, F2: 90% peak load, F3: peak load, and F4: 90% after peak load) is given in Appendix 2.

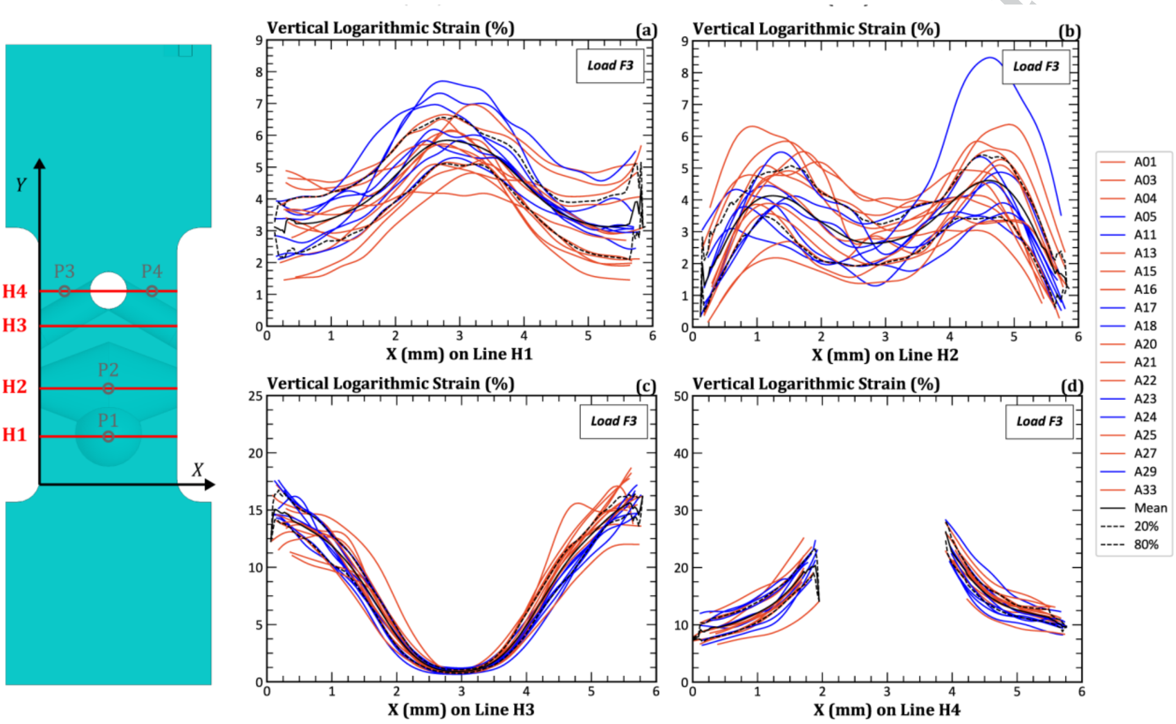

Figure 23: Line scan results along lines H1-H4, which are shown in the schematic of the location of lines H1-H4 in relationship to the internal additively manufactured features. Vertical logarithmic strain vs. horizontal (x) location plots at peak load (F3) for both Lab 1 (orange) and Lab 2 (blue), plotted against the experimental average (solid black), 80th %-tile (black, short dash) and 20th %-tile (black, short dash) results for (a) H1, (b) H2, (c) H3, and (d) H4. Note the difference in y-axis scale.

3.2 Confirmation observations from the Material Mechanics Laboratory

The test setup in Lab 2 was very similar to the setup in Lab 1, but with slightly different instrumentation (Figure 24). Tests were conducted on an MTS load frame with a 150-mm actuator and 90-kN load cell. The stereo-DIC system was comprised of two 6 MP AVT cameras with Navitar 12x zoom lenses and a stereo angle of 14.9 degrees, yielding a FOV of 143 pix/mm. The exact location in space of the cameras was measured using a commercial calibration routine, incorporated into Vic3D 7 software, developed by Correlated Solutions, and using a glass backlit target with 1.34 mm spacing between calibration markings. Specimens were speckled using a similar paint-based technique and pulled in tension at an identical rate while imaging at 4 fps.

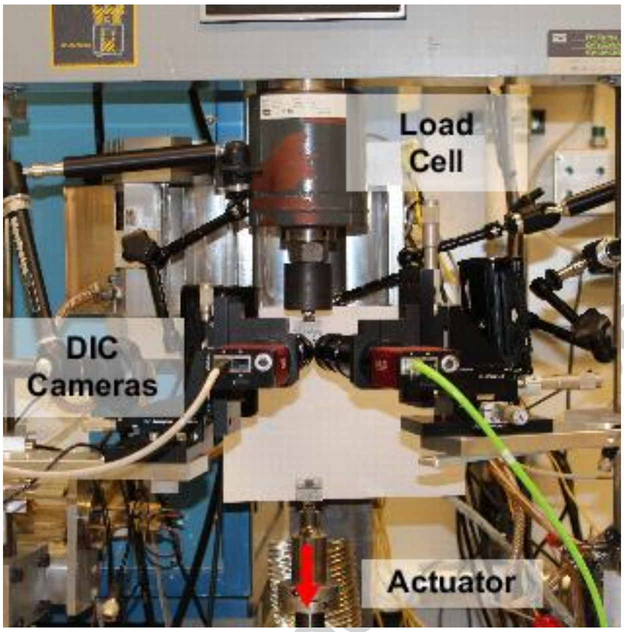

Figure 24: Lab 2 test setup, showing camera placement and load frame.

For all samples, an identical set of post-processing parameters was used, and the strain window was selected to match as closely as possible the strain window used in the Lab 1 (Table 7). The associated noise floor from these parameters (as defined above) is tabulated in Table 8.

Table 7: DIC Post processing parameters used in the Lab 2.

DIC Post-Processing Parameter	Dimension	
	pixel	*mm*
Subset	41 x 41	0.287 x 0.287
Step	7	0.049
Strain Window	11 step	N/A
Virtual Strain Gauge	71	0.50

Table 8: DIC Noise Floor associated with Lab 2 measurements.

DIC Noise Floor (MML)	
U (mm)	0.000844
V (mm)	0.001064
W (mm)	0.001440
ε_{xx} (με)	260.2
ε_{yy} (με)	202.7

ε_{xy} ($\mu\varepsilon$)	163.0

The most noteworthy difference between the two series is the addition of a swivel joint below one set of grips in Lab 2 for two specimens: A18 and A24. It was observed that the cracks initiated on the right side for 12 specimens, both sides for four specimens, but on the left side for only three specimens (Table 5). Due to the concern this could be a bias from the fixed-fixed gripping conditions, the series of data from Lab 2 also included two swivel joint tests. These tests were not conclusively different from the rest of the series and crack initiation occurred on different sides for these two tests, implying the fixed-fixed grips were not solely responsible for the majority of crack initiation occurring on the right side. One other hypothesis for the bias in failure is preferential void accumulation on one side of the specimen from the AM process. Overall, for both labs, the specimen-to-specimen variability in mechanical response was low in spite of expectations based on AM-introduced inhomogeneities.

4 Brief synopsis of modeling approaches

Each blind prediction ideally being independent, modeling choices vary. This section consists of information about the material models, the numerical methods, and uncertainty propagation approaches used by each team, including a short description comparing and contrasting the approaches. Additional details for each blind prediction can be found in Appendix 1.

4.1 Description of Methods

Table 9 presents a summary of the numerical methods employed by all the teams to solve the boundary value problem (BVP). The table categorizes methods with the following column headings: Team, Solver, Coupling, Boundary Conditions, Element Type, Discretization, Fracture Method, and Uncertainty Bounds. Details about the constitutive relations used to relate deformation to load are summarized in the following subsection, along with details of the damage or fracture formulation. The second column of Table 9 summarizes the numerical methods used in response to the fracture challenge. The finite element method (FEM) was the predominant method used to solve for the relevant field variables, and ABAQUS was the most widely used FE code. Team C employed the mesh-free, peridynamic method for the solution. Temporal discretization and/or load incrementation are necessary to solve nonlinear BVPs, and there were three choices used in response to the challenge including explicit time integration, implicit time integration, and pseudo-time integration or quasi-statics.

In previous challenges, effects of loading rate and adiabatic heating played a dominant role in the deformation processes. Consequently, fully coupled thermo-mechanical models were introduced by two teams to account for heat generation and its influence on the constitutive behavior, as shown in the third column of Table 9; all other teams neglected these effects. The specific constitutive models used to characterize the elastic-plastic deformation of the material is discussed in Section 4.2.

As with any BVP, the treatment of boundary conditions is an essential aspect of the modeling approach. The choices of boundary conditions are summarized in the fourth column in Table 9For this problem, all teams applied kinematic boundary conditions to distal node sets in some manner. The most common approach was to fix one grip end and apply displacements to the opposite grip end. Some teams applied opposing displacements, and some teams applied velocities.

Element formulation is another important decision for the numerical modeling approach (column 5 of Table 9). The majority of the teams used reduced-integration, linear hexahedron elements, presumably with hourglass control. For ease of meshing, 11 teams used tetrahedrons in modeling the challenge geometry, in part or in whole. The discretization varied widely resulting in a reported range of 33,000 up to 5,980,000 degrees of freedom, as shown in column 6 of Table 9.

Column 7 in Table 9 summarizes the fracture method employed by the different teams. By far the most common method used a local damage model, reducing element or Gauss point stiffness based on accumulated damage. The form of the damage model varied and is described in Appendix 1. Local damage can include element deletion to avoid numerical complications, and was used by most teams, but not all. The peridynamic solution approach, used by Team C, is naturally positioned to address fracture where classical damage mechanics is incorporated by irreversible damage to material point bonds. Team E used FRANC3D to adaptively remesh to accommodate an evolving crack shape, which, for elasto-plasticity, is assumed to require state variable mapping. This team employed a crack-tip displacement criterion to inform growth, and direction was chosen locally to be perpendicular to the maximum principal stress. Teams I, J, and K applied the extended finite element method, locally enriching element shape functions to allow for discontinuities in their displacement field. Their approach used either strain or stress for initiation and a displacement or energy criterion for crack advance. The direction for crack propagation was taken to be orthogonal to the maximum principal stress.

Finally, column 8 in Table 9 summarizes the approach to account for uncertainty bounds. A common approach was to calibrate the constitutive model to available data that represented mean and upper and lower bounds of performance. There were several more complex approaches. For instance, Team D employed Latin Hypercube sampling for response surface construction. Team N examined discrepancies between available damage models. Team P used Bayesian inference to identify distributions of material parameters and the forward uncertainty propagation was achieved with Markov chain Monte Carlo simulation. Team R developed a simple model for random porosity. Finally, Team S calibrated Weibull probability distributions to approximate the distribution of material parameters.

Table 9. Methods employed by teams participating in the Sandia Fracture Challenge.

Team	**Solver**	**Coupling**	**Boundary Condition**	**Element Type**	**Discretization (Element Size and Number of Degrees of Freedom)**	**Fracture Method**	**Uncertainty Bounds**
A	Explicit dynamics	No	Surface nodes, fixed and applied displacement	Tet4	*0.02 mm x 0.02 mm* *178k*	Local damage w/ element deletion	N/A
B	Explicit dynamics	No	Symmetry, fixed nodes, applied velocity	Hex8, reduced integration	*0.05mm x 0.08 mm* *460k*	Local damage w/ element deletion	Material parameters -- assumed Gaussian
C	Explicit peri-dynamics	No	Surface nodes, fixed	Mesh-free	*0.14mm x 0.14mm* *1200k*	Peridynamics with bond damage	Material parameters
D	Explicit Dynamics	No	Symmetry, fixed rotations, applied velocity	Tet10 & Hex8, reduced-integration	*0.10mm x 0.10mm* *1,150-1,180k*	Local damage w/ element deletion	Material and geometric parameters, LHS and response surface
E	Implicit	No	Surface nodes, fixed and applied displacement	Predominantly Tet10, with Hex20, quarter-point and Wedge15 along crack front	*from 0.10mm x 0.10mm to 0.3mm x 0.3mm in gauge region; 0.01 mm x 0.01 mm along crack front.* *Approx. 200k to 1,800k*	Adaptive remeshing; state mapping; CTD; maximum tangential stress	N/A
F	Explicit with mass scaling	No	Surface nodes, fixed and applied displacement	Tet10	*0.1395 mm x 0.1379mm* *1,235k*	Local damage w/ element deletion	Material parameters (hardening and damage parameters) calibrated to experimental bounds of double-notched specimens
G	Explicit with mass scaling	No	Symmetry, fixed nodes, applied displacement	Tet4	*0.186mmx0.179mm* *211k*	Local damage w/ element deletion	N/A
H	Explicit with mass scaling	No	Surface nodes, fixed and applied displacement	Tet10 explicit	*0.05mm x 0.05mm* *5,980k*	Local damage w/ element deletion	Material parameters (fracture strain) calibrated to experimental bounds of double-notched specimens
I	Implicit	No	Surface nodes, fixed and applied displacement	Hex8, reduced integration w/ XFEM enrichment; Tet4 elsewhere	*0.3mm x 0.3mm* *52k*	XFEM	N/A
J	Implicit	No	Surface nodes, fixed and applied displacement	Hex8, reduced integration w/XFEM; Tet4 elsewhere	*0.25mm x 0.29 mm* *51k*	XFEM	N/A
K	Implicit	No	Symmetry, fixed nodes, applied displacement	Hex8, reduced integration w/XFEM; Tet10 elsewhere	*0.15mm x 0.15mm* *109k*	XFEM	N/A
L	Explicit dynamics	No	stiff, displacement /velocity	Hex8	*0.1mm x 0.1mm* *555k*	Local damage w/ element Deletion	Material and geometric parameters

M	Implicit Dynamics	Fully coupled	Applied velocity at carefully selected “grip” nodesets	Hex8	0.1mm x 0.1mm	Local damage w/ element deletion	Material parameters
N	Implicit Dynamics	No	Symmetry, fixed nodes, applied displacement	Hex8, reduced integration	0.05mm x 0.05 mm	Local damage w/ element deletion	Model discrepancy for bounds
O	Implicit dynamics	No	Tied constraint, fixed and applied velocity	Hex8, reduced integration	*0.085mm x 0.085mm* *1,815k*	Local damage (no deletion)	N/A
P	Explicit dynamics	No	Surface nodes, fixed and applied velocity	Hex8, reduced integration	*0.15mm x 0.15mm*	Element deletion	Bayesian inference and adaptive Metropolis MCMC focused on material parameters
Q	Implicit quasi-statics	No	Surface nodes, fixed and applied displacement	Hex8, selective reduced integration (Q1P0)	*0.03mm x 0.053 mm*	Local damage w/ element Deletion	Material and geometric parameters; calibration to all data sets
R	Implicit quasi-statics	No	Symmetry, fixed nodes, applied displacement	Hex8, selective reduced integration (Q1P0)	*0.041mm x 0.035mm* *894k*	Local damage w/ element Deletion	Material Parameters, Overlaid Porosity Distributions, calibration to bounds
S	Implicit quasi-statics	No	Symmetry, fixed nodes, applied displacement	Tet10	*0.21mm x0.21mm* *218k*	Local damage	Material parameters -- exponential Weibull by fitting the 20,50 and 80% data
T	Explicit with mass scaling	No	Surface nodes, fixed and applied displacement	Tet4	*0.1mmx 0.1mm* *1,064k*	Local damage w/ element deletion	N/A
U	Implicit quasi-statics	No	Surface nodes, fixed and applied displacement	Hex8	33k	Local damage	Material parameters

4.2 Description of Material and Damage/Fracture Models

The description of the material models includes a description of the underlying elasto-plasticity model, the fracture/failure model, and which data were used for calibration. Table 10 includes information about the modeling choices each team made. Previous challenges emphasized the importance of selecting appropriate yield surfaces, as well as evaluating the importance of strain rate and temperature dependence. These choices are represented in the columns 2-4 of Table 10. As in previous challenges, there typically was a wide variation in the choices of fracture/failure modeling approach, ranging from strain-to-failure to micromechanically informed porosity evolution laws. These selections are displayed in columns 5 and 6. Lastly, the calibration processed is summarized by identifying which of the provided data sets were used to find model parameters (Column 7).

The different plasticity models consist of a yield surface, hardening law, and whether or not strain rate and temperature dependence were used in the challenge prediction. Amongst all the teams, only two yield surface descriptions were used, with a majority of teams selecting the isotropic von Mises, or J_2 plasticity, model. Otherwise, a few teams used a variant of the anisotropic Hill yield representation. In terms of hardening, every team selected an isotropic hardening approach, and many teams used a tabulated hardening curve available in ABAQUS. The remaining teams employed a variety of other nonlinear functions to represent hardening behavior. The vast majority of teams did not incorporate temperature dependence into their models; however, eight teams incorporated strain-rate dependence.

Many teams used a critical value of damage, or a damage-like variable, as the fracture criterion. Damage evolution models used by the teams included the Gurson-Tvergaard-Needleman (GTN) model as well as other modified GTN models. Related models of damage evolution included stress triaxiality dependence and some form of dependence on the third invariant of the deviatoric stress, J_3, whether directly, or through the Lode angle, or Lode parameter. A few teams selected a critical fracture strain, or maximum principal stress or strain, in conjunction with the XFEM capability in ABAQUS. Team O chose a damage initiation criterion based on equivalent plastic strain exceeding a threshold value, depending on triaxiality; however, once damage initiated, an energy-based criterion was applied to describe the evolution of damage.

The last column of Table 10 identifies which data sets were used for calibration. With the exception of Teams A, R, and U, every team utilized the longitudinal and notched tension data. Unsurprisingly, the teams that chose a Hill yield surface also calibrated against both the longitudinal and the transverse tension data. Calibration to the data was typically performed in an iterative process; details of the material and damage/failure model used by each team can be found in Appendix 1.

Table 10: Models employed by teams participating in the Sandia Fracture Challenge.

Team	**Plasticity**			**Fracture/failure**		**Calibration**
	Yield Function	**Hardening (isotropic)**	**Rate/Temp**	**Initiation Criteria**	**Damage Evolution**	
A	J_2	tabular	No/No	Damage	GTN failure	Transverse
B	Hill 48	Swift-Voce	Yes/No	Damage	Hosford-Coulomb	Longitudinal, transverse & notched
C	J_2	Power law	No/No	Damage	Johnson-Cook	Longitudinal & notched
D	Hill	Power law	Yes/No	Damage	Triaxiality/Lode parameter dependent	Longitudinal, transverse & notched
E	J_2	Tabular	No/No	Max. principal strain	Crack tip displacement, max tangential stress	Longitudinal & notched
F	J_2	Tabular	No/No	Critical fracture strain	Ductile damage (critical displacement)	Longitudinal & notched
G	J_2	Tabular	No/No	Critical fracture strain	Ductile damage (critical energy)	Longitudinal & notched
H	J_2	Tabular	No/No	Critical fracture strain	Ductile damage (critical energy)	Longitudinal & notched
I	J_2	Tabular	No/No	Max. principal strain	Displacement-based	Longitudinal & notched
J	J_2	Tabular	No/No	Max. principal stress	Energy-based	Longitudinal & notched
K	J_2	Tabular	No/No	Max. principal strain	Displacement-based	Longitudinal & notched
L	Hill	Power law	No/No	Damage	Triaxiality/Lode angle dependent	Longitudinal, transverse & notched

M	Hill	Power law	Yes/Yes	Damage	Triaxiality dependent	Longitudinal, transverse & notched
N	Hill	Tabular	Yes/No	Damage	GTN failure	Longitudinal, transverse & notched
O	J_2	Tabular	Yes/No	Critical strain (triaxiality dependent)	Ductile damage (critical energy)	Longitudinal & notched
P	Hill	Tabular	Yes/No	Damage	Displacement based	Longitudinal, transverse & notched
Q	Hill	Power law	Yes/No	Damage	Triaxiality/J_3 dependent	Longitudinal, transverse & notched
R	J_2	Exponential	No/No	Damage	Triaxiality/J_3 dependent	Longitudinal
S	Hill	Five parameter	No/No	Damage	Pressure dependent	Longitudinal & notched
T	J_2	Tabular	Yes/No	Damage	Wilkins et al	Longitudinal & notched
U	J_2	tabular	No/No	Damage	Modified GTN	Longitudinal

5 Comparisons

Overall, the team predictions in the third Sandia Fracture Challenge are in better agreement with the experimental record than in the earlier challenges. All teams predicted the correct fracture path, several teams predicted the correct elastic-plastic response prior to damage, and two teams predicted the entire nominal load-displacement curve within the experimental bounds. Measured DIC strains introduce a new local quantity of interest that was not investigated in the earlier challenges, and there were significant discrepancies between predicted and measured strains. In this challenge, strain fields were reported at discrete locations, along lines at various loads, and on the surface near initial damage and final failure. Twelve teams provided uncertainty bounds in addition to nominal predictions.

The remainder of this section compares team predictions with experimental measurements on a question-by-question basis as reported by the individual teams. Due to the large amount of data measured and predicted, several comparison plots have been relegated to Appendix 2, and we direct the interested reader to that section of the report.

5.1 Questions 1 and 3: Loads vs. displacements

The first and third challenge questions asked participants to report simulated loads against virtual gauge displacement for the challenge specimen. Question 1 requested these loads at discrete displacements, and question 3 requested the full load-displacement curve. Teams were encouraged to report nominal predictions and 20th/80th percentile bounds to compare against nominal and bounded measurements from the suite of replicate experiments.

Predictions for question 1 have been plotted in Figure 25 against the measured load-displacement curves. In general, predictions most closely matched experimental measurements at the lowest displacement levels (0.25 mm and 0.50 mm) where an elastic-plastic material response dominated. At 0.25 mm, nineteen teams originally predicted the nominal load within 10% of the nominal experimental value, and several teams were better than 1%. At 0.50 mm, seventeen teams predicted nominal loads within 10%, and two teams were better than 1%. (For reference, there is a 1.6% difference at 0.25 mm and a 1.4% difference at 0.50 mm between the experimental 20th/80th percentiles relative to the nominal value.) These predictions represent major improvements relative to the previous Sandia Fracture Challenge results.

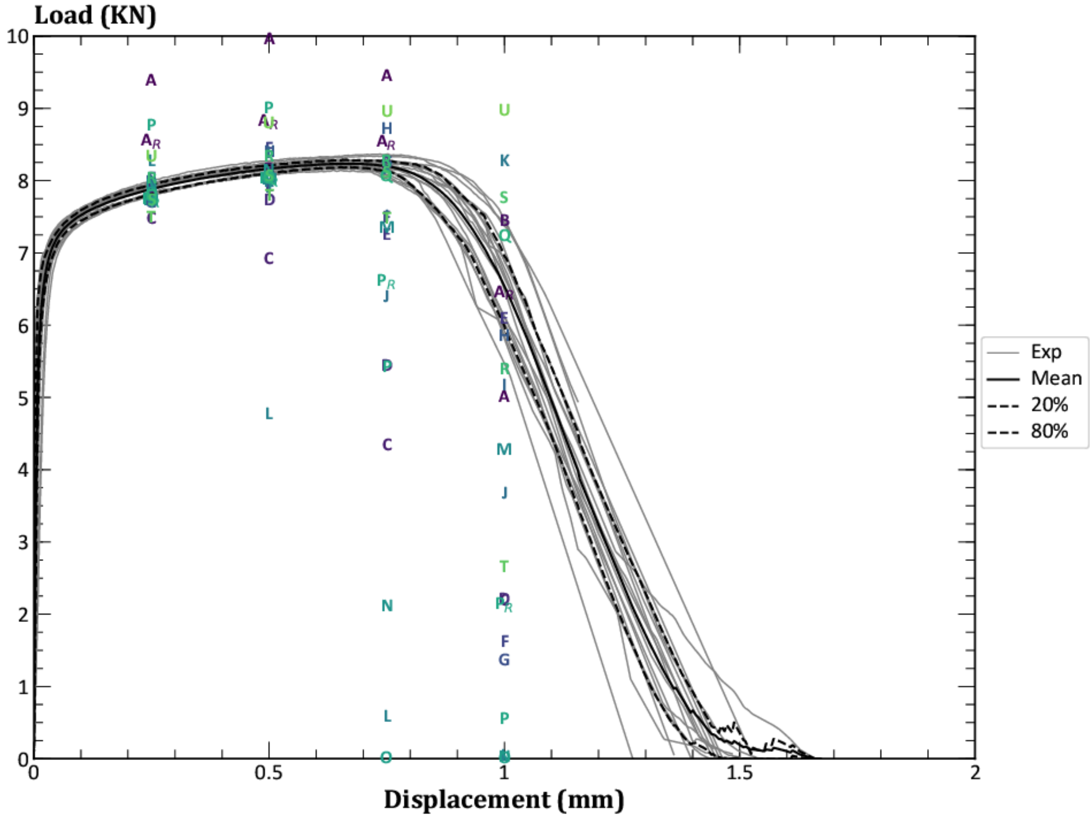

Figure 25: Predicted nominal loads from participants plotted against experimental measurements over the load-displacement range. This figure includes two revised predictions marked by a subscript "R".

At the increasing deformation levels of 0.75 mm and 1.00 mm, this close agreement generally ceases between predictions and measurements with a few exceptions. Two teams (B and Q) predicted load levels within experimental bounds at all four loading levels. However, most teams predicted damage initiation too early in the load-displacement response; this resulted in load levels below measured values. Well into the damage process at 1.00 mm, there is a range of predictions from 0 to 9 kN vs. the experimental measurement of 6.5 kN. Despite variability in predictions, results shown here represent an improvement over predictions in earlier challenges. For example, all teams predicted the correct damage initiation location and failure path, and the variation shown here reflects damage process variability (e.g., how much damage at what load).

Table 11 lists nominal and bound values for each team along with the experimental measurements for Question 1. Of the teams that provided uncertainty quantification, a team's predicted bounds track with their nominal predictions, i.e., if the nominal prediction matches the nominal experimental value, then the predicted bounds usually match the experimental bounded values. This correlation reflects (most likely) dependencies on the bounded predicted of various assumptions embedded in the nominal and bounded predictions. Relative to the bounded range (i.e., the upper bound minus the lower bound), predicted bounded ranges tended to overestimate the actual uncertainty in experimental measurements. For example, there were only three predictions within 10% of the experimental bounded range out of the 40 predictions submitted by the various teams. Interestingly, predicted values of bounded ranges tended to improve with increased damage, though this may be an artifact of the spread in the loading process wherein the experimental bounds increase with deformation and damage.

Table 11: Measurements and predicted loads at four select displacements from the various teams, including revised solutions. These results represent the comprehensive results from question 1.

Displacement		Force (kN) at 0.25 mm			Force (kN) at 0.50 mm			Force (kN) at 0.75 mm			Force (kN) at 1.00 mm		
Type		20%	Nom.	80%	20%	Nom.	80%	20%	Nom.	80%	20%	Nom.	80%
Measurements		7.814	7.884	7.942	8.098	8.164	8.214	8.142	8.203	8.276	5.985	6.538	6.956
Initial Predictions	A	N/A	9.376	N/A	N/A	9.948	N/A	N/A	9.445	N/A	N/A	5.005	N/A
	B	7.764	7.892	8.021	8.026	8.159	8.293	8.093	8.233	8.369	6.860	7.430	7.738
	C	7.115	7.469	7.829	6.502	6.919	8.046	3.685	4.330	6.476	1.785	2.188	3.515
	D	7.693	7.842	7.931	7.518	7.726	7.931	4.852	5.430	6.130	0.979	2.195	3.265
	E	N/A	7.784	N/A	N/A	7.917	N/A	N/A	7.250	N/A	N/A	6.083	N/A
	F	8.030	8.027	N/A	7.771	8.434	N/A	3.497	7.485	N/A	0.189	1.615	N/A
	G	N/A	7.690	N/A	N/A	8.021	N/A	N/A	8.241	N/A	N/A	1.358	N/A
	H	7.982	7.983	7.982	8.380	8.393	8.380	8.689	8.716	8.710	4.043	5.839	8.707
	I	N/A	7.974	N/A	N/A	8.368	N/A	N/A	7.503	N/A	N/A	5.166	N/A
	J	N/A	7.910	N/A	N/A	7.901	N/A	N/A	6.391	N/A	N/A	3.659	N/A
	K	N/A	7.706	N/A	N/A	7.972	N/A	N/A	8.150	N/A	N/A	8.264	N/A
	L	8.030	8.269	8.508	2.547	4.762	6.978	0.000	0.576	1.705	0.000	0.039	0.238
	M	7.530	7.728	7.899	7.858	8.003	8.157	6.546	7.345	8.042	1.759	4.277	6.988
	N	N/A	7.935	7.992	N/A	8.131	8.160	N/A	2.106	6.447	N/A	0.026	1.574
	O	N/A	7.823	N/A	N/A	8.034	N/A	N/A	N/A	N/A	N/A	N/A	N/A
	P	8.333	8.755	8.747	8.717	9.002	9.117	4.607	5.416	8.052	0.146	0.539	3.355
	Q	7.685	7.786	7.913	7.920	8.032	8.161	7.914	8.057	8.196	6.795	7.235	7.738
	R	7.952	8.019	8.085	8.274	8.324	8.375	7.938	8.257	8.614	2.714	5.385	7.961
	S	7.685	7.725	7.756	8.023	8.056	8.083	8.078	8.100	8.120	7.741	7.751	7.758
	T	N/A	7.480	N/A	N/A	7.780	N/A	N/A	7.469	N/A	N/A	2.645	N/A
	U	N/A	8.322	N/A	N/A	8.792	N/A	N/A	8.946	N/A	N/A	8.959	N/A
Revised	A_R	N/A	8.540	N/A	N/A	8.815	N/A	N/A	8.519	N/A	N/A	6.448	N/A
	P_R	7.351	7.729	7.913	7.660	8.009	8.020	6.035	6.600	7.839	1.492	2.124	5.181

Nominal predictions for load-displacement curves from all participants have been plotted against experimental measurements as shown in Figure 26. As described in the preceding paragraphs, most participants under-predicted the ultimate tensile strain and the strain at failure, highlighting the challenge in accurately modeling damage and failure in metals in general and additively manufactured components in particular. Similar to the experimental load-displacement measurements, most variation in predictions occurred in the softening region of the load-displacement curve after damage processes were activated. This large variation in softening behavior could come from, for example, the choice of damage law and failure criterion and how the parameters for those models were determined. For reference, the modeling approach each team chose is reported in Section 4. Prior to plastic deformation, most teams predicted lower elastic stiffness (higher compliance) than measured in the test coupons. Most participant results compared well up to ultimate tensile strain, and while there was some variation in predicted yield stress, hardening moduli predictions were qualitatively close to the experimental data.

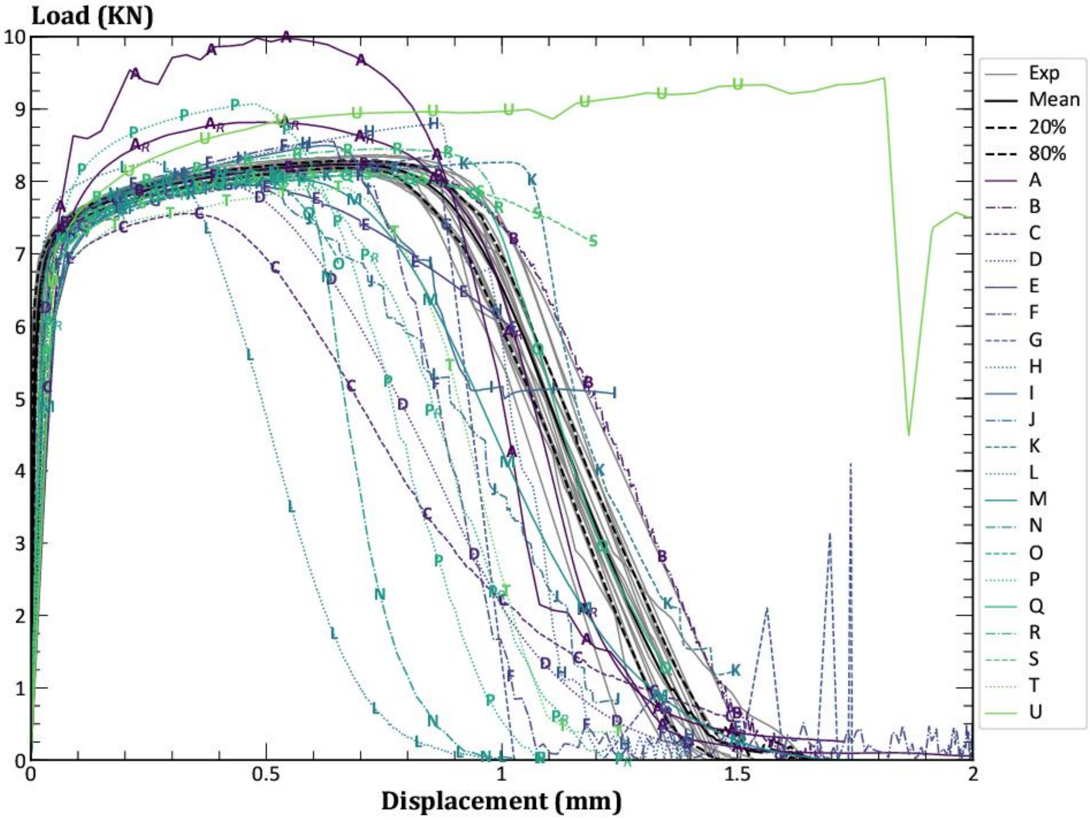

Figure 26: Average load-displacement predictions compared to the experimental results.

Figure 27 shows individual predictions on a team-by-team basis including uncertainty bounds where applicable. Figure 27 highlights variability in the predictions of the individual teams, e.g., steady ductile tearing with increasing loads vs. a sharp load drop. Furthermore, this figure emphasizes prediction uncertainty that is not shown in nominal results. Uncertainty bounds from the experimental measurements remain nearly symmetric about the nominal prediction. In most predictions, nominal prediction skews towards one of the two bounds. That is, the uncertainty quantification techniques employed by the teams artificially skew the load-displacement curves.

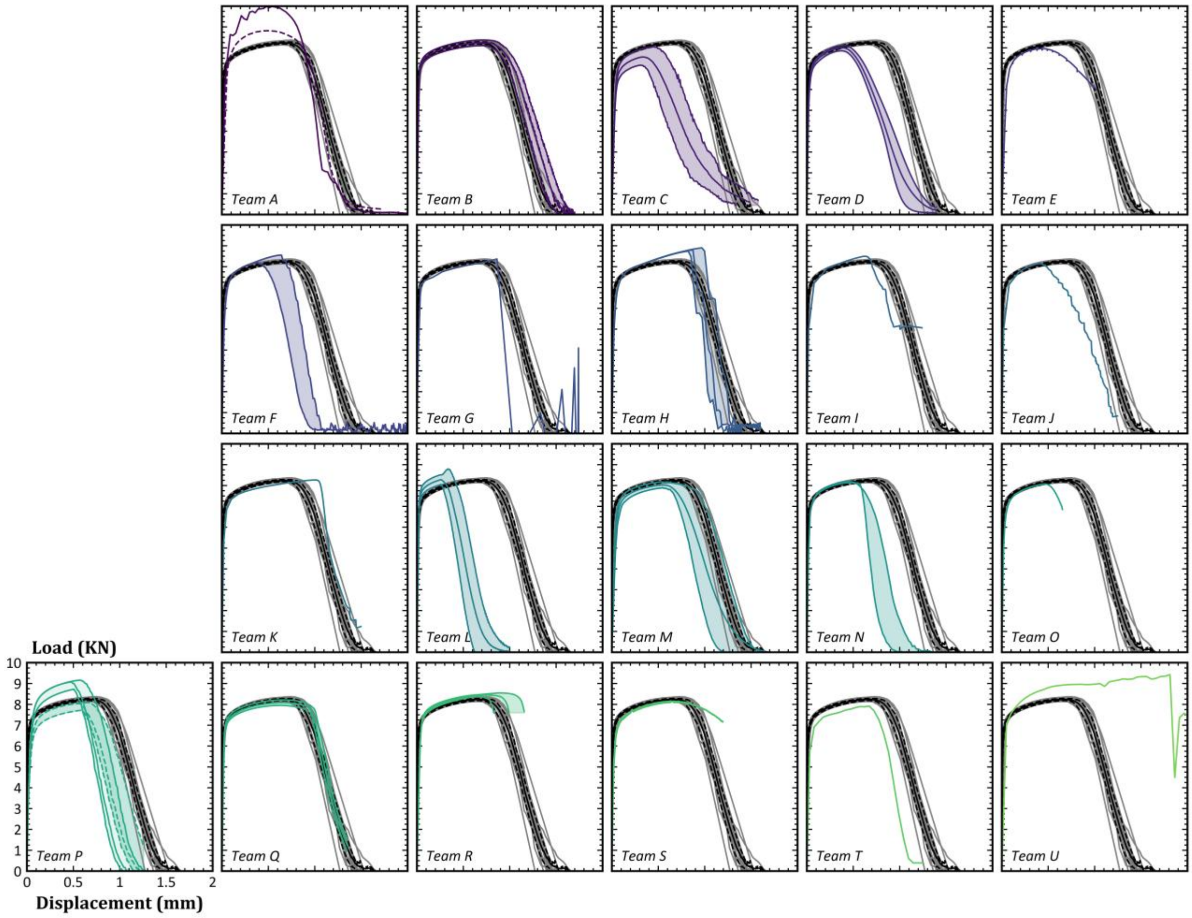

Figure 27: Predicted load-displacement curves from each team compared against experimental measurements. Banded curves show uncertainty bounds provided by the individual teams. Colored dashed lines indicate revised predictions from Team A and Team P.

5.2 Questions 2 and 4: Loads vs. strains

The second and fourth challenge questions ask participants to report simulated loads against vertical strains at the four locations (P1, P2, P3, and P4) of the challenge geometry. These locations reflect potential damage initiation sites at the spherical void (P1), the elliptical cross-section (P2), and near the intersecting circular holes where damage actually initiated (P3/P4). Nominally, locations P3/P4 are symmetric about the centerline, and most of the participants included this nominal symmetry in their predictions. Once again, participants were encouraged to provide bounds for their results. In the requested data file format, strains, loads, and displacements were to have been provided on the same row, and the strains in questions two and four are not completely independent of the displacements in questions one and three as a result.

For question two, loads were defined relative to the peak load and indicated when strains should be recorded at the various locations. Predicted peak loads were within 30% of the measured nominal peak load, though few predictions fell within the experimental uncertainty bounds. However, predicted strains deviated by orders of magnitude from measured strains, especially in the early stages of loading (F1) prior to plastic deformation, i.e., in the linear-elastic regime. Predicted strains values align more closely with measured strains values as damage increases. It is unclear if better agreement signifies more significant figures, more accurate measurements, more accurate mechanics, differences in material inhomogeneity, or the marginalization of some other factor at higher strains, e.g., residual stress or surface roughness. Overall, predicted strains tend to be lower than measured strains.

A brief overview of results from question two will illustrate key trends. It is sufficient to examine trends for F3 (shown in Figure 28) since loads F1, F2, F3, and F4 were defined relative to load F3. Team B and Team K predicted nominal peak loads (F3 values) within the experimental bounds; the revision prediction from Team L was also within the experimental bounds. Teams B, F, M and Q (and Team L with the revised prediction) predicted 20th and 80th percentile ranges that overlapped with the experimental 20th and 80th percentile ranges. Eight teams over-predicted average F3 values above the 80th percentile, and eleven initial predictions had average F3 values below the experimental 20th percentile. However, experimental bounds remained relatively tight at less than 0.1 kN despite the AM process. Consequently, most teams predicted peak loads within 5% of the measured peak loading; displacement at peak load instead represents a better measure of model fidelity, though it was not one of the challenge questions.

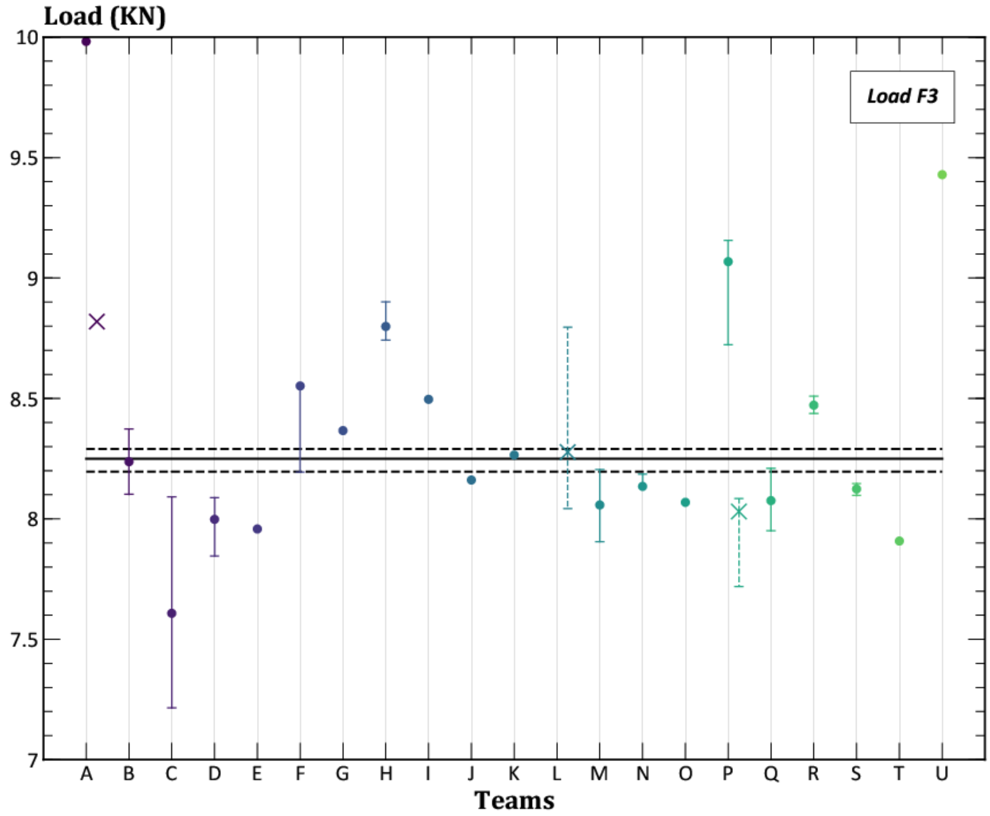

Figure 28: Predicted peak loads (F3) plotted team-by-team against experimental bounds. The mean experimental peak load is shown as a solid line, and the 20th/80th percentile bounds are presented as broken lines. For each team, the solid dot indicates a team's expected value, and the uncertainty bounds are plotted, if provided. Revised predictions have been indicated by X's.

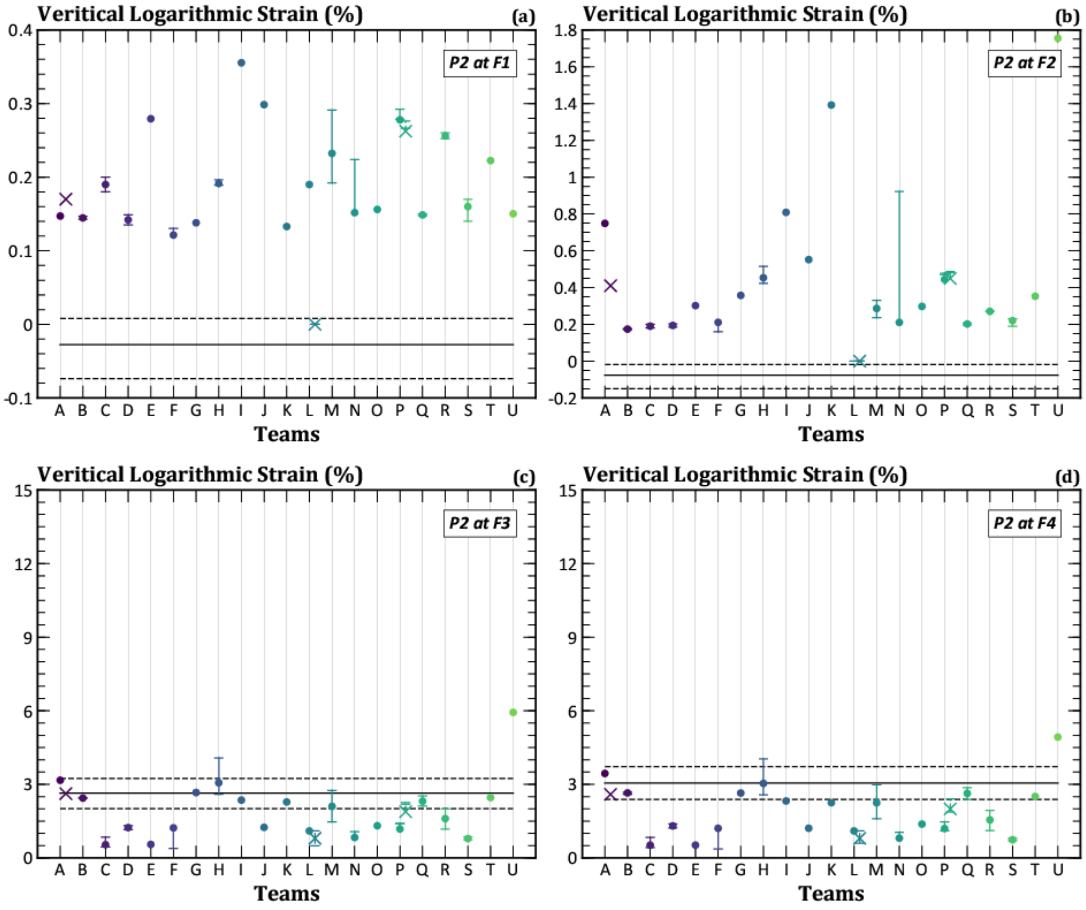

Figure 29: Predicted strain at P2 plotted team-by-team against experimental bounds. The mean experimental strains are shown as a solid line, and the 20th/80th percentile bounds are presented as broken lines. For each team, the solid dot indicates a team’s expected value, and the uncertainty bounds are plotted as well. Revised predictions have been indicated by X’s. Strains have been plotted on a load-by-load basis.

Figure 29 presents discrete strain values at location P2 from the second question. Similar plots may be found in Appendix 2 Figure 111, Figure 112, and Figure 113 for points P1, P3, and P4, respectively. The vertical logarithmic strain at location P2 for load F1 (in the elastic regime) indicates that none of the original predictions fell within the experimental bounds. Instead, all of the original predictions over-predicted the logarithmic strain value. The experimental logarithmic strain 20th to 80th percentile values ranged from -0.000739 to 0.000079, while all of the reported predicted logarithm strain averages and 20th and 80th percentiles were non-negative. That is, positive (tensile) loads produced negative (compressive) strains in the experimental record, but not in the team predictions for this location (P2) and only this location, i.e., not at P1, P3, and P4. This may speak to the surface strains being greatly affected by surface effects (roughness and residual strain) that may have reduced the surface strain in this geometry as compared to a similar part with a smooth, residual stress-free surface. It is tempting to account for these negative strains on bending from grip misalignment, but the two specimens, A18 and A24, that were tested using a swivel joint to minimize grip misalignment still had negative surface strains at P2. These observations must be made in the context of these small strains being near the noise floor of the DIC strain measurement capabilities (see Table 3 and Table 8). Agreement between predictions and measurements increases with increased loading. At peak load (F3), several predictions featured an average logarithmic strain value that fell within the experimental 20th and 80th percentile logarithmic strain values. Of the predicted percentile ranges that did not overlap with the experimental percentile ranges, one predicted range (Team U) over-predicted while the remaining under-predicted.

At location P1 shown in Figure 30, most teams captured the major features of the experimental response prior to damage initiation – an initial linear-elastic regime prior to plastic initiation and a smooth transition into the elastic-plastic regime. Also, everyone replicated the sharp load-drop at P1 that reflects unloading as strain localizes near locations P3/P4. Fifteen teams under-predict the strain at failure. Teams that predicted the correct load-displacement curve in question three (Team B and Team Q) did not necessarily predict the correct load-strain curve in question four, and vice versa (e.g., see Team M and Team T). Predicted uncertainty bounds prior to damage follow the trends observed in question three, and they tended to be narrower than the uncertainty bounds in the measurements post damage.

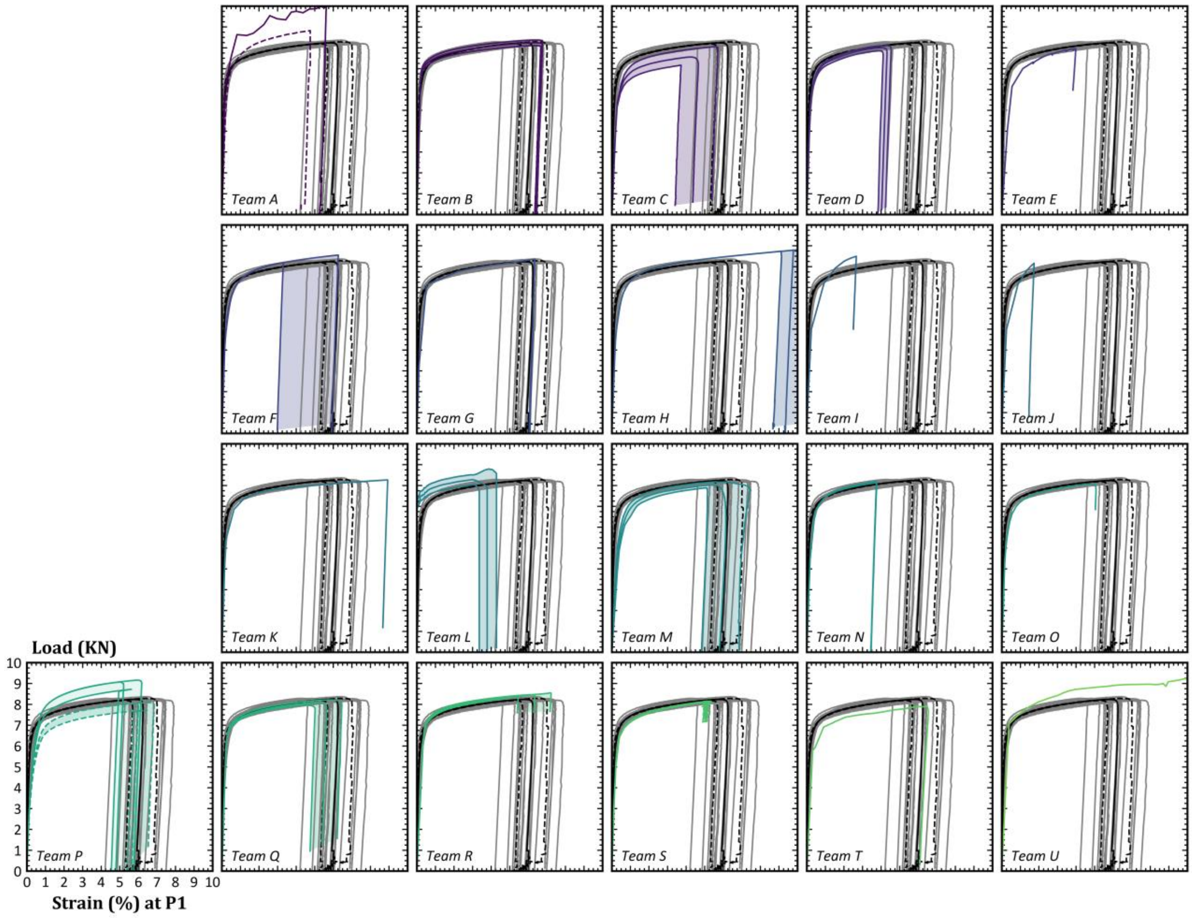

Figure 30: Predicted load-strains curves from individual team against experimental measurements at point P1. Banded curves show uncertainty bounds provided by the individual teams. Colored dashed lines indicated revised predictions.

At location P2 shown in Figure 31, there is an early discrepancy. Predictions and measurements diverge in the elastic regime prior to plastic deformation. Team predictions show increasing tensile (positive) elastic strains with increasing tensile load, but experimental measurements reveal increasing compressive (negative) elastic strains with increasing tensile load. Post-yield, both team predictions and experimental measurements show the expected trend of increasing tensile strains with increasing tensile loads. Once again, the team predictions skew towards lower final strains at zero load than higher final strains. All but three of the nominal predictions have lower strains-at-failure than the experimental measurements. Lower strains at P2 at specimen failure suggest reduced plastic deformation during the elastic-plastic regime leading up to the peak load. Predicted uncertainty bounds again underestimate the amount of final strain uncertainty in the post-damage regime.

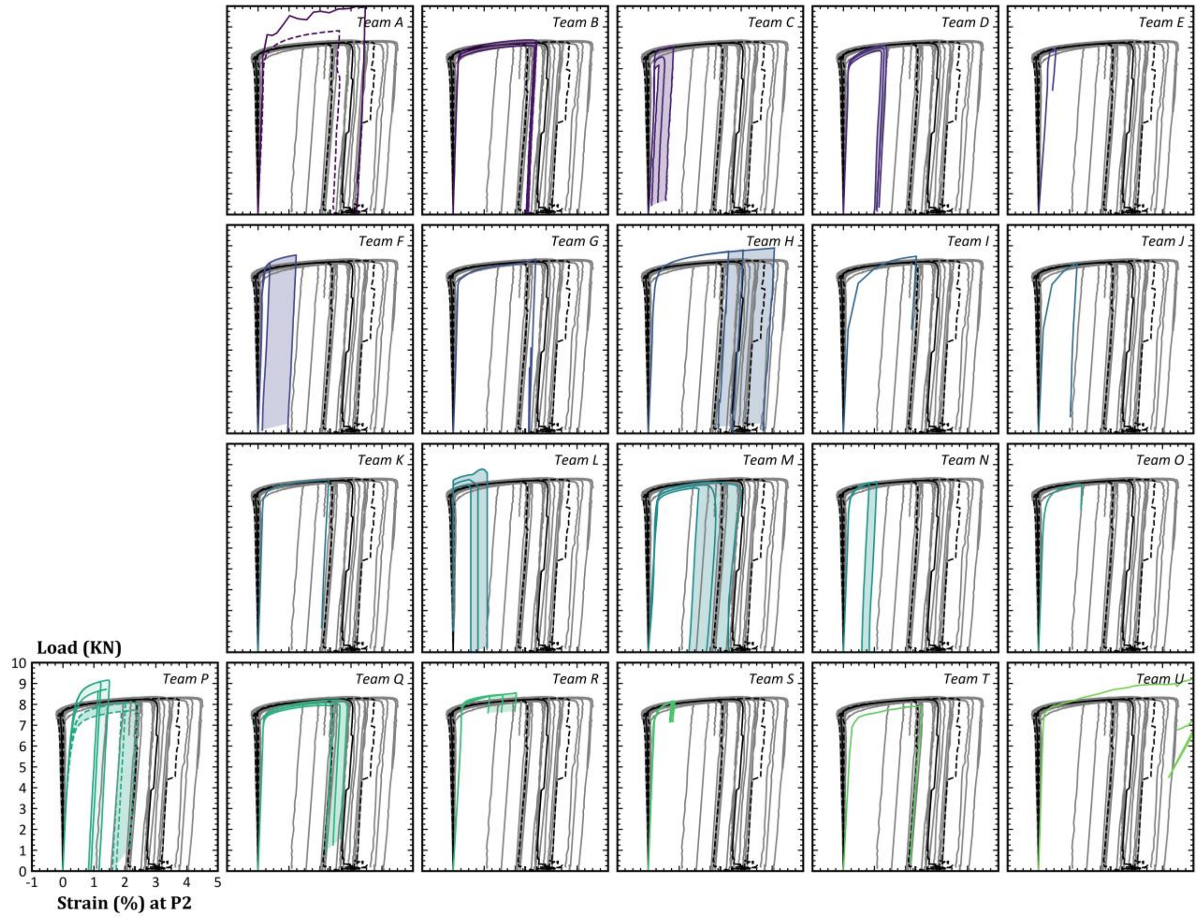

Figure 31: Predicted load-strains curves from individual teams against experimental measurements at point P2. Banded curves show uncertainty bounds provided by the individual teams. Colored dashed lines indicated revised predictions.

Results at locations P3/P4 indicate damage propagation as it advances from the corners towards these locations. These results are shown in Figure 32 and Figure 33. With a few exceptions, most teams predicted the general experimental response – increasing surface strain with increasing load prior to peak load; gently decreasing load with increasing strain at the intersection of the through-hole and angled channels after peak load; and then rapid unloading due to the damage evolution around P3/P4. Most teams also submitted identical predictions for P3/P4, and this assumption may be justified due to the limited variation of measurements at P3 vs. P4. (It is unclear if the nominal experimental variations are statistically significant or not.) Nineteen of the teams predicted lower nominal strains at P3/P4 at specimen failure than were measured at P3/P4. These results may suggest increased deformation near free surfaces, e.g., Team B and Team Q predicted load-displacement curves well but have lower magnitudes of strain-at-failure. Predicted uncertainty bounds again under-estimate the amount of uncertainty in the measurements. Furthermore, measured uncertainty in strains peaks below 5 kN at P3 and above 5 kN at P4. None of the team predictions show this variation at point P3/P4, though several teams showed more uncertainty above or below the 5-kN limit.

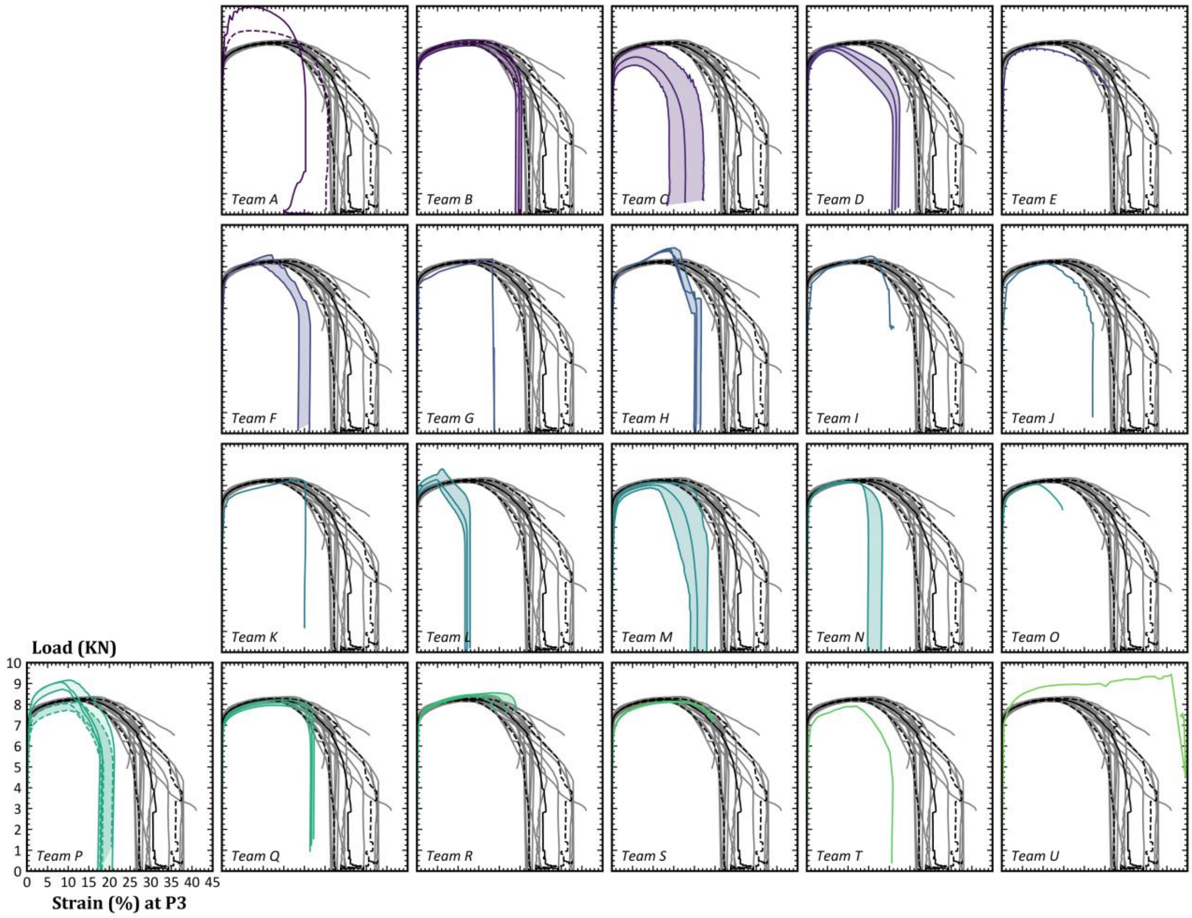

Figure 32: Predicted load-strains curves from individual team against experimental measurements at point P3. Banded curves show uncertainty bounds provided by the individual teams. Colored dashed lines indicated revised predictions.

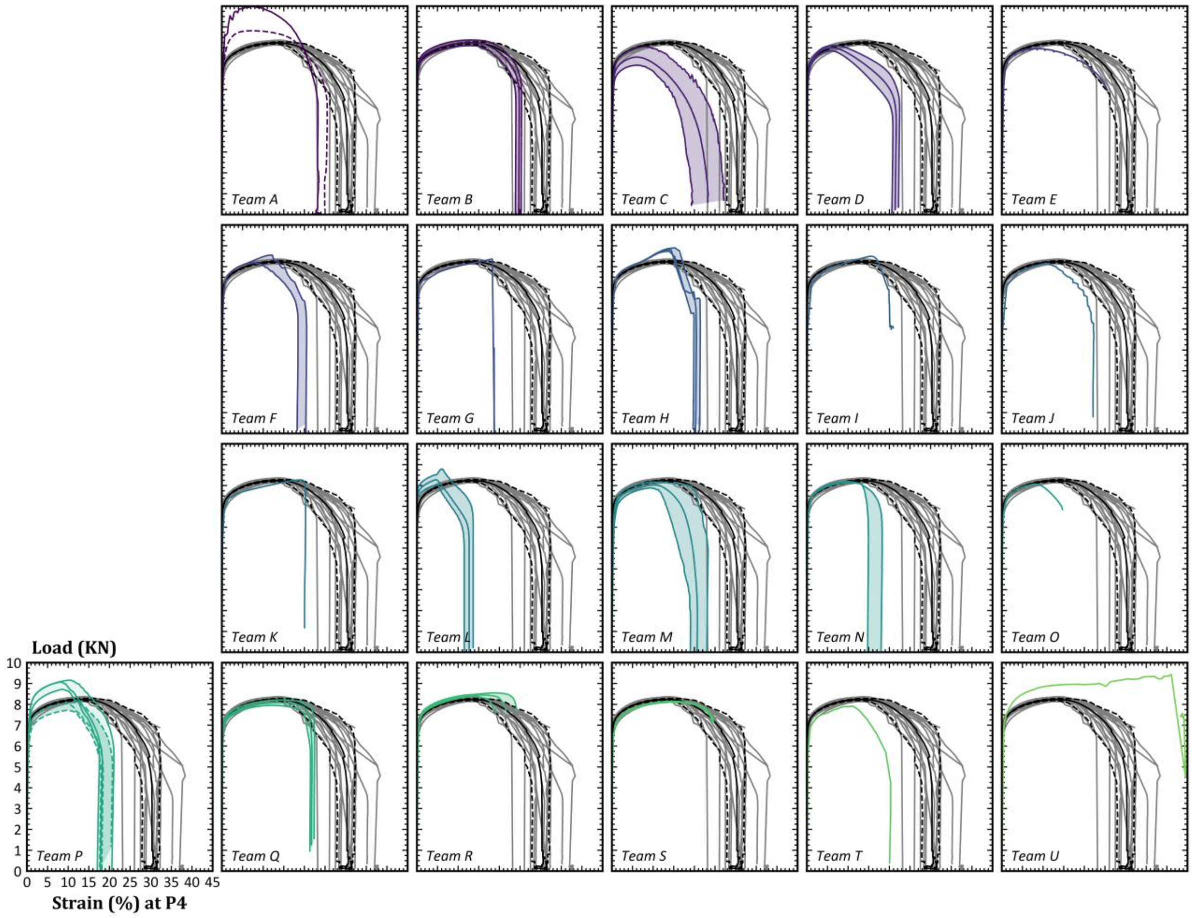

Figure 33: Predicted load-strains curves from individual team against experimental measurements at point P4. Banded curves show uncertainty bounds provided by the individual teams. Colored dashed lines indicated revised predictions.

5.3 Question 5: Load-strain curves on lines

The fifth question asked participants to predict strains along four lines at the four loading levels F1, F2, F3, and F4. Line H1 lies above the spherical cavity, line H2 lies on the elliptical hole, and lines H3 and H4 bound the fracture region. All of these regions feature some plasticity and damage that tends to concentrate along lines H3 and H4. Overall, this question led to more problematic data issues than the other questions. Many of the anomalous results represent reporting issues and are not reflective of the techniques employed by the various participants as shown by their revised predictions. It should be noted that line H4 features a hole, and there were several approaches to reporting data in this empty region, including empty entries, NaN values, zeros, and constant strains between free surfaces. Without context (i.e., the geometry), these data values may be misinterpreted, and future challenges may be improved by defining non-existent values a priori.

At the lowest load level (F1), there is a large spread of strain measurements prior to plastic deformation in the tested samples. Measured strain values have an asymmetrical distribution with higher on the right side of the specimens (“X” approaching 6.0 mm) than on the left side of the specimens (“X” approaching 0 mm) At this loading level, predicted strains remain larger than nominal strain values determined using DIC methods along all lines. Along lines H1 and H2, several teams predicted local maxima not shown near thinner sections that do not appear in the experimental measurements (see Appendix 2 Figure 118(a) and Figure 119(a)). None of the teams predicted negative strain values along line H1 at load F1. Along lines H3 and H4, most teams predicted local peaks/valleys that trend with DIC measurements (see Appendix 2 Figure 120(a) and Figure 121(a)).

As the load increases from F1 to F2, predictions increasingly align with the measurements (see Appendix 2 Figure 118(b) through Figure 121(b)). The measured strain asymmetry disappears, and the mostly symmetric predictions capture the peaks and valleys along the four lines. Several predictions are within experimental bounds at this loading level. Interestingly, the most accurate predictions were provided along line H3 below the stress concentrating feature.

At peak load (F3), predictions have the best agreement with experimental measurements, particularly in the yielding but not damaging regions of H1 and H2 (see Appendix 2 Figure 118(c) and Figure 119(c)). That is, prior to significant damage initiation, most teams could predict the nominal trend near measured strains. Along line H3 (shown in Figure 34), most teams captured the shift of the peak strain location at load F3 from an interior location to the free surface. Capturing this peak location shift correlates with increased deformation prior to damage initiation, i.e., predictions with low displacements at peak load generally did not capture the shift. Team-to-team differences in the predictions increased most along line H4 (shown in Figure 35) where damage initiates. While several teams were unable to remain within experimental bounds with increasing loads, a few teams maintained very good agreement up to peak load. All of the teams captured the strongly increasing strain gradient approaching the hole, but they differed in the magnitude of the strain concentration.

After damage initiations at load F4, measured strains increase along line H4 (the damage process zone) and remain relatively constant along lines H1, H2, and H3. Predicted strains capture this trend, but only a few groups predicted strains within the experimental bounds. Typically, predicted strains underestimate strains in the damage process zone relative to the experimental values. In summary, the predictions overestimated strains early in the deformation at F1, predicted reasonably well at F2 and F3, but generally underestimated at F4, which are observations consistent with the points locations of Question 2. Question 5 also tell us that the predictions generally captured the shape of the strain gradients along the four lines of interest, though the actual values were not accurate early and late in the deformation.

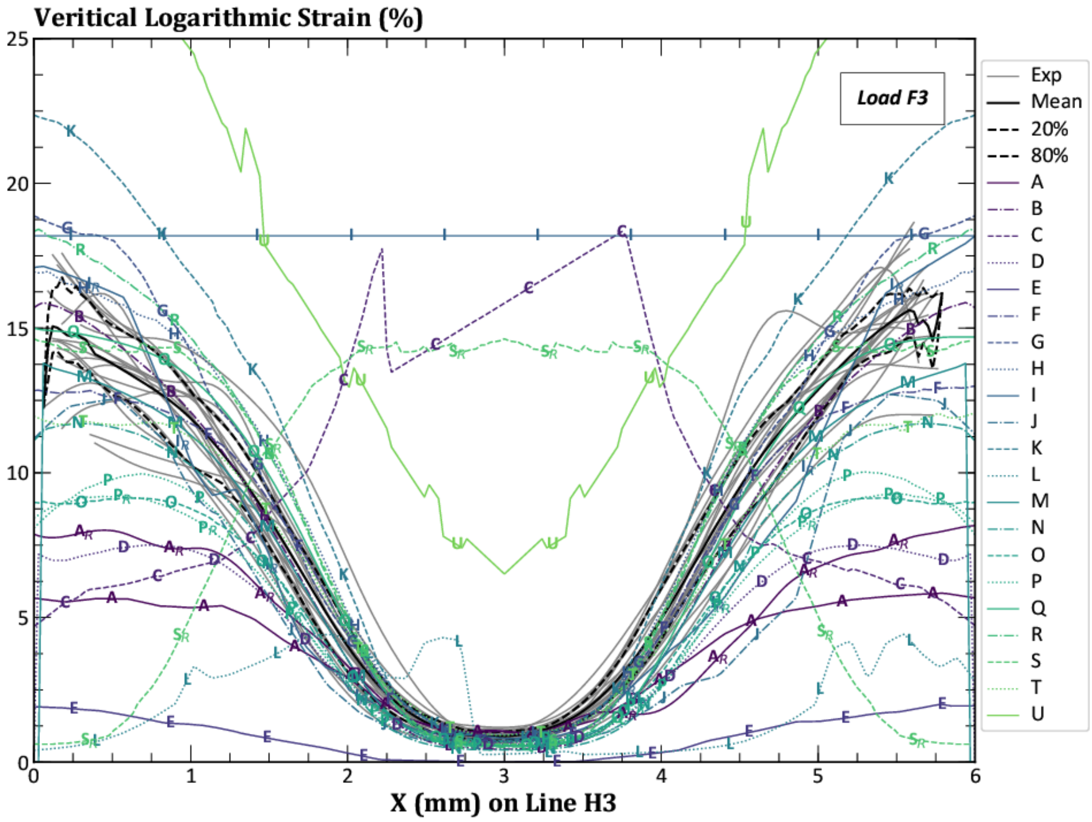

Figure 34: Average vertical strain predictions compared to the experimental results at peak loading (F3) on line H3.

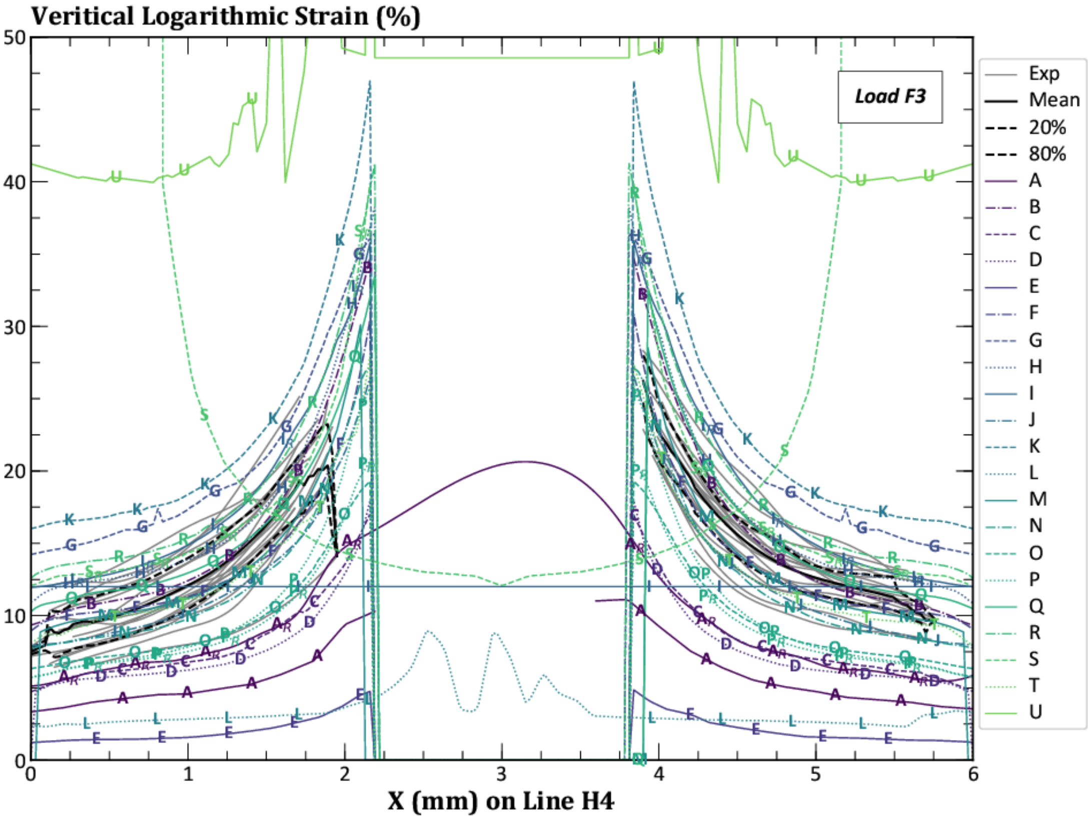

Figure 35: Average vertical strain predictions compared to the experimental results at peak loading (F3) on line H4.

5.4 Question 6: Strain contour plots

The sixth question asked participants to provide images of the logarithmic strains in the vertical direction at crack initiation and complete failure. However, the question did not specify a color scale, color limits, mesh visibility, etc… in the challenge announcement, and participants freely choose these options in their submissions. For example, most participants choose a rainbow color scale (default in Abaqus) while other participants adopted a red-white-blue scale (default in Paraview). In particular, the color limits were not specified as to not bias the participants' predictions. As a result, the submissions and comparison presented here are of more qualitative value than quantitative value.

The corresponding simulation prediction results are shown for all participants in Figure 36 for crack initiation and in Figure 37 for complete failure. These images represent nominal values. Two features are important to note: (1) all teams predicted failure in the correct location and (2) the majority of the simulations predicted failure paths directly following the upper, angled channels in the challenge specimen while there is more crack path variability in the challenge specimens.

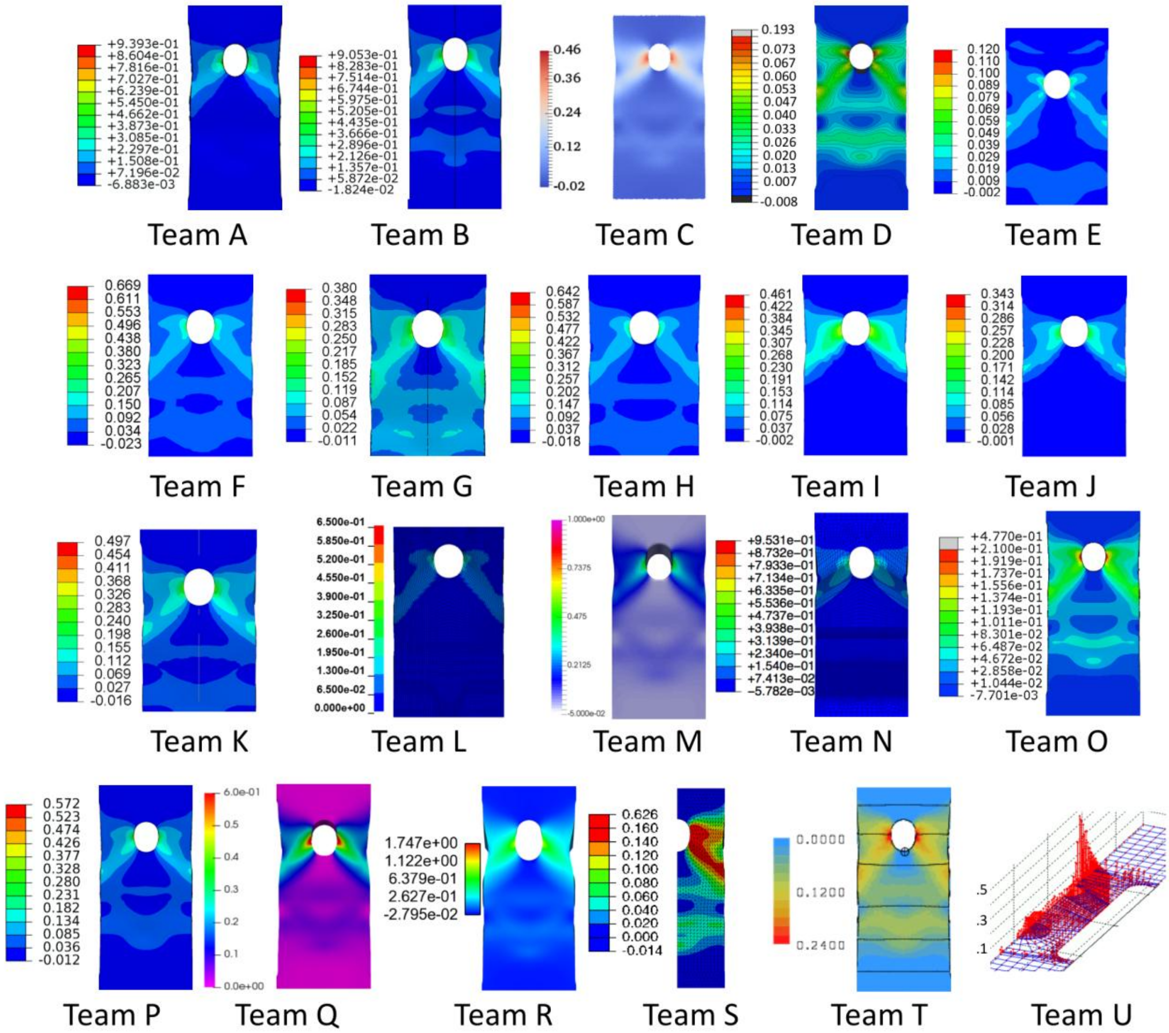

Figure 36. The submitted simulation predictions showing the logarithmic strains in the vertical direction for the challenge specimen at crack initiation.

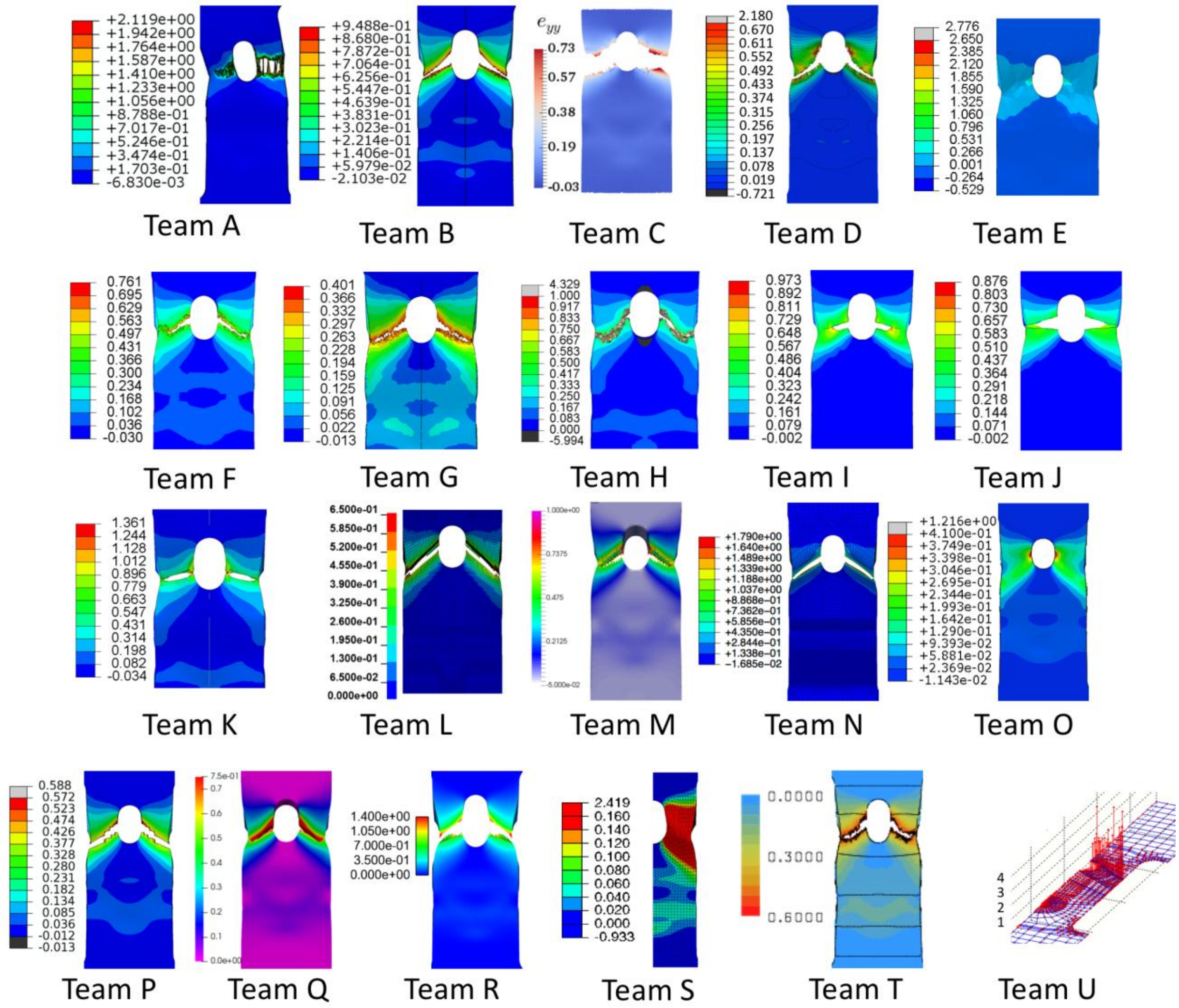

Figure 37. The submitted simulation predictions showing the logarithmic strains in the vertical direction for the challenge specimen nearest to complete failure. If complete failure is not observed, these figures indicate strains when the simulation was terminated.

6 Discussion

6.1 Summary of Results

As with previous Challenges, the experimental testing of the SFC3 Challenge geometry was completed in two independent laboratories to determine if testing approaches biased the results. Here, the only shared items were the grips and the details of DIC parameters (pixel-to-length ratio and subset, step, and strain filter sizes). The comparison of DIC results between test setups can be difficult if care is not taken to match the virtual strain gauge sizes of the two setups so that the strain measures can be compared between the two laboratories. Each laboratory was otherwise given the freedom to interpret and execute the testing parameters independently, from load cells to cameras for DIC. As shown in Section 4, the experimental results were consistent between the two laboratories. The failure location was the same, the global load versus DIC-generated gauge displacement overlapped, and the local DIC strains had the similar contours and relative quantities. This implies that the individual setups, both for loading and for DIC, did not negatively bias the results, allowing for all data collected in the two laboratories to be combined and used as the basis for comparison to the computational predictions.

It is important to reemphasize that in SFC3 there was only one observed failure mode, allowing all global and local quantities of interest to reflect the behavior leading to one failure mode, providing a reasonable population size of nineteen observations to inform the uncertainty quantification. In the previous two Challenges, two competing failure modes complicated the comparison of experimental and computational results. In SFC3, the details of the exact location of the crack initiation (right or left side of the nominally symmetric geometry) and crack propagation can be discussed in terms of the stochastic nature of ductile fracture and the defects of the AM structure.

The SFC3 participants generally fared better in their global predictions of deformation and failure than the participants in the previous Challenges. All teams predicted the correct failure path, perhaps due to a few factors: experience gleaned from previous Challenges, straightforward boundary conditions, and a Challenge geometry without competing failure modes. Unexpectedly, the elastic response in the predictions of the load versus gauge displacement behavior tended to be slightly low, but the difference was to a lesser degree than in SFC2 where there was considerable overprediction of stiffness. Explicit studies of this discrepancy were not conducted, but one hypothesis is that the models did not account for residual stress, which was not measured in these parts, but is commonly found in AM parts (Wu et. al. 2014). Nearly all teams predicted load versus gauge displacement behavior with plastic behavior (seen in good agreement in the load-displacement curve and strains away from the failure regime in H2, for example). The greatest differences were in the displacement at peak load and the displacement after peak load during failure, which is not surprising because the predictions diverge as the cumulative effects of the varied modeling choices stack up in the load-drop regime. Amidst this variability, two teams (B and Q) predicted nominal load versus displacement behavior within the experimental bounds through failure. Though the details of these two teams' approaches differed, both teams went to great lengths to carefully calibrate sophisticated plasticity and failure models, incorporating anisotropy and/or strain-rate dependence, and used small element sizes. These two teams chose different approaches in capturing variability, either through the constitutive and failure models or through the Challenge geometry, affecting their uncertainty quantification. More detailed analysis of best practices amongst all the teams will appear later in the Discussion section.

The ability of all the teams to reasonably predict the global behavior of the Challenge geometry is encouraging. First, a number of different computational approaches gave similar global results, pointing to maturity of the models used and to the adoption of best practices described in previous Challenges. Second, most teams did not treat the AM material differently than they would have treated a wrought material, yet they were able to predict global behavior. This speaks to the relative insensitivity of the Challenge geometry to the variability from the AM process. The tensile and notched tensile specimens had considerable variability in failure due to the AM material; geometry of these samples did not have large stress concentrations, and the surface roughness and voids were key players in the stochastic failure. On the other hand, the structural response to the large stress concentrations in the Challenge geometry appears to have overwhelmed the local responses to the surface roughness and voids, leading to less variability in global behavior than in the calibration experiments. Considerable research efforts on optimizing geometric topology of AM parts often lead to organic-like structures with thin members akin to the SFC3 tensile specimens where failure can occur in many locations, driven by surface roughness and voids. Understanding that an AM structure is more tolerant of surface roughness and voids when larger stress concentrations drive failure can lead to new approaches to design of AM structures with features that dominate the structural failure response, allowing for predictable failure behavior.

Third, the general orientation of the challenge geometry was aligned with the direction of the longitudinal samples for the model calibration. If the challenge geometry had deformation of a more biaxial nature or in direction intermediate between transverse and longitudinal direction, the response from the different isotropic models may have been less accurate. That being said, we see here that reasonable predictions may be obtained from models calibrated using traditional specimen configurations (i.e., uniaxial tension tests). Most legacy data are load-displacement curves and/or stress-strain curves from uniaxial tension tests. This information remains the most relevant information to calibrate elastic-plastic-damage models. Furthermore, it may not always be necessary to develop new specimen configurations (e.g., a dual keyhole specimen) for shear dominated plasticity and damage models. These novel specimen configurations are not included in standardized testing specifications and often require additional interpretation/analysis to determine relevant parameters. Fourth, the tensile and notched tensile specimens were made during the same build as the Challenge geometry, which implies that the teams were calibrating their models using data from material with similar porosity, residual stress, and surface roughness. The ability of most of the teams to predict strains away from the damage (namely along H1 and H2) implies that the plasticity was generally done well, enabled by calibration data from specimens built at the same time as the Challenge specimens. Interestingly, the material properties provided by the commercial vendor (Table 1) were very different than the as-manufactured 316L (Figure 3). This highlights the importance of calibrating models with as-manufactured materials and not database information.

In SFC3, the inclusion of local QOIs has afforded a new way to assess the predictions against the experimental observations. In general, the teams tended to over-predict surface strains early in the deformation and then under-predict surface strains late in the deformation. These local QOIs would be influenced by the local structure (surface roughness, residual strain, voids near the surface, etc.). Though the teams were not given residual stress data, they were given extensive microstructural data that were largely left unused for a whole host of reasons such as complexity and size of a model with void and surface details and limited time to incorporate such details. We do not know if inclusion of these details would have improved the predictions of local deformation.

The crack paths of the Challenge geometry specimens were generally located along the upper portion of the specimens, first experimentally observed on the surface at the through-hole and propagating along the adjacent angled channels, but the crack initiation location and the paths were not precisely the same between specimens. Some specimens had more horizontal crack paths, while others followed the angle of the channels. These variations were most likely due to the voids located near the large features that cause the crack path to deviate. Indeed, as discussed in detail in Kramer et. al. 2018, interrupted tests of the Challenge geometry with micro-CT scans between load steps revealed cracks formed at the interior corners at the intersection of the through-thickness hole and angled channels well before peak load, though cracks on the front surface did not appear until after peak load. The micro-CT scans showed that the cracks intersected pre-existing voids, leading to the varied crack paths between specimens. No team explicitly modeled the voids found in micro-CT scans, so that variability was not captured in their predictions.

Another new assessment tool is the optional reporting of specific uncertainty bounds (previous Challenges allowed for the reporting but did not specify the type). The nominal, 20th percentile, and 80th percentile values for forces, displacements, and strains were intended to capture the distribution based on the nineteen experimental observations. Additionally, requesting these values would query how the teams accounted for the inherent variability in the Challenge. In the experimental data, the bounds on the data tended to be relatively tight globally but varied more locally. The large variability in the local strain measures is not surprising for an AM structure. The less prominent variability in the global measures like in the load versus displacement response was not originally expected for an AM part, but as previously discussed, the large intentional features in the Challenge geometry appears to have tempered the variability of the global response.

Twelve out of twenty-one teams reported uncertainty bounds with their predictions, similar in absolute number to the twelve out of fourteen teams with uncertainty bounds for SFC2. As discussed in Section 4, the teams took several different approaches for making uncertainty bounds from simple variation of the material model parameters to Monte Carlo simulations that varied material, geometry, and loading parameters. The complexity of the uncertainty quantification approaches did not necessarily correlate with improved uncertainty bound predictions, likely due to the underlying nominal modeling choices having greater effect on the overall prediction. In other words, a quality nominal prediction is the foundation for reasonable uncertainty bounds. Generally, the range of the 20th and 80th percentile uncertainty bounds on the predicted global load-displacement were close to the range of that of the experimental data. The range of the uncertainty bounds on the strain data tended to be too small, perhaps because the predictions did not account for the local variability from the AM surface.

6.2. Provided data vs. required data

Based on experience from previous challenges, it was clear that teams would use different approaches to constitutive and failure modeling, and hence would require different types of calibration data. Thus, the formulation of the challenge required the anticipation of data that might be required for establishing the basis for material modeling. The data set provided was extensive. Detailed geometric data on the specimen dimensions was provided both for the specimens tested to provide material calibration data as well as the challenge specimens. Mid-plane cross-section images and porosity distributions were provided for longitudinal tensile specimen LTA21 (Figure 4), notched tensile specimen NA24 (Figure 9) and challenge geometry specimen A06 (Figure 12). Also, micro-CT scans of all of the challenge-geometry specimens were provided, including measurements of the internal geometric features. Post-test fracture shape images were provided for all longitudinal and transverse tension tests and notched tensions tests were documented to facilitate calibration of failure models. Post-test SEM images of the fracture surface was provided for longitudinal tension specimen LTA04 (Figure 5) and notched tension specimen NA05 (Figure 10). The force versus gauge displacement (engineering stress versus strain) for all calibration specimens – 20 longitudinal and 17 transverse tension tests and 23 notched tension tests – were provided (see Figure 3 and Figure 8). This large set was meant to provide adequate sampling to explore potential stochastic behavior in the additively manufactured specimens.

Quite interestingly, most of the supplied data was *not* used in the blind predictions by the teams that participated in the challenge. The longitudinal tensile data was used by nearly all teams to calibrate the elastic and plastic properties. The transverse tensile data was used only by teams that felt that anisotropy was essential to model the plastic flow; it appears from post-test assessment that a number of teams that did not predict the load-displacement response correctly attributed it to effects arising from plastic anisotropy. The notched tension tests were used by most of the teams since it provided a different triaxiality than the tension tests; typically, comparison of the predicted versus observed response was used to determine onset of failure and therefore calibrate the failure criterion. Teams that used micromechanical damage model such as the GTN estimated porosity levels, some from the x-ray data, and others simply from heuristic arguments. A number of teams accounted for stochastic variability in the calibration data by using mean and deviation of the model parameters.

Many different failure models were used in the SFC3 predictions, each with a specific set of features requiring parameterization. Though data was generated for tension and double notched tension geometries, some of the models would have benefitted from additional data from tests sampling other stress states, such as additional values of triaxiality or shear dominated behavior. In previous challenges, (Boyce et.al. 2014, and Boyce et.al. 2016) a number of teams indicated that additional information for calibration of the shear response would have been useful. Nevertheless, the fact that many teams were able to capture the essential deformation and failure characteristics of this challenge quite well with simple phenomenological models is encouraging; however, it is possible that this particular challenge was dominated by a high-triaxiality failure while the previous challenges involved significant localized shearing deformation.

6.3 Challenges for experimental - numerical comparison

When comparing experiments to numerical simulations, multiple dimensions of the similarity quantification exist. The zero-dimension comparison uses global measures (for instance force, gauge displacement, resistance) as a function of time to infer similarity. On the other end of the comparison range is the three-dimensional comparison (for instance 3D tomography displacement measurements) as a function of time which are challenging due to the inability to measure inside a dense material and accuracy of those measurements, the amount of data collected, as well as the time required for these advanced measurements. In the middle of the comparison range are one and two-dimensional comparisons for each time-step.

In this Challenge, forces, displacements, and logarithmic strains in the tensile direction were selected as Quantities of Interest (QOIs) as these values were accessible in experiments and simulations. Forces and displacements are used for a zero-dimensional comparison while the strains are compared in 2D. The global force and displacement QOIs are useful for the challenge geometry as forces and displacements were used to calibrate the material model. Therefore, these measures allow evaluating directly the calibration. In addition, these measures evolve with minor scatter in experiments. Local strains are essential QOIs for the engineers that focus on the failure location and path and on potential component shape optimizations. Moreover, the strains allow evaluating the global-local discrepancy: while most teams had similar global force-displacement curves as were observed experimentally, the local predictions and experiments varied more significantly. Hence, future SFCs might include local measures for calibration to improve the local predictions.

The second step towards comparing the deformation of a physical sample and the numerical simulation is the algorithm used for similarity quantification. The absolute deviation $\Sigma|y_e - y_s|$ or its average weight evenly each value, where y_e and y_s are the measures of the experiments and simulations, respectively, and |..| denotes the absolute value is one possible measure. A similar approach is the squared deviation which amplifies larger differences but has mathematical advantages regarding differentiability. These quantification methods are unit dependent. The relative absolute deviation $\Sigma|(y_e - y_s)/y_e|$ and the relative square deviation lead to unit-independence and -- therefore -- allow an easier aggregation of different measures. However, this quantification method leads to artifacts if individual measures increase/decrease significantly (e.g. in a tensile experiment the initial load has an elevated weight compared to final load). The coefficient of determination R^2 is also unit-independent and especially advantageous for linear-models. In the SFC3, the differences between the experimental and numerical force-displacement curves were quantified by the teams during the calibration section and in Table 12 [in this section]. These quantifications naturally require linear or cubic interpolation as both data-sets do not use the same independent axis, i.e. displacement.

The evaluation of experimental measures has additional challenges. General challenges like slip in the grips as well as bending/torsion are often identified by multi-point measures in the gauge section. Moreover, the first loading of the samples is often not representative of the elastic behavior. For this reason, the calibration experiments in SFC3 included an unloading-reloading cycle which allows quantifying the Young's modulus; however, it also results in additional data-points which complicate the evaluation of the plastic behavior. Additionally, experiments often exhibit measurements which are difficult to explain. The negative strains in the tensile direction (vertical logarithmic strain H4 at F1 in most measurements) or the infinite stiffness in the tensile experiments (e.g. Longitudinal Tensile LTA06 and LTA10) are difficult to explain by elasticity or plasticity.

DIC is the primary method to evaluate the displacements and the strains on the sample surface and this method has a number of additional challenges. DIC uses multiple image pixels to define a correlation pixel which is used to determine the displacement and -- correspondingly -- the strains by locating the correlation pixel as a function of the image sequence, i.e. as a function of time. As Pan et al (2009) noted in their review, the errors of the DIC method can be divided into errors related to specimen, loading and imaging and to noises during image acquisition and numerical algorithm evaluation. The first group of errors includes the physical setup for image acquisition of the DIC pattern including the suboptimal speckle pattern and image distortion of the lenses. Errors relating to the correlation algorithm, the small subset size, non-appropriate correlation function, sub-pixel algorithm and low-order shape function in addition to the interpolation scheme are grouped into the second error category. In addition, the evaluation of strains depends on the strain gauge size: larger virtual strain gauges hide the local strain localizations while smaller gauges are more susceptible to the DIC errors. These errors lead to low confidence in domains of high strains and strain gradients: e.g. next to holes that are perpendicular and parallel to the surface as in the case of the challenge geometry. In addition to these metrology challenges, there are also physical challenges in the experiments, such as non-ideal boundary conditions and specimens with potential local residual strains that might influence the local deformation measures and determine crack initiation and propagation.

FEM simulations have general challenges that are connected to convergence of the nonlinear solvers within each time-step and the convergence with regard to the mesh resolution: finer meshes in elastic-plastic simulations converge to a single solution for models without damage parameters. In addition, dynamic simulations might exhibit high local velocities at the evolving crack tip which are hidden when using global energy measures to determine the applicable time-step (Hibbit et.al. 1998). More fundamentally, FEM is an approximation whose accuracy depends on the element size, number of integration points and the order of the shape functions. Stresses and strains are evaluated at these integration points and are extrapolated to the mesh nodes and there averaged to result in a unique interpolation algorithm. When using the most common tri-linear shape functions, stresses and strains exhibit an artificial jump across element boundaries. Although a refined mesh is often beneficial for most FEM challenges, an overly refined mesh might adversely affect simulation stability during crack propagation. Furthermore, as number of degrees of freedom increase, the computational expense can drastically increase.

Experiments and simulations suffer similar challenges regarding the file format of the data storage. To extract the binary data from the proprietary file formats, additional software must be written which is tailored to the challenge geometry and question. In addition to the different file-formats of the DIC and the FEM software, distributions of strains and stresses -- on the one hand -- and force-displacement curves -- on the other hand -- come from different origins, which require a manual alignment and data assembly. One common file-format for experiments and simulations would allow for numerical comparison but would hinder visual quality control.

During the evaluation phase of the challenge, we discussed the evaluation method for the percentiles of the given point and global measures. It was decided that the 20th and 80th percentile of the vertical strains and global forces were evaluated for each increasing displacement increment. This displacement increment based method was especially applicable for the SFC3 experiments which have a fixed displacement rate and for the simulations that used displacement boundary conditions. As a consequence of the displacement increment based evaluation, the relation of local strains and forces are broken (i.e. the 20th percentile strain does not necessarily correspond to the 20th percentile force). However, the display of global forces and local strains as a function of time shows the physical temporal evolution.

6.4 Defects in additively manufactured materials

Porosity (void) characterization of a longitudinal tensile and notched tensile specimen were given in Figure 4 and Figure 9, respectively, indicating porosity sizes up to 75 µm in the laser sintered components. Porosity in the fracture specimens is also evident in the *micro*-CT images in Figure 13. The fracture surfaces shown in Figure 5 and Figure 10 indicate large dimples, indicating locations of large void growth during deformation. Figure 38 provides additional images of the fracture surfaces for a longitudinal tensile and notched tensile specimen showing several small dimples. Such small dimples were reported by Gu et al. 2009 for a Cu-based powder reinforced with Ni particulates that was subject to laser sintering and it was highlighted that small dimples could be observed over 80% of the fracture surface. Also, as detailed by Gu et al. 2009, another fracture feature typical of laser sintered components are de-bonded surface particles. De-bonded spherical particles were evident in specific locations on the fracture surface of a longitudinal tensile specimen as seen in Figure 5. As seen in images of the AM specimens (Figure 5, Figure 7, and Figure 10) there is a rough surface finish. As detailed in Sames et. al. (2016), this rough surface finish is expected in AM components due to the layer-by-layer sintering method where there can be a correlation between the surface roughness and the layer thickness. Although this correlation was not specifically studied with the current specimens, the surface roughness might be expected to further contribute, but to a lesser degree than porosity or particle de-bonding, to variation in strain localization.

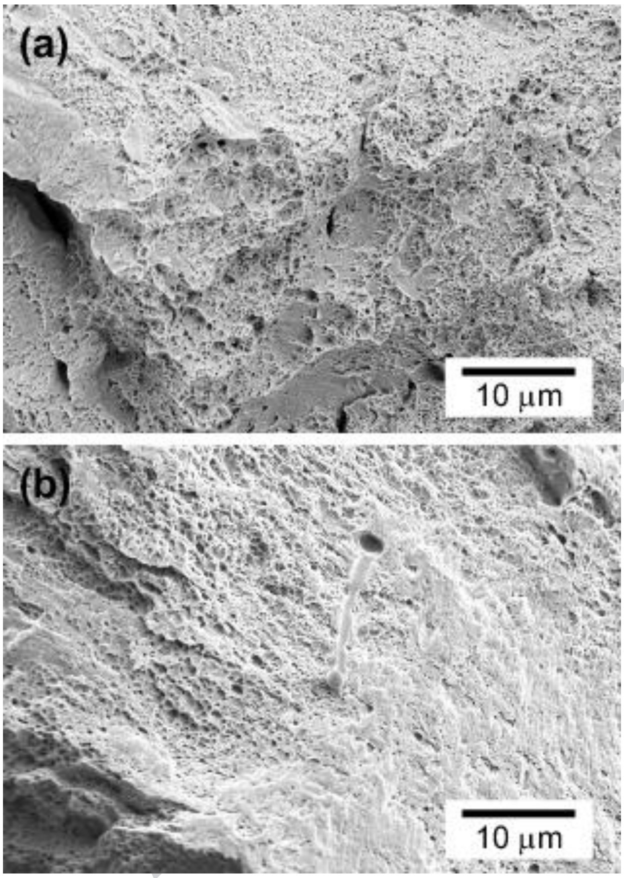

Figure 38: SEM images of fracture surface of (a) longitudinal tension (LTA04) and (b) notched tension (NA05) specimens.

As detailed by Sames et al. (2016), residual stresses resultant from the numerous heating and cooling cycles the part experiences during processing can lead to part distortion and internal cracking which can negatively affect the mechanical performance of the components. In the current work, there were no apparent internal cracks observed at which failure occurred in any of the tested geometries nor was part distortion evident in any of the samples. Rather, the crack initiated near or at the surface at the intersection of the through-hole and the angle channels of the Challenge geometry, affected by the local void structure at the intersection (Kramer et. al. 2018). For the geometries tested, the effect of residual stresses on the resultant mechanical properties may have been minimal as the strain was localized to the gauge length, notch, and stress concentrations in the tensile, notched tensile, and fracture specimens, respectively.

The stress versus strains and load versus displacement data presented in Figure 3, Figure 8, and Figure 19 indicated a larger scatter in the strain or displacement to failure than in the stress or loading response. This indicates that defects in the form of porosity, particle de-bonding, and surface roughness, were more inclined to lead to variation in the location of and evolution of strain localization as opposed to variation in the plastic deformation response of the components, particularly for the nominally uniform cross-section of the tensile specimens without geometric stress concentrators. Void metrics from the gauge region of each challenge sample studied using 3D characterizations were correlated with mechanical performance. Void metrics calculated include average void volume, maximum void volume, mean nearest neighbor distance and void volume fraction. No correlations were determined between these void metrics and the overall mechanical performance of the challenge samples. This is demonstrated with Figure 39, which presents peak load during uniaxial tension against the four different void metrics evaluated in seven challenge samples characterized, as described in Section 2.4. The results presented in Figure 39 support the conclusion that internal porosity does not dominate global mechanical performance in the challenge geometry under a uniaxial tensile load.

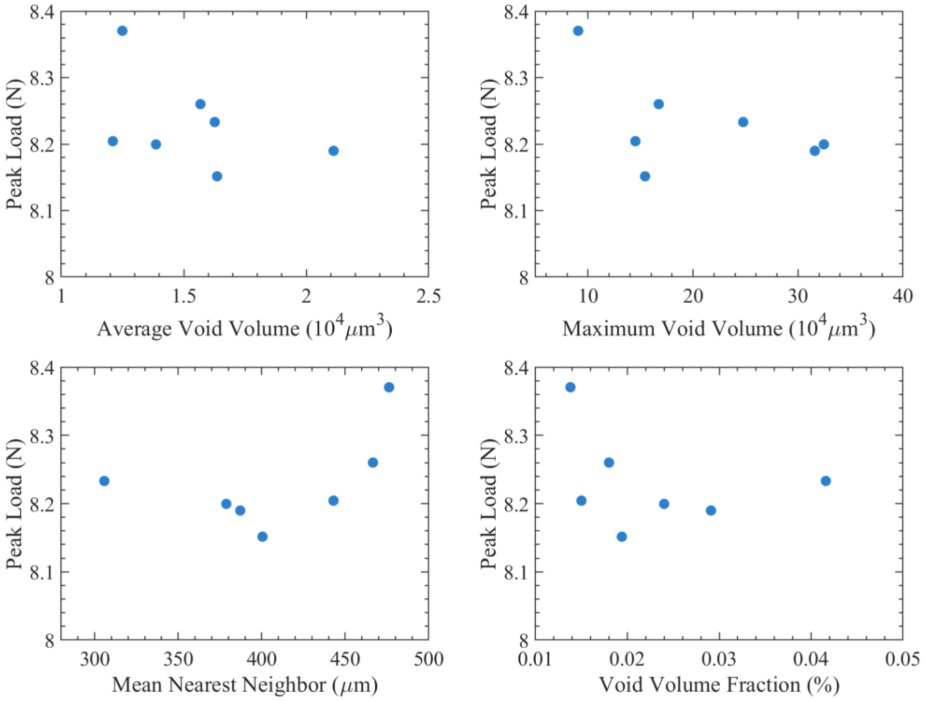

Figure 39: Peak load for the seven challenge samples studied using 3D characterizations is plotted against the average void volume (10^4 μm^3), maximum void volume (10^4 μm^3), mean nearest neighbor distance (μm), and void volume fraction (%) determined in each specimen.

6.5 Human Factors

There are many opportunities for human factors to affect the predictive capabilities of a computational model. In this study, the wealth of data supplied to the researchers for calibration along with the complexity of the material necessitated the use of relatively complex computational models with many input parameters. As the complexity of a problem increases, the chance for simple human errors to occur also increases, along with the chance that an error may not be identified. Most institutions implement quality assurance procedures for high consequence predictions. Such procedures may require group code reviews and/or full replication of the predictions by a second researcher.

Six of the teams (Teams A, C, I, L, P and S) detected errors in their original submissions and corrected their final predictions after the experimental results had been revealed. Two of the teams (Teams A and P) made errors in their simulation inputs. Team A misoriented their elastic modulus relative to the printing direction, which affected their prediction due to the anisotropic nature of the additive material. Team A also used incorrect boundary conditions on their simulated challenge specimen so that their specimen was allowed to twist during the test. In the case of Team P, the plastic hardening response in the simulated challenge specimen was misoriented relative to the printing direction.

The other teams (Teams C, I, L, and S) made errors during post-processing. Team C extracted the strain values for Question 5 from the wrong location in their model. Team I extracted the strain values for Question 5 correctly, but then likely overwrote the values during post-processing. Team S incorrectly assigned a coordinate system with respect to a path direction when extracting results. And in the case of Team L, they interpreted Question 2 differently than intended by the challenge organizer. After the submissions from all teams were compiled, the challenge organizer recognized a discrepancy in Team L’s submission. Team L supplied local forces in their submission, whereas the intent was to provide global forces. Such misinterpretations can occur in normal practice; however, appropriate measures should be in place to ensure a requesting engineer receives the correct information from the mechanician.

Some of the teams acknowledged that the SFC3 was a benchmark problem without real application consequences as compared to normal practice, and thereby reduced the thoroughness of their pre-submission review. Depending on other teams’ protocols, it is likely that other human factor errors have been propagated through the analyses at different stages and affected predictions on different scales. The effect of human factors on predictive simulation further motivates appropriate measures to verify and validate model inputs and outputs for high-consequence tasks.

6.6 Best Practices

Table 12 lists the average error between each team's mean prediction of force-versus-displacement (F-D) and the mean of the measured challenge coupon responses (challenge question 3). When a team provided revised predictions after their initial submittal (i.e., teams A, C, I, P, and S), their most recent predictions have been used. The error reported in the table is based on the average of the error percentages calculated on an interval of 0.01 mm over the displacement range of 0.0 to 1.66 mm. The error at each interval is normalized against the force of 8233 N to produce an error percentage. The 8233 N force is the maximum force attained by the mean of the measured response curves. This approach is taken so that large relative errors at low force levels are not overly emphasized in the comparison. The table also lists the average r-squared statistic between the team's prediction and the mean of the measured response. **Table 12** lists similar average errors and r-squared statistics between each team's mean prediction of vertical strain-versus-displacement (S-D) along the lines H1, H2, H3, and H4 at loads F1, F2, F3, and F4, associated with challenge question 5, and the mean of the measured challenge coupon responses for those quantities at those loads. The error reported in the table is based on the average of the error percentages calculated on a spatial interval of 0.03 mm over the widths from 0.12 to 5.88 mm for H1, H2, and H3, and over the widths from 0.12 to 1.98 and 4.02 to 6.00 for H4. The error at each interval is normalized against the maximum strain of 0.43 to produce an error percentage. The maximum strain of 0.43 is the maximum strain associated with the mean response considering all strain lines (i.e., H1, H2 H3, and H4) and all load levels (i.e., F1, F2, F3, and F4). Again, this approach is taken as it ensures that large relative errors at low strain levels are not overly emphasized in the comparison. The table also includes a combined category, which includes an average of the rankings for the F-D and S-D categories. Highlighted in the table are the top five teams in each comparison category, and for the combined category. Based on the comparison metrics, Team B and Team Q were particularly successful at predicting the response of the challenge coupon, being in the top five of each category, as well as in the top five of the combined comparison. In the subsequent sections, the specific choices of Team B and Team Q will be referenced to glean insight into what made their approach successful. It is worth emphasizing that this approach for distillation of the data, while convenient from the standpoint of reducing the large datasets involved to more manageable scalar quantities, inherently introduces bias into the comparisons. When deciding upon this approach, several alternative comparison methods were investigated, including at least one in which relative differences were normalized against localized response data. The current approach was decided upon as it most clearly illustrates the trends in the data.

Table 12 Average Error in Each Team's Force-Displacement and Strain-Displacement Predictions.

Team		Force-Displacement				Strain-Displacement				Combined	
#	Letter	Average Error	Rank	Average R-Squared	Rank	Average Error	Rank	Average R-Squared	Rank	Average Rank	Rank
1	A	6.4%	2	0.960	2	3.0%	7	0.734	12	5.75	4
2	B	7.0%	3	0.946	3	1.4%	1	0.766	2	2.25	2
3	C	20.9%	16	0.734	16	4.6%	17	0.695	15	16.00	19
4	D	17.4%	15	0.787	14	4.1%	13	0.766	1	10.75	11
5	E	12.7%	10	0.852	11	9.7%	20	0.647	18	14.75	18
6	F	15.6%	14	0.770	15	2.5%	5	0.759	4	9.50	8
7	G	14.8%	13	0.802	13	3.4%	8	0.731	13	11.75	12
8	H	8.0%	5	0.942	4	4.2%	14	0.753	7	7.50	5
9	I	8.1%	6	0.915	7	3.9%	11	0.669	17	10.25	10
10	J	13.0%	11	0.902	8	4.3%	16	0.675	16	12.75	13
11	K	7.8%	4	0.929	6	4.0%	12	0.729	14	9.00	7
12	L	36.6%	20	0.330	20	7.6%	19	0.112	21	20.00	20
13	M	8.7%	8	0.936	5	2.0%	3	0.756	5	5.25	3
14	N	26.6%	18	0.487	18	3.6%	9	0.736	11	14.00	15
15	O	30.3%	19	0.370	19	3.7%	10	0.746	9	14.25	16
16	P	23.1%	17	0.649	17	4.3%	15	0.750	8	14.25	16
17	Q	3.0%	1	0.986	1	1.8%	2	0.764	3	1.75	1
18	R	12.1%	9	0.826	12	2.3%	4	0.754	6	7.75	6
19	S	8.5%	7	0.880	9	5.6%	18	0.586	19	13.25	14
20	T	14.5%	12	0.860	10	2.6%	6	0.740	10	9.50	8
21	U	40.9%	21	0.034	21	13.4%	21	0.419	20	20.75	21

6.6.1 Implicit vs. Explicit, Quasi-Static vs. Dynamic

Just over half of the teams (52.4%) used explicit time integration to solve the transient dynamic equations of motion. The remaining teams (47.6%) used an implicit time-integration approach to solve for static force equilibrium at each time step. Only one of the teams (Team M) solved the transient dynamic equations of motion using an implicit approach. Undoubtedly, the majority of teams selected an explicit approach due to the inherent difficulties with implicit solvers and nonlinear systems that include softening and failure. Team B utilized an explicit transient dynamic approach, while Team Q utilized an implicit quasi-static approach, with approximately equivalent success, suggesting that the solution procedure was not a determining factor in a successful prediction. On average, teams that utilized an explicit approach have an F-D error of 17.4% versus 14.5% for the implicit teams, and an average S-D error of 3.7% versus 5.1%.

Due to time step limitations associated with an explicit approach, the teams that employed such an approach must have made use of mass scaling (with or without damping) and/or non-representative rates of loading. Team B in particular utilized mass scaling to increase the critical time step in their explicit simulations. As a precautionary step to ensure that the mass scaling did not affect the model response appreciably, they monitored the model kinetic energy to ensure it remained small in comparison to the internal energy.

6.6.2 Element Type, Mesh Resolution, and Symmetry

All but one team made use of either 4- or 10-node tetrahedral elements, or 8-node hexahedral elements with either reduced integration, selectively reduced integration, or full integration. Only one team (Team C) made use of a non-traditional approach, peridynamics, that does not rely on a traditional mesh or elements. Several teams made use of multiple element types in their simulations. Approximately half of the teams (45.2%) used tetrahedral elements, and the other half (50.0%) hexahedral elements. Of the teams that used tetrahedral elements, approximately half (4 teams or 19% of the total) used 4-node tetrahedral elements and the other half (5.5 teams or 26.2% of the total) used 10-node tetrahedral elements. Of the teams that used hexahedral elements, the majority (8.5 teams or 40.5% of the total) used standard reduced integration elements and just two teams (9.5% of the total) used selectively reduced integration hexahedral elements. The teams that used tetrahedral elements performed better on average with respect to the S-D error (13.3% versus 20.7% for tetrahedral and hexahedral teams, respectively) and about the same with respect to the S-D error (5.0% for both categories). However, the top performing teams (Team B and Team Q) both made use of hexahedral elements, with Team B using reduced integration hexahedral elements and Team Q using selectively reduced hexahedral elements in which the deviatoric portion of the element's response is based on a full integration scheme and the volumetric response is based on a reduced integration scheme. Overall, the element type was not a critical factor for prediction success, but the hexahedral elements were used by the top performing teams.

The average element size employed in the gauge section of the challenge coupon was approximately 0.145 mm, ranging from as large as approximately 0.3 mm to as small as 0.038 mm. Both Team B and Team Q employed elements smaller than the average element size at 0.065 mm and 0.0415 mm, respectively. Figure 40 illustrates the correlation between average element size and model error. Reduced element size does seem to correlate with reduced error, although smaller element sizes, by themselves, do not guarantee improved model prediction. The average number of degrees of freedom (DOFs) for all teams (with DOFs for each team all converted to a full model representation when symmetry was employed) is 1.752 million. It is worth noting that Team Q reported the second highest DOFs at 20.242 million and produced approximately as accurate a prediction as Team B whose model included only 1.841 million DOFs. Additionally, Team Q used selectively reduced 8-node hexahedral elements; whereas Team B used standard reduced integration hexahedral elements, meaning Team Q paid an additional 8x computational penalty factor, per element, per material point solve, that Team B did not. The exact difference in computational cost is difficult to compare, however, as Team B used an explicit solution strategy and Team Q used an implicit solution strategy.

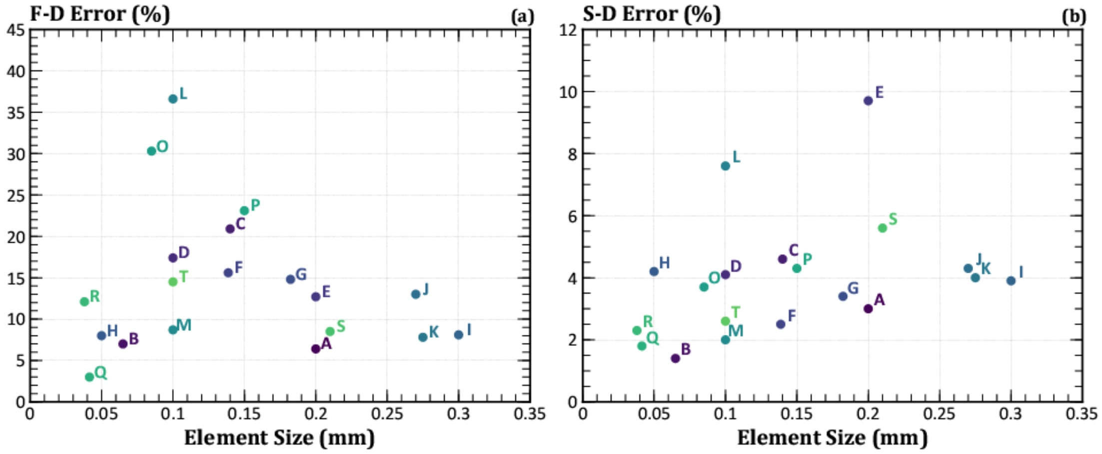

Figure 40: Average Element Size in the Challenge Coupon Gauge Section Versus Model Prediction Error: (a) Force versus displacement error and (b) strain versus displacement error.

The majority of the teams (66.7%) did not employ symmetry in their model, with the remainder of the teams employing quarter-symmetry. One team (Team N) specified that symmetry was employed but did not specify the type of symmetry. Team B used a quarter-symmetric model. Team Q did not employ symmetry. Comparison of the average F-D and S-D errors for teams employing symmetry (average F-D error of 17.2% and S-D error of 4.0%) with those that did not (average F-D error of 17.3% and S-D error of 4.8%), indicates little difference between the two groups. The primary reason there was little difference between models that assumed symmetry and models that did not is that the failure that was experimentally generated was nominally symmetric, apart from the details of the failure interacting with the AM voids. If the actual failure had ended up not being nominally symmetric, then models that assumed symmetry would have likely exhibited much larger errors.”

6.6.3 Boundary Conditions

Nearly two-thirds of the teams applied nodal displacement and/or velocity boundary conditions to the nodes in their model that would be in direct contact with the grip pads, or to all the nodes on the contact faces of the grip sections of the coupon. In all instances, these boundary conditions acted to constrain translations and rotations. A few teams decided to apply nodal boundary conditions at planar cross-sections either at each end of the gauge section of the coupon, or at the mid-height of each grip section, therefore eliminating some or all of the grip portions of the coupon from their models. In general, the boundary conditions applied by each team are the same in most respects, and there appear to be no significant advantages to any of the approaches taken.

6.6.4 Yield, Hardening, and Rate and Temperature Effects

Nearly two-thirds (61.9%) of the teams employed an isotropic, J_2 (second invariant of the deviatoric stress tensor) based, yield condition, whereas the remainder of the teams (38.1%) used an anisotropic yield condition, most prevalently based on the Hill yield surface. While the average F-D (15.8% for isotropic versus 16.4% for anisotropic) and S-D (4.7% for the isotropic and 3.8% for the anisotropic) errors do not indicate a clear difference between the two groups, both Team B and Team Q made use of anisotropic yield surfaces. That being said, teams A and H are both in the top 5 when their combined rankings in Table 12 are considered, and both used an isotropic yield surface. This would tend to indicate that while the material is clearly anisotropic in its response, successfully predicting the response of the coupon with respect to the quantities requested does not require that an anisotropic material model be used. That being said, other comparison metrics not considered in the SFC3 may have shown the importance of an anisotropic material model.

Approximately two-thirds (61.9%) of the teams used a tabulated hardening behavior for the material. The remainder of the teams (38.1%) fit specific functional relationships to the provided data to define the hardening behavior. Half of these teams (4 or 19.0% of the total) assumed power-law hardening, whereas the other half of these teams (also 4 or 19.0% of the total) assumed some other form of hardening. Two of the top five teams (with respect to combined average ranking in Table 12) fall in this final category, specifically teams B and Q which assumed a combined Swift/Voce law and a combined Frost-Ashby power-law, respectively. Teams that assumed some exotic hardening law had the lowest F-D and S-D error percentages at 7.6% and 2.8%. These percentages are comparatively 17.1% and 4.8%, and 20.9% and 4.6%, for the tabular hardening and power-law hardening teams, respectively.

Only Team M performed coupled thermal-mechanical simulations. While Team M was in the top 5 when combined performance is considered, the sample size is too small to determine if this was really a determining factor in that team's success. Given the relatively low loading rates, it is likely that heating of the material due to plastic deformation did not play a significant role in the response. In fact, the balance of the teams in the top 5 of the combined results (teams A, B, H, and Q) did not include thermal effects in their models. More than half of the teams (57.1%) did not explicitly include loading rate effects in their models. Some teams argued that loading rates were implicitly included through their calibration effort, as the loading rates for the material test data coupons were similar to those used with the challenge coupon. Approximately 38.1% of the teams explicitly including loading rate effects in the material models they used. Teams that explicitly included loading rate effects had, on average, a lower F-D error (14.1% versus 17.6%) and a lower S-D error (3.2% versus 4.7%). The top three teams with respect to combined ranking (B, M, and Q) all explicitly including loading rate in their simulations. The 0.0127 mm/s challenge coupon loading rate is relatively low, suggesting that loading rate effects might be negligible; however, based on the above comparison this may not necessarily be the case. In general, stainless steels are considerably rate-dependent, even at low strain rates. Also, it is not the loading rate that matters as much as the local strain rates, which are necessarily higher during localization events.

6.6.5 Damage Accumulation, Failure Initiation, Strength Decay, Crack Surface Formation

Just under three-quarter of the teams (71.4%) used some form of stress state informed, strain-based damage accumulation and failure initiation criterion. Three teams (14.3%) accumulated damage and initiated failure using a pure strain criterion (maximum principal or equivalent plastic), two teams (9.5%) initiated failure using a pure stress criterion (maximum principal stress), and one team (4.8%) used a stress criterion that was based on a combination of maximum principal stress and hydrostatic stress. All but one team in the top five of the combined average ranking used a stress state informed, strain-based damage accumulation and failure initiation criteria, including Team Q that used a strain-based criterion with dependence on all three (I1, J2, and J3) stress invariants. Team B uses a stress-state dependent Hosford-Coulomb model. Due to the limited dataset of fracture geometries provided and because of the team's experience, the criterion was reduced to a maximum equivalent plastic strain criterion in this case.

Just over one-third of the teams (38.1%) made use of a material constitutive model that continuously evolves the material response based on some measure of accumulated damage. The remaining teams (61.9%) used failure models that only decayed the material strength once a failure threshold had been achieved. The failure threshold teams performed slightly better, with their average F-D and S-D errors being 14.4% and 4.0%, respectively, in comparison to the continuous evolution teams with average F-D and S-D errors of 18.6% and 5.0%, respectively. However, it is worth noting that two of the top five teams (A and Q) are included in the continuous evolution group.

Most of the teams (61.9%) used element deletion following strength decay to represent the formation of fracture surfaces. Three teams (14.3%) used XFEM, one team (4.8%) used adaptive remeshing, one team used peridynamics, and three teams (14.3%) did not include any means by which to explicitly represent the formation of fracture surfaces in their mesh (although they did rely on stress decay and damage to capture the loss of strength associated with the formation of fracture surfaces). All five top performing teams used element deletion, with Team B deleting elements immediately upon their reaching the failure initiation criterion without first decaying their strength.

6.6.6 Test Data Utilization and Model Calibration

Nearly all of the teams made use of the 0.05 mm/s loading rate longitudinal coupon A tensile test data, with five teams (23.8%) ignoring the AM finish coupon data in favor of the electrical discharge machined (EDM) coupon data. Fourteen teams (66.7%) made use of the AM longitudinal coupon test data without consideration of the EDM longitudinal test data. Two teams (9.5%) considered both in their calibration. Teams that considered the EDM coupon A longitudinal test data performed, on average, better than the teams that did not, with average F-D and S-D errors of 14.5% and 3.3% respectively, versus 15.4% and 4.8%, respectively. Both teams B and Q considered the EDM data, whereas teams A and M (also top 5 performers) did not. Approximately half of the teams (47.6%) considered the transverse coupon A test data (with EDM finish) and those teams, on average, performed better with respect to the S-D error (3.7% versus 5.0%) but worse with respect to F-D error (16.8% versus 15.3%). Five teams (23.8%) made use of the slow loading rate (0.0005 mm/s) longitudinal coupon A with EDM finish test data. The teams that made use of that data have approximately the same F-D error (16.2% versus 15.9%) and lower average S-D error (3.1% versus 4.8%). Nearly all of the teams (85.7%) made use of the notched tensile test data (coupon B, longitudinal, 0.15 mm/s, AM finish). These teams also had lower average F-D and S-D errors (15.4% versus 19.8%, and 4.1% versus 6.2%, respectively).

One team (team L) made use of the DIC data which they used to determine r-values for the Hill yield surface definition, and a second team (team B) used the DIC data to determine two Lankford ratios for the flow potential of the non-associated yield surface. Only two teams (D and Q) made use of the dimensional data (challenge coupon gross dimensions and CT-scan tomography data related to internal geometric feature dimensional variability) to explicitly include geometric variability in their meshes. Only one team (team R) made use of the micrographs of the sectioned LTA21, NA24, and A06 coupons to inform their model with respect to void size and spatial distribution. Team R used this data to explicitly include representations of voids within their meshed geometries. In general, none of the teams used the dimensional data for the A coupons, the deformed shape of the A and B type coupons following testing, the scanning electron microscope (SEM) data provided of the LTA04 and NA05 fracture surfaces, or the electron backscatter diffraction (ESBD) data for the A06 challenge coupon. Nearly two-thirds (61.9%) used some sort of data from external sources (described in the Team Summaries Appendix 1).

6.6.7 Summary

Based on an evaluation of the performance of the teams described above the following observations may be made. Implicit and explicit methods, either quasi-static or dynamic, were each capable of producing accurate predictions. Both hexahedral and tetrahedral element types produced accurate predictions (although all but one of the top performing teams used hexahedral elements). Use of symmetry was a valid approach for this problem. Element size does not correlate with accuracy of prediction for this geometry. Boundary conditions were generally represented in a consistent fashion across all teams, with no indication that the selection of boundary condition detrimentally affected any team's prediction (with one exception possibly being Team A vs. Team A Revised). Representation of anisotropy did not seem to be overly critical in predicting the QOI's for this problem, although there are some indications that the teams that considered the transverse test data in addition to the longitudinal test data made better strain predictions. Inclusion of temperature affects appears not to be overly important for this challenge, whereas including loading rate affects was of moderate importance, with teams that included loading rate effects doing somewhat better. Element deletion was the most popular approach for representation of the formation of fracture surfaces and was adequate for this problem. Strain-based failure initiation criteria were the most prevalent, including stress-state informed strain-based criteria. The specific approach taken to decay the strength of the material once the failure initiation criteria had been met was not important for this problem. Nearly all teams incorporated material and geometric variability implicitly (indirectly) by capturing the variability in response in material model input parameters determined through the calibration process with the provided material test data. Only three teams explicitly considered coupon geometric variability and/or material defect inclusions and variability. Two of the teams that considered geometric variability noted that the geometric variability was likely the largest contributor to the variability observed in the test data. Based on the results, correctly accounting for surface geometric variability appears to be important, as indicated by the improved performance of the teams that recognized and captured the importance of the differences between the AM and EDM coupon A tensile test data. DIC, pre-test dimensional, longitudinal mid-plane cross-section micrograph, post-test fracture plane cross-section deformation, fracture surface SEM, challenge coupon micro-CT, and challenge coupon longitudinal mid-plane cross-section ESBD data were largely unused.

7 Summary and Future Work

The third Sandia Fracture Challenge evaluated blind predictions from 21 teams from 16 institutions of ductile failure in an additively manufactured 316L stainless steel structure. These predictions included global and local measures of deformation, the latter of which were compared to DIC surface strains. In addition to nominal predictions, the teams were given the option to provide specific uncertainty bounds on their predictions. In this third installment of the Sandia Fracture Challenge, there was one observed failure path, unlike the prior two Challenges where two failure modes were observed. All teams predicted the same, correct path, while in prior Challenges, the teams predicted either of the two observed paths. The global behavior of the SFC3 geometry specimens had modest variability despite being made of AM metal; this surprising experimental result was attributed to the large stress concentrations overwhelming the stochastic local influence of the AM voids and surface roughness that often plagues structures with more uniform cross sections. In general, the predictions of nominal global behavior were reasonable as compared to the experiments, but the predicted 20th and 80th percentile uncertainty bounds varied widely amongst the 12 teams that provided them. The local surface strains differed considerably between different specimens leading to large uncertainty bounds, particularly at larger global deformations. The teams tended to over-predict the nominal local strains early in the deformation and then under-predict later in the deformation; also, the bounds had a smaller range compared to that of the experiments.

The overall better nominal predictions of global behavior and correct identification of the crack path as compared to the previous two Challenges is encouraging. Notably, two teams (B and Q) predicted nominal global load versus displacement behavior within the experimental bounds using different numerical and modeling approaches. The common features of these two predictions included sophisticated plasticity and failure models, anisotropy and/or strain-rate dependence, and small element sizes. Though a variety of numerical and modeling choices all led to decent predictions overall, one best practice was identified to help in this problem: consideration of geometric variability, particularly in the calibrations of constitutive models, but also in the SFC3 geometry simulations. The sensitivity to specimen geometry (due to out-of-tolerance dimensions (Boyce *et. al.* 2014) or a warped plate (Boyce *et. al.* 2016)) led to bifurcations of the crack paths in the prior two Challenge, so the importance of specimen geometry variation is a common theme across all three Challenges. Unlike previous Challenges, SFC3 did not show much sensitivity to loading conditions, calibration data in non-tensile deformation modes, or temperature. Human errors were prevalent in all three Challenges, highlighting the importance of peer review to prevent seemingly minor mistakes with large consequences.

An extensive set of data was provided, including microstructural data from EBSD and micro-CT, but much of this data was left unused, likely due the complexity of the data in combination with a limited time for the prediction. We simply do not know if these data would have improved the predictions, but it is likely that some of the details of the voids and surface roughness would have contributed to better predictions of local strains. One way to identify the importance of including these details would be to perform experiments and simulations that look at a similar geometry to the SFC3 geometry in both AM and wrought metal. Specifically, a geometry with the through hole and angled channels, where the SFC3 specimens failed, could be fabricated in both AM and wrought 316L stainless steel. Calibration experiments would need to run for both materials with the same geometries to allow for comparison of the simulations of the two types of materials. Some simulations of the AM structure would consider the AM voids and surface roughness to compare to nominal geometry simulations. Then these could be compared to simulations of the wrought material where large voids are not present. These experiments and simulations together would highlight what microstructural information improved the simulations of the AM material compared to the control case of the same structure in a wrought material. The experiments also would show how the structure itself was affected by the AM voids. This potential study could provide additional best practices for simulating ductile failure AM structures as compared to ductile failure in structures made from traditional materials.

The success of the three Sandia Fracture Challenges has laid the foundation for the establishment of the Structural Reliability Partnership (SRP), initiated by Sandia National Laboratories, Exxon Mobil, and the University of Texas at Austin. The purpose of the SRP is to facilitate coordinated experimental and computational research in the area of structural reliability. The SRP members will organize staggered blind assessment Challenges on different structural reliability topics, using shared focus materials that facilitate cross-institution comparison, sharing of best practices, and leveraging of cross-institutional R&D investments to address shortcomings and gaps in structural reliability experiments and predictions. Documentation of these SRP Challenges will broadly disseminate the research to the mechanics community. Details of the SRP are available at https://share-ng.sandia.gov/srp/

Acknowledgements

ADS gratefully acknowledges support from the Air Force Office of Scientific Research Young Investigator Program, under Agreement No.FA9550-15-1-0172. Southwest Research Institute acknowledges support from internal research and development grant 18.R8747. BLB would like to thank James Redmond and H. Eliot Fang for managing Sandia's role in this work through the DOE Advanced Scientific Computing program. SLBK would like to thank Dennis Croessmann, Scott Peterson, and Darrick Jones for their management role supporting the experimental efforts at Sandia for this work through the NNSA Delivery Environments program. Microscopy facilities used in this study are provided by the Center for Integrated Nanotechnologies at Sandia National Laboratories. SLBK would like to thank Alice Kilgo, Joseph Michael, Bonnie McKenzie, Jhana Gearhart, David Johnson, Darren Pendley, Carl Jacques, Andrew Lenfter and Todd Huber for their help in characterization of the SFC3 materials. SLBK and BLB would like to thank Ben Blaiszik with the Materials Data Facility with support publishing of the SFC3 Challenge data. Sandia National Laboratories is a multimission laboratory managed and operated by National Technology & Engineering Solutions of Sandia, LLC, a wholly owned subsidiary of Honeywell International Inc., for the U.S. Department of Energy's National Nuclear Security Administration under contract DE-NA0003525. The views expressed in the article do not necessarily represent the views of the U.S. Department of Energy or the United States Government.

References

B. M. Adams, L. E. Bauman, W. J. Bohnhoff, K. R. Dalbey, M. S. Ebeida, J. P. Eddy, M. S. Eldred, P. D. Hough, K. T. Hu, J. D. Jakeman, J. A. Stephens, L. P. Swiler, D. M. Vigil, and T. M. Wildey. Dakota, A Multilevel Parallel Object-Oriented Framework for Design Optimization, Parameter Estimation, Uncertainty Quantification, and Sensitivity Analysis: Version 6.3 User's Manual. SAND Report SAND2014-4633, Sandia National Laboratories, Albuquerque, NM and Livermore, CA, 2015.

M. Agarwala, D. Bourell, J. Beaman, H. Marcus, and J. Barlow, "Direct selective laser sintering of metals," *Rapid Prototyping Journal,* vol. 1, pp. 26-36, 1995.

D. J. Bammann and E. C. Aifantis, “A model for finite-deformation plasticity,” *Acta Mech.*, vol. 69, no. 1–4, pp. 97–117, Dec. 1987.

F. Bechmann, "Changing the future of additive manufacturing," *Metal Powder Report,* vol. 69, pp. 37-40, 2014.

A. M. Beese and B. E. Carroll, "Review of mechanical properties of Ti-6Al-4V made by laser-based additive manufacturing using powder feedstock," *Jom,* vol. 68, pp. 724-734, 2016.

Behzadinasab, M., & Foster, J. (2018). The third Sandia Fracture Challenge: peridynamics blind prediction of dynamic ductile fracture characterization in additively manufactured metal. Int J Fract.

Behzadinasab, M., & Foster, J. (In preparation). On the stability of the generalized, ordinary, finite deformation constitutive correspondence model of peridynamics.

V. Bhavar, P. Kattire, V. Patil, S. Khot, K. Gujar, and R. Singh, "A review on powder bed fusion technology of metal additive manufacturing," in *4th International Conference and Exhibition on Additive Manufacturing Technologies-AM-2014, September*, 2014, pp. 1-2.

B. Blaiszik, K. Chard, J. Pruyne, R. Ananthakrishnan, S. Tuecke, and I. Foster. "The Materials Data Facility: Data services to advance materials science research." JOM 68, no. 8 (2016): 2045-2052.

B. L. Boyce, S. L. Kramer, H. E. Fang, T. E. Cordova, M. K. Neilsen, K. Dion, *et al.*, "The Sandia Fracture Challenge: blind round robin predictions of ductile tearing," *International Journal of Fracture,* vol. 186, pp. 5-68, 2014.

B. Boyce, S. Kramer, T. Bosiljevac, E. Corona, J. Moore, K. Elkhodary, *et al.*, "The second Sandia Fracture Challenge: predictions of ductile failure under quasi-static and moderate-rate dynamic loading," *International Journal of Fracture,* vol. 198, pp. 5-100, 2016.

D. Brackett, I. Ashcroft, and R. Hague, "Topology optimization for additive manufacturing," in *Proceedings of the solid freeform fabrication symposium, Austin, TX*, 2011, pp. 348-362.

S. Bremen, W. Meiners, and A. Diatlov, "Selective laser melting," *Laser Technik Journal,* vol. 9, pp. 33-38, 2012.

S. Brinckmann, L. Quinkert, *Ductile tearing: applicability of a modular approach using cohesive zones and damage mechanics*, International Journal of Fracture 186, pp. 5-68, 2014.

D. Broek, *The practical use of fracture mechanics*: Springer Science & Business Media, 2012.

A.A. Brown and D.J. Bammann. Validation of a model for static and dynamic recrystallization in metals. International Journal of Plasticity, 32-33:17–35, 2012.

J. Chambert, P. Bressolette, and A. Vergne, “Implementation of coalescence criteria into the GTN model application to work-hardening ductile materials,” *ECF13*, 2013.

T. Chu, W. Ranson, and M. A. Sutton, "Applications of digital-image-correlation techniques to experimental mechanics," *Experimental mechanics,* vol. 25, pp. 232-244, 1985.

B. V. Cockeram and K. S. Chan, "In situ studies and modeling of the deformation and fracture mechanism for wrought Zircaloy-2 and Zircaloy-4 as a function of stress state," *Journal of Nuclear Materials,* vol. 434, pp. 97-123, 2013.

A. Cocks and M. Ashby. Intergranular fracture during powerlaw creep under multiaxial stresses. Metal Science, 14(8– 9):395–402, August 1980.

L. Cortese, T. Coppola, F. Campanelli, F. Campana en M. Sasso, „Prediction of ductile failure in materials for onshore and offshore pipeline applications," *International Journal of Damage Mechanics,* vol. 23, nr. 1, pp. 104-1235, 2013.

C. R. Deckard, J. J. Beaman, and J. F. Darrah, "Method for selective laser sintering with layerwise cross-scanning," ed: Google Patents, 1992.

K. Dion, and M.K. Neilsen, "Coupled thermal stress simulations of ductile tearing," *International Journal of Fracture*, vol. 198, pp. 167-178, March 2016.

J. M. Emery, R. V. Field, J. W. Foulk, K. N. Karlson, and M. D. Grigoriu, "Predicting laser weld reliability with stochastic reduced-order models: PREDICTING LASER WELD RELIABILITY," *Int. J. Numer. Methods Eng.*, vol. 103, no. 12, pp. 914–936, Sep. 2015.

Ergodan, F. and G.C. Sih. "On Extension in Plates Under Plane Loading and Transverse Shear." Journal of Basic Engineering, Transactions of ASME 85 (1963): 5 19-27.

Erice, B., Roth, C.C., Mohr, D., 2018, Stress-state and strain-rate dependent ductile fracture of dual and complex phase steel, Mechanics of Materials, 116, pp. 11-32.

R. Fletcher, P*ractical methods of optimization* (2nd ed.), New York: John Wiley & Sons, ISBN 978-0-471-91547-8, 1987.

Foster, J., & Xu, X. (2018). A generalized, ordinary, finite deformation constitutive correspondence model for peridynamics. *Int J Solids Struct*, 141:245–253.

M. Foust, D. Thomsen, R. Stickles, C. Cooper, and W. Dodds, "Development of the GE aviation low emissions TAPS combustor for next generation aircraft engines," in *50th AIAA Aerospace Sciences Meeting including the New Horizons Forum and Aerospace Exposition*, 2012, p. 936.

W. E. Frazier, "Metal additive manufacturing: a review," *Journal of Materials Engineering and Performance,* vol. 23, pp. 1917-1928, 2014.

H.J. Frost and M.F. Ashby. Deformation-mechanism maps: The plasticity and creep of metals and ceramics. Pergamon Press, New York, 1982.

H. Gong, K. Rafi, H. Gu, T. Starr, and B. Stucker, "Analysis of defect generation in Ti–6Al–4V parts made using powder bed fusion additive manufacturing processes," *Additive Manufacturing,* vol. 1, pp. 87-98, 2014.

Gorji, M.B., Manopulo, N., Hora, P., Barlat, F., 2016. Numerical investigation of the post-necking behavior of aluminum sheets in the presence of geometrical and material inhomogeneities. Int. J. Solids Struct. 102–103, 56–65.

Gorji, M.B., Tancogne-Dejean, T., Mohr, D., 2018. Heterogeneous random medium plasticity and fracture model of additively-manufactured Ti-6Al-4V. Acta Mater. 148, 442-455.

D. Gu, Y. Shen, and Z. Lu, "Microstructural characteristics and formation mechanism of direct laser-sintered Cu-based alloys reinforced with Ni particles", Materials and Design, Vol. 30, pp. 2099-2107, 2009.

D. Gu, Y.-C. Hagedorn, W. Meiners, G. Meng, R. J. S. Batista, K. Wissenbach*, et al.*, "Densification behavior, microstructure evolution, and wear performance of selective laser melting processed commercially pure titanium," *Acta Materialia,* vol. 60, pp. 3849-3860, 2012.

Gurson, A. (1977). "Continuum Theory of Ductile Rupture by Void Nucleation and Growth: Part I—Yield Criteria and Flow Rules for Porous Ductile Media." ASME. J. Eng. Mater. Technol.: 99(91):92-15.

T. A. Hemphill, "POLICY DEBATE: The US advanced manufacturing initiative: Will it be implemented as an innovation–or industrial–policy?," *Innovation,* vol. 16, pp. 67-70, 2014.

E. D. Herderick, "Accelerating the Additive Revolution," *JOM,* vol. 69, pp. 437-438, 2017.

D. Hibbitt, B. Karlsson, and P. Sorensen. ABAQUS/Standard: User's Manual, volume 1. Hibbitt, Karlsson & Sorensen, 1998.

R. Hill, "A theory of the yielding and plastic flow of anisotropic metals," *Proceedings of the Royal Society of London,* vol. 193, pp. 281-297, 1948.

W. Hofmeister and M. Griffith, "Solidification in direct metal deposition by LENS processing," *Jom,* vol. 53, pp. 30-34, 2001.

Mark F. Horstemeyer and Arun M. Gokhale. A void-crack nucleation model for ductile metals. Internation Journal of Solids and Structures, 36(33):5029–5055, November 1999.

S. H. Huang, P. Liu, A. Mokasdar, and L. Hou, "Additive manufacturing and its societal impact: a literature review," *The International Journal of Advanced Manufacturing Technology,* vol. 67, pp. 1191-1203, 2013.

Y. Huang, "Accurate dilatation rates for spherical voids in triaxial stress fields," *Journal of Applied Mechanics,* vol. 58, pp. 1084-1086, 1991.

C. W. Hull, "Apparatus for production of three-dimensional objects by stereolithography," ed: Google Patents, 1986.

Ingraffea, A. R. (2004). Computational fracture mechanics. John Wiley & Sons, Ltd.

Jackiewicz J (2011) Use of a modified Gurson model approach for the simulation of ductile fracture by growth and coalescence of microvoids under low, medium and high stress triaxiality loadings. Eng Fract Mech 78:487–502.

Jackiewicz J (2016) Recent trends in the development of Gurson's model. In: Recent Trends in Fracture and Damage Mechanics; Hütter G, Zybell L (ed.). Springer International Publishing, Cham, pp. 417-442.

B. H. Jared, M. A. Aguilo, L. L. Beghini, B. L. Boyce, B. W. Clark, A. Cook, *et al.*, "Additive manufacturing: Toward holistic design," *Scripta Materialia,* vol. 135, pp. 141-147, 2017.

Johnson, G., & Cook, W. (1985). Fracture characteristics of three metals subjected to various strains, strain rates, temperatures and pressures. *Engrg Fract Mech, 21*(1), 31-48.

Kale A B, Bag A, Hwang J-H, Castle E G, Reece M J, Choi S-H (2017) The deformation and fracture behaviors of 316L stainless steels fabricated by spark plasma sintering technique under uniaxial tension. Materials Science & Engineering A 707: 362–372.

M. Khaing, J. Fuh, and L. Lu, "Direct metal laser sintering for rapid tooling: processing and characterisation of EOS parts," *Journal of Materials Processing Technology,* vol. 113, pp. 269-272, 2001.

G. Kharmanda, N. Olhoff, A. Mohamed, and M. Lemaire, "Reliability-based topology optimization," *Structural and Multidisciplinary Optimization,* vol. 26, pp. 295-307, 2004.

W. King, A. Anderson, R. Ferencz, N. Hodge, C. Kamath, S. Khairallah, *et al.*, "Laser powder bed fusion additive manufacturing of metals; physics, computational, and materials challenges," *Applied Physics Reviews,* vol. 2, p. 041304, 2015.

S. Kramer, B. Boyce, A. Jones, J. Gearhart, B. Salzbrenner, "The Third Sandia Fracture Challenge," 2018, http://dx.doi.org/doi:10.18126/M26D20.

S. Kramer, T. Ivanoff, A. Lentfer, and J. Madison. "Void and Fracture Evolution in the Third Sandia Fracture Challenge Specimens." *Int. J. Fract.* Special SFC3 volume, 2018.

Lan, W., Deng, X., & Sutton, M. A. (2007). Three-dimensional finite element simulations of mixed-mode stable tearing crack growth experiments. Engineering Fracture Mechanics, 74(16), 2498-2517.

C. Landron, E. Maire, O. Bouaziz, J. Adrien, L. Lecarme and A. Bareggi, "Validation of void growth models using X-ray microtomography characterization of damage in dual phase steels," *Acta Materialia,* vol. 59, pp. 7564-7573, 2011.

L. Lecarme, E. Maire, K. Kumar, C. De Vleeschouwer, L. Jacques, A. Simar and T. Pardoen, "Heterogenous void growth revealed by in situ 3-D X-ray microtomography using automatic cavity tracking," *Acta Materialia*, vol. 63, pp. 130-139, 2014.

M. J. Matthews, G. Guss, S. A. Khairallah, A. M. Rubenchik, P. J. Depond, and W. E. King, "Denudation of metal powder layers in laser powder bed fusion processes," *Acta Materialia*, vol. 114, pp. 33-42, 2016.

F. A. McClintock and G. Irwin, "Plasticity aspects of fracture mechanics," in *Fracture toughness testing and its applications*, ed: ASTM International, 1965.

D. McDowell and F. Dunne, "Microstructure-sensitive computational modeling of fatigue crack formation," *International journal of fatigue,* vol. 32, pp. 1521-1542, 2010.

W. Meiners, K. Wissenbach, and A. Gasser, "Shaped body especially prototype or replacement part production," *DE Patent*, vol. 19, 1998.

W. J. Milles, "Fracture toughness of type 304 and 316 stainless steels and their welds," *International Materials Reviews,* vol. 42, pp. 45-82, 1997.

Moës, N., Dolbow, J., & Belytschko, T. (1999). A finite element method for crack growth without remeshing. International journal for numerical methods in engineering, 46(1), 131-150.

Mohr, D., Dunand, M., Kim, K.H., 2010. Evaluation of associated and non-associated quadratic plasticity models for advanced high strength steel sheets under multi-axial loading. Int. J. Plast. 26, 939–956.

Mohr, D., Marcadet, S.J., 2015. Micromechanically-motivated phenomenological Hosford–Coulomb model for predicting ductile fracture initiation at low stress triaxialities. Int. J. Solids Struct. 67–68, 40–55.

L. E. Murr, S. M. Gaytan, D. A. Ramirez, E. Martinez, J. Hernandez, K. N. Amato, *et al.*, "Metal fabrication by additive manufacturing using laser and electron beam melting technologies," *Journal of Materials Science & Technology*, vol. 28, pp. 1-14, 2012.

K. Nahshon and J. W. Hutchinson. Modification of the Gurson model for shear failure. European Journal of Mechanics -A/Solids, 27(1):1–17, February 2008.

J.A. Nelder, and R. Mead, *A simplex method for function minimization*, The Computer Journal, 7, pp. 308-313, 1965.

Hans Nordberg. Note on the sensitivity of stainless steels to strain rate. Research Report 04.0-1, AvestaPolarit Research Foundation and Sheffield Hallam University, 2004.

W. L. Oberkampf and C. J. Roy, Verificaton and validation in scientific computing, New York: Cambridge University Press, 2010.

Parks, M., Littlewood, D., Mitchell, J., & Silling, S. (2012). *Peridigm users' guide.* Techincal Report SAND2012-7800, Sandia National Laboratories.

H. Rafi, N. Karthik, H. Gong, T. L. Starr, and B. E. Stucker, "Microstructures and mechanical properties of Ti6Al4V parts fabricated by selective laser melting and electron beam melting," *Journal of materials engineering and performance,* vol. 22, pp. 3872-3883, 2013.

J. R. Rice and D. M. Tracey, "On the ductile enlargement of voids in triaxial stress fields," *Journal of the Mechanics and Physics of Solids,* vol. 17, pp. 201-217, 1969.

Roth, C.C., Mohr, D., 2014. Effect of strain rate on ductile fracture initiation in advanced high strength steel sheets: Experiments and modeling. Int. J. Plast. 56, 19–44.

Reu, P.L., "Hidden Components of 3D-DIC: Triangulation and Post-processing—Part 3." Experimental Techniques*, 39, pp. 3-5, 2012.*

Saad Y (2003) Iterative Methods for Sparse Linear Systems, 2nd edition, Society for Industrial and Applied Mathematics.

B. C. Salzbrenner, J. M. Rodelas, J. D. Madison, B. H. Jared, L. P. Swiler, Y.-L. Shen, *et al.*, "High-throughput stochastic tensile performance of additively manufactured stainless steel," *Journal of Materials Processing Technology,* vol. 241, pp. 1-12, 2017.

W.J. Sames, F.A. List, S. Pannala, R.R. Dehoff, and S.S. Babu, "The metallurgy and processing science of metal additive manufacturing", International Materials Reviews, Vol. 61, pp. 1-46, 2016.

L. E. Schwer, "An overview of the ASME V&V-10 guide for verification and validation in computational solid mechanics," in 20th International Conference on Structural Mechanics in Reactor Technology, Espoo, Finland, 2009.

F. Šebek, P. Kubík, J. Hůlka, and J. Petruška, "Strain hardening exponent role in phenomenological ductile fracture criteria," *European Journal of Mechanics - A/Solids*, vol. 57, pp. 149–164, May 2016.

M. Seifi, A. Salem, J. Beuth, O. Harrysson, and J. J. Lewandowski, "Overview of materials qualification needs for metal additive manufacturing," *Jom,* vol. 68, pp. 747-764, 2016.

Sierra Solid Mechanics Team, "Sierra/Solid Mechanics 4.40 User's Guide," SAND2016-2707, Sandia National Laboratories, Albuquerque, NM, March 2016.

Silling, S. (2000). Reformulation of elasticity theory for discontinuities and long-range forces. J Mech Phys Solids, 48(1), 175-209.

Silling, S., Epton, M., Weckner, O., Xu, J., & Askari, E. (2007). Peridynamic states and constitutive modeling. J Elasticity, 88(2), 151-184.

Simha CHM and Williams BW, "Modeling failure of Ti-6Al-4V using damage mechanics incorporating effects of anisotropy, rate, and temperature on strength", Int J Fract, Vol. 198, pp. 101-115, 2016.

Simo, J. (1988). A framework for finite strain elastoplasticity based on maximum plastic dissipation and the multiplicative decomposition: Part I. Continuum formulation. *Comput Methods in Appl Mech Eng , 66*(2), 199-219.

Simulia, Dassault Systemes. "Abaqus 6.14 documentation." Providence, Rhode Island, US (2012).

A.D. Spear, M.W. Czabaj, P. Newell, K. DeMille, B.R. Phung, D. Zhao, P. Creveling, N. Briggs, E. Brodbine, C. Creveling, E. Edelman, K. Matheson, C. Arndt, M. Buelte, S. Childs, I. Nelson, F. Safazadeh, J. French, C. Audd, A. Smith, E.J. Dorrian, G. Clark, J. Tayler, R. Ichi, The Third Sandia Fracture Challenge: From Theory to Practice in a Classroom Setting, *International Journal of Fracture*, submitted.

Spear, A. D., Priest, A. R., Veilleux, M. G., Ingraffea, A. R., & Hochhalter, J. D. (2011). Surrogate modeling of high-fidelity fracture simulations for real-time residual strength predictions. AIAA journal, 49(12), 2770-2782.

R. Storn and K. Price, *Differential Evolution - a Simple and Efficient Heuristic for Global Optimization over Continuous Spaces*, Journal of Global Optimization 11, pp. 341 - 359, 1997.

Z. Sun, X. Tan, S. B. Tor, and W. Y. Yeong, "Selective laser melting of stainless steel 316L with low porosity and high build rates," *Materials & Design*, vol. 104, pp. 197-204, 2016.

Sutton, M. A., Yan, J. H., Deng, X., Cheng, C. S., & Zavattieri, P. (2007). Three-dimensional digital image correlation to quantify deformation and crack-opening displacement in ductile aluminum under mixed-mode I/III loading. Optical Engineering, 46(5), 051003.

Tancogne-Dejean, T., Roth, C.C., Woy, U., Mohr, D., 2016. Probabilistic fracture of Ti–6Al–4V made through additive layer manufacturing. Int. J. Plast. 78, 145–172.

M. Tang, P. C. Pistorius, and J. L. Beuth, "Prediction of lack-of-fusion porosity for powder bed fusion," *Additive Manufacturing*, vol. 14, pp. 39-48, 2017.

Tupek, M., & Radovitzky, R. (2014). An extended constitutive correspondence formulation of peridynamics based on nonlinear bond-strain measures. *J Mech Phys Solids*, *1*(65), 82-92.

Tupek, M., Rimoli, J., & Radovitzky, R. (2013). An approach for incorporating classical continuum damage models in state-based peridynamics. Comput Methods in Appl Mech Eng, 263, 20-26.

Tvergaard, V. (1981). "Influence of voids on shear band instabilities under plane strain conditions." International Journal of Fracture **17**(4): 389-407.

Wang K and Wierzbicki T, “Experimental and numerical study on the plane-strain blanking process on an AHSS sheet”, Int J Fract, Vol. 194, pp. 19-36, 2015.

Wawrzynek, P. A., Carter, B. J., Hwang, C. Y., & Ingraffea, A. R. (2010). Advances in Simulation of Arbitrary 3D Crack Growth using FRANC3Dv5. Journal of the Computational Structural Engineering Institute of Korea, 23(6), 607-613.

M. Wilkins, R. Streit, and J. Reaugh, "Cumulative-strain-damage model of ductile fracture: simulation and prediction of engineering fracture tests," Lawrence Livermore National Lab., CA (USA); Science Applications, Inc., San Leandro, CA (USA) 1980.

A. S. Wu, D. W. Brown, M. Kumar, G. F. Gallegos, and W. E. King, "An experimental investigation into additive manufacturing-induced residual stresses in 316L stainless steel," *Metallurgical and Materials Transactions A*, vol. 45, pp. 6260-6270, 2014.

T. Zegard and G. H. Paulino, "Bridging topology optimization and additive manufacturing," *Structural and Multidisciplinary Optimization*, vol. 53, pp. 175-192, 2016.

Z. Xue, J. Faleskog and J. W. Hutchinson, "Tension-torsion fracture experiments - Part II: Simulations with the extended Gurson model and a ductile fracture criterion based on plastic strain," *International Journal of Solids and Structures*, vol. 50, pp. 4258-4269, 2013.

Zhou, J., X. Gao, J. C. Sobotka, B. A. Webler and B. V. Cockeram (2014). "On the extension of the Gurson-type porous plasticity models for prediction of ductile fracture under shear-dominated conditions." International Journal of Solids and Structures **51**(18): 3273-3291.